TOPOGRAPHIC AMPLIFICATION OF SEISMIC MOTION INCLUDING NONLINEAR RESPONSE

A Thesis
Presented to
The Academic Faculty

by

Seokho Jeong

In Partial Fulfillment
of the Requirements for the Degree
Doctor of Philosophy in the
School of Civil and Environmental Engineering

Georgia Institute of Technology
December 2013

TOPOGRAPHIC AMPLIFICATION OF SEISMIC MOTION INCLUDING NONLINEAR RESPONSE

Approved by:

Dr. Dominic Assimaki, Advisor
School of Civil and Environmental Engineering
Georgia Institute of Technology

Dr. David Frost
School of Civil and Environmental Engineering
Georgia Institute of Technology

Dr. Glenn Rix
School of Civil and Environmental Engineering
Georgia Institute of Technology

Dr. Zhigang Peng
School of Earth and Atmospheric Science
Georgia Institute of Technology

Dr. Adrian Rodriguez-Marek
Department of Civil and Environmental Engineering
Virginia Polytechnic Institute and State University

Date Approved: November 6, 2013

To my family

ACKNOWLEDGEMENTS

First and foremost, I would like to express my special thanks to my advisor, Dr. Dominic Assimaki, for introducing me to this subject and sharing her knowledge and experience with me throughout the period of this study. This work wouldnt have been completed without her endless and patient support and guidence.

I would like to extend my appreciation to other members of my thesis committee, Dr. David Frost, Dr. Glenn Rix, Dr. Zhigang Peng, and Dr. Adrian Rodriguez-Marek, for their guidances and insightful advices for this research.

The financial support for this work has been provided by the National Science Foundation under Grant No. CMMI-0936543 with title "NEESR-CR: Topographic Effects in Strong Ground Motion - From Physical and Numerical Modeling to Design". Such generous finacial support is gratefully acknowledged.

I would like to express my special thanks to my former and current officemates, Varun, Wei, Alex, Kami and Jian. I especially enjoyed the inspiring whiteboard discussions; I will surely miss it.

Last but not least, I would like thank my parents and my wife, Jina Park, for their unconditional love, continuous support and understanding. To them, I dedicate this work.

TABLE OF CONTENTS

LIST OF TABLES

LIST OF FIGURES

SUMMARY

Topography effects, the modification of seismic motion by topographic features, have been long recognized to play a key role in elevating seismic risk. Site response, the modification of ground motion by near surface soft soils, has been also shown to strongly affect the amplitude, frequency and duration of seismic motion. Both topography effects and 1-D site response have been extensively studied through field observations, small-scale and field experiments, analytical models and numerical simulations, but each one has been studied independently of the other: studies on topography effects are based on the assumption of a homogeneous elastic halfspace, while 1-D site response studies are almost exclusively formulated for flat earth surface conditions.

This thesis investigates the interaction between topographic and soil amplification, focusing on strong ground motions that frequently trigger nonlinear soil response. Recently, a series of centrifuge experiments tested the seismic response of single slopes of various inclination angles at the NEES@UCDavis facility, to investigate the effects of nonlinear soil response on topographic amplification. As part of this collaborative effort, we extended the search space of these experiments using finite element simulations. We first used simulations to determine whether the centrifuge experimental results were representative of free-field conditions. We specifically investigated whether wave reflections caused by the laminar box interfered with mode

conversion and wave scattering that govern topographic amplification; and whether this interference was significant enough to qualitatively alter the observed amplification compared to free-field conditions. We found that the laminar box boundaries caused spurious reflections that affected the response near the boundaries; however its effect to the crest-to-free field spectral ratio was found to be insignificant. Most importantly though, we found that the baseplate was instrumental in trapping and amplifying waves scattered and diffracted by the slope, and that in absence of those reflections, topographic amplification would have been negligible. We then used box- and baseplate-free numerical models to study the coupling between topography effects and soil amplification in free-field conditions.

Our results showed that the complex wavefield that characterizes the response of topographic features with non-homogeneous soil cannot be predicted by the superposition of topography effects and site response, as is the widespread assumption of engineering and seismological models. We also found that the coupling of soil and topographic amplification occurs both for weak and strong motions, and for pressure-dependent media (Nevada sand), nonlinear soil response further aggravates topographic amplification; we attributed this phenomenon to the reduction of apparent velocity that the low velocity layers suffer during strong ground motion, which intensifies the impedance contrast and accentuates the energy trapping and reverberations in the low strength surficial layers. We finally highlighted the catalytic effects that soil stratigraphy can have in topographic amplification through a case study from the 2010 Haiti Earthquake. Results presented in this thesis imply that topography effects vary significantly with soil stratigraphy, and the two phenomena should be accounted for as a coupled process in seismic code provisions and seismological ground motion predictive models.

CHAPTER 1

Introduction

Seismic hazard assessment and microzonation studies rely increasingly on wave motion simulations for the prediction of ground surface accelerations for given seismic input scenarios. By and large, however, ground motion simulations do not account for topographical features, making the sweeping assumption of a flat earth surface model.

Observations from large earthquakes on the other hand, have shown that the presence of a strong topographic relief can significantly aggravate the catastrophic consequences of strong seismic motion. A prominent example of so-called *topography effects* is the extraordinary ground motion (PGA=1.82g) recorded at the hilltop Tarzana strong motion station during the 1994 Northridge Earthquake [12]. And since tectonics and topography are closely related, most seismically active regions of the world are also marked by significant topographic relief, while the population growth in the recent years, combined with the scarcity of undeveloped metropolitan land, have changed land-use patterns and placed an increasing portion of the world's inhabitants and infrastructure assets in areas susceptible to topographic effects.

The understanding and simulation of topographic effects has important implications on ground motion predictions beyond seismic site response, both on a site-specific and on a regional hazard scale. Typical examples include the role of topographic effects on seismic slope stability assessment of natural formations and on the design and retrofit of critical man-made earth structures such as dams, bridge abutments, and embankments; as well as for the data processing and interpretation of ground motion recordings used to develop attenuation relationships. While, however, it is recognized that topographic amplification can elevate seismic risk, there is currently no consensus on how to reliably quantify its effects and the observed amplifications usually are much higher than what's predicted by analytical solutions and numerical simulations. This discrepancy has been attributed, among other reasons, to the lack of realistic soil conditions in predictive models on topographic amplification.

Although topography effects have been extensively studied through field observations, small-scale and field experiments, analytical models and numerical simulations, they have been considered independently of site response: studies on topography effects are based on the assumption of a homogeneous elastic halfspace, while site response studies are almost exclusively formulated for flat earth surface conditions. The interaction of topography effects and ground motion amplification caused by layered soils is scarcely documented and poorly understood; on the same time, the lack of this interaction from predictive models is considered at least in part responsible for the discrepancy between predictions and observations of topography effects [25].

This thesis investigates the possible interaction between topographic and soil amplification, focusing on strong ground motions that frequently trigger nonlinear soil response. Recently, a series of centrifuge experiments tested the seismic response of single slopes of various inclination angles at the NEES@UCDavis facility, to investigate the effects of nonlinear soil response on topographic amplification. As part of this collaborative effort funded by NEES, George E. Brown, Jr. Network for Earthquake

Engineering Simulations, we extended the search space of these experiments using finite element simulations. We first used validated numerical models to determine whether the centrifuge experimental results were representative of free-field conditions. We specifically investigated whether wave reflections caused by the laminar box interfered with mode conversion and wave scattering that govern topographic amplification; and whether this interference was significant enough to qualitatively alter the observed amplification compared to free-field conditions. We then used box- and baseplate-free numerical models to study the coupling between topography effects and soil amplification in free-field conditions. We finally complemented our findings by observations and simulations from a case study from the 2010 Haiti Earthquake.

Results in this thesis are organized in six Chapters. Chapter 2 briefly reviews the literature and current practice on topography effects, including recorded field evidence, theoretical and numerical predictions, and evidence from previous physical model studies on topography effects. In Chapter 3, we present results of numerical simulations validated by comparison with centrifuge experimental data [18]. We discuss in detail procedures of modeling centrifuge experiments, including how to characterize and calibrate material constitutive parameters. We then investigate the effects of wave reflections from the centrifuge boundary and the aluminum baseplate on the recorded topographic amplification, and extend results through numerical simulations to free-field (box and baseplate free) boundary conditions. Parametric simulations for free-field conditions are presented in Chapter 4; using the numerical model described in Chapter 3, we investigate the role of soil thickness, impedance contrast between surface and underlying soil layers, ground motion intensity, height of topographic feature, and impedance contrast between soil and bedrock on the topographic amplification of ground surface motion. Finally, Chapter 5 highlights some of our findings using a case from the 2010 Haiti earthquake, where unusually severe localized damage pattern was observed near Hotel Montana, at the top of a small foothill ridge. We

conducted numerical simulations and showed that the recorded amplification is most likely attributed to coupled site-topography amplification effects. We also showed the instrumental role of the bedrock depth in quantifying topographic amplification. Concluding remarks and future research directions are presented in Chapter 6.

CHAPTER 2

Literature Review

2.1 Field evidence of topographic effects

Topographic effects are associated with the presence of strong topographic relief (hills, ridges, canyons, cliffs, and slopes), complicated subsurface topography (sedimentary basins, alluvial valleys), and geological lateral discontinuities (e.g., ancient faults, debris zones). These features have been shown to significantly affect the intensity and frequency content of ground shaking during earthquakes. Observational evidence from past earthquakes indicates that damage concentrations occur where steep slopes or complicated topography is present; buildings located on the tops of hills, ridges, and canyons, suffer more intense damage than those located at the base during earthquakes. Examples of such observations were made in the 1971 San Fernando earthquake [10], the 1976 Friuli earthquake in Italy [14], and various others (see [3]).

There is also strong recorded evidence that surface topography affects the amplitude and frequency content of the ground motions. Reviews of such instrumental studies and their comparison to theoretical results can be found in [8, 23–25]. Among others, a case study on the response of a steep site in the Southern Alps revealed a crest-to-base spectral ratio of 20 [37]. In another case study, records obtained on a small ridge revealed that their spectral ratios to recorded motions at a nearby station located on flat ground were only a function of topography and site conditions and

were nearly independent of the azimuth, distance, and size of the seismic events [56]. Geli et al. [25] showed that topographic amplification ratios typically range from 2 to 10, while events have also been recorded with spectral amplifications on the order of 20 or more. The existing observational and instrumental evidence, however, has not been adequately documented to allow a statistically significant amount of data to be compiled into design guidelines on topographic effects.

Even further, recorded evidence of topography effects is almost exclusively from small or distant events; weak motion data, however, may not be applicable to describe topographic effects for strong motion shaking that is usually associated with nonlinear effects. Currently there are no fully documented case histories of topographic effects under strong ground motion, while there exist very few comprehensive parametric studies of the effects of soil nonlinearity on topographic amplification [5, 6].

2.2 Predictions of topographic effects

Prompted by observational and instrumented evidence, the problem of scattering and diffraction of seismic waves by topographical irregularities has been studied by many researchers. Nonetheless, while theoretical and numerical studies qualitatively predict the effects of topography on seismic ground motion, observed time- and frequency-domain amplification levels are much larger than theoretical predictions.

The inconsistency between theory and observations has been attributed in part to the fact that in the theoretical studies, topographic asperities are simulated as isolated ridges or depressions on the surface of idealized half-spaces.Furthermore, seismic input is usually represented by monochromatic or narrow-band pulses that cannot describe the broad-band nature of true earthquake motion. Examples of such numerical analyses include [7, 10, 11, 44, 51, 56] using various techniques including finite difference, finite-elements, boundary-element, and discrete-wave number methods. A limited number of examples, which involve more complex simulations such as

numerical models with soil layering and/or three dimensional effects, can be found in [2, 9, 13, 25, 45, 60]. A comprehensive review of such analyses is given in a study by Assimaki [3]. Experimental evidence and theoretical results are summarized by [8, 25] as follows:

1. There exists a qualitative agreement between theory and observations on ground motion amplification at ridges and mountain tops, and de-amplification at the base of hills.

2. The observed or computed amplification is first-order related to the "sharpness" of the topography: the steeper the average slope, the higher the peak amplification.

3. Topographic effects are frequency-dependent; the stronger effects correspond to wavelengths comparable to the horizontal dimension of the topographic feature.

2.3 Previous physical model studies

Previous research has demonstrated the feasibility of using a geotechnical centrifuge to study the dynamic response of earth systems (e.g. [21, 32]) and several recent studies have shown strong evidence of higher intensity shaking near the crests of model slopes. Ozkahriman et al. [38] examined the results of a centrifuge test on a sand embankment (performed as part of an investigation of other phenomena). Despite the modest inclination of the side slopes (25° and 30°), significant topographic amplification occurred at normalized frequencies (slope height/wavelength) of approximately 0.2 to 0.4. A similar centrifuge experiment was conducted by Madabhushi et al. [34] to investigate the seismic stability of steep slopes in granular soil. Acceleration-time histories recorded within the slope showed significant apparent acceleration amplification (from combined site and topographic effects) of the base motion.

2.4 Engineering Practice

Existing observational or instrumental data are neither adequate in quantity nor documented in sufficient detail to justify a rigorous statistical analysis needed to develop design recommendations to augment the existing code provisions on ground motion amplification via site-dependent factors. Also, published analytical and numerical studies -while qualitatively in agreement with field recorded evidence- have failed to quantitatively predict the amplification of seismic motion attributed to irregular topographic features in part due to simplified assumptions of the idealized models such as homogeneous, elastic halfspaces and narrowband pulses. As a result, topographic effects are not accounted for in current U.S. building codes and in routine seismic design. Recognizing the importance of topographic effects, new French and European provisions [1, 20] have introduced purely empirical, space-dependent but frequency-independent, topographic amplification coefficients that are used to multiply the elastic design spectra in the immediate vicinity of the crest to account for the topographic amplification of seismic motion, but these have not been validated by means of recorded evidence.

CHAPTER 3

Boundary wave reflections in centrifuge experiments on topography effects

3.1 Introduction

Topography effects, the modification of seismic ground motion in the vicinity of topographic features such as hills, ridges, cliffs, and canyons, is a well documented phenomenon [6–8, 10, 11]. Macroseismic observations from past earthquakes have systematically shown that steep slopes or complicated topography accentuate earthquake damage compared to flat ground, hence the term *topographic amplification of seismic motion*. The PGA=1.82g ground motion recording on the Tarzana hilltop during the 1994 Northridge Earthquake [12], the Pacoima Dam (PGA=1.12g) recording during the 1971 San Fernando earthquake [10], and the recent extraordinary ground motion (PGA=2.74g) recorded at the Japanese Seismic Network K-Net station MYG004 during the 2011 Tohoku Earthquake [36] are only a few examples of records that have been linked to topography effects.

Topography effects have been extensively researched in the recent decades. Field studies have revealed strong recorded evidence that surface topography significantly affects the amplitude and frequency content of surface ground motion [8, 23–25]; a prominent example of topographic amplification was reported by Nechtstein et

al. [37], who measured a crest-to-base spectral ratio of 20 at a steep site in the Southern Alps. However, these studies used almost exclusively ground motions from small or distant events. Several analytical and numerical studies have also been dedicated to the scattering, diffraction, focusing and mode conversion of seismic waves by ridges and hills; examples of the numerical techniques employed include closed form analytical solutions, discrete wavenumber methods, finite difference, finite elements and boundary elements [2, 3, 7, 9–11, 13, 25, 40, 44, 45, 51, 56, 60]. In addition to parametric and case-studies of isolated or idealized features, the effects of regional topography have been recently studied in the context of large-scale ground motion simulations; three-dimensional ground surface features extracted from high resolution digital elevation maps have started to replace the sweeping assumption of flat ground regional models [33, 35, 40]. However, with the exception of very few [3], these studies have focused on linear viscoelastic materials; because of this assumption, and other idealizations such as homogeneous halfspaces and monochromatic pulses, theoretical predictions almost ubiquitously underestimate observed topographic amplification by a factor of 10 or more in some cases Geli et al. [25]

Considering the limitations and assumptions of the above studies, it is unclear whether their results adequately describe topography effects for strong ground motion; recorded topographic amplification factors from well-documented case studies are available only for weak events, and results from numerical predictions are by and large conditioned on linear viscoelastic soil behavior. Among others, Dafni [18] approached this question by conducting a series of centrifuge experiments, in which idealized features were subjected to ground motion suites that ranged from weak to strong –adequate to cause nonlinear effects, but not strong enough to cause slope stability failure– and from monochromatic to broadband. Published results from previous centrifuge experiments on the seismic response of earth systems (embankments, slope stability analyses) [21, 32, 34, 38] have reported that the ground motions near the

features's crests were amplified compared to recordings on the flat surfaces of the models, thus alluding to the potential use of centrifuge experiments in studies of topography effects.

In this study, we investigated the extent to which the amplification observed in centrifuge experiments by Dafni [18] and others, is representative of free-field topography effects. We hypothesized that centrifuge box boundary effects (reflections) may interfere with mode conversion and wave scattering effects that govern topographic amplification, and aimed to understand whether this interference is significant enough to qualitatively alter the observed topographic amplification compared to field conditions. We studied this problem using finite element simulations, which we first validated using centrifuge observations, and then extended to free-field boundary conditions by removing the constraints of the laminar box and aluminum base plate. We then compared the amplification patterns in space and frequency, as well as the absolute amplitude, to our predictions of the same configuration in free-field conditions. The aim of this study was twofold: (i) to highlight the advantages and limitations of centrifuge experiments in simulating topography effects, and in doing so, to guide the design and interpretation of future experimental studies on 3D site effects, which aim to complement our scarce and sparse observations of strong motion site response; (ii) to provide a detailed description of a cyber-model of free-field nonlinear topography effects that we, and other researchers, can use to expand the search space of centrifuge experiments for this class of problems, at a fraction of the experimental cost.

3.2 Validation: Numerical simulation of centrifuge experiments

Dafni [18] conducted centrifuge experiments at 27g and 55g acceleration at the NEES site of the University of California, Davis (`http://nees.ucdavis.edu/`). The models

were prepared with dry Nevada sand in the flexible shear beam container of the facility, FSB-2, which comprises an aluminum base plate, five metal rings. The rings are separated by 12 mm thick soft neoprene rubber layers, which provide lateral flexibility. The container also has several flexible vertical rods, which are designed for the complementary shear stress at the interface of soil and container [31]. Figure 3.1 shows the actual photos of physical models for the flat and 30° slope configurations; photo of 30° slope configuration also shows the exposed flexible vertical rods for complementary shear stress. Technical specifications of the centrifuge, shaking table (base plate) and containers at NEES@UCDavis can be found in Kutter et al. [31].

3.2.1 Geometry, boundary conditions and material calibration

We simulated the centrifuge experiments using the finite element (FE) code DYNAFLOW ™ [42]. Of the three single slope configurations tested by Dafni [18] ($20°, 25°$ and 30°) we here present numerical predictions for the 30° single slope. Since topographic amplification is proportional to the feature steepness, and slope instability of granular media increases as the natural slope approaches the material friction angle, the 30° slope was selected as the 'worst case' scenario configuration among all single slopes tested. We also simulated the flat ground model of Dafni [18] that we used as far-field reference, that is to say as a site that, while located adequately far from the topographic feature, has identical soil profile and incident ground motion, and exhibits one-dimensional response to ground shaking (Figure 3.2). The corresponding finite element meshes of the two models are shown in Figure 3.3.

We used plane strain elements (2D) to simulate the centrifuge box and the soil, and calibrated the mass and stiffness of the 2D numerical model of the container to match the corresponding properties of the three-dimensional (real) container. The linear elastic properties that were selected for the metal rings are described in detail in Kutter et al. [31]. The neoprene foam rubber, on the other hand, was modeled as

Figure 3.1: Photos of physical models: a flat ground configuration (top) and a single slope with angle of 30° (bottom)

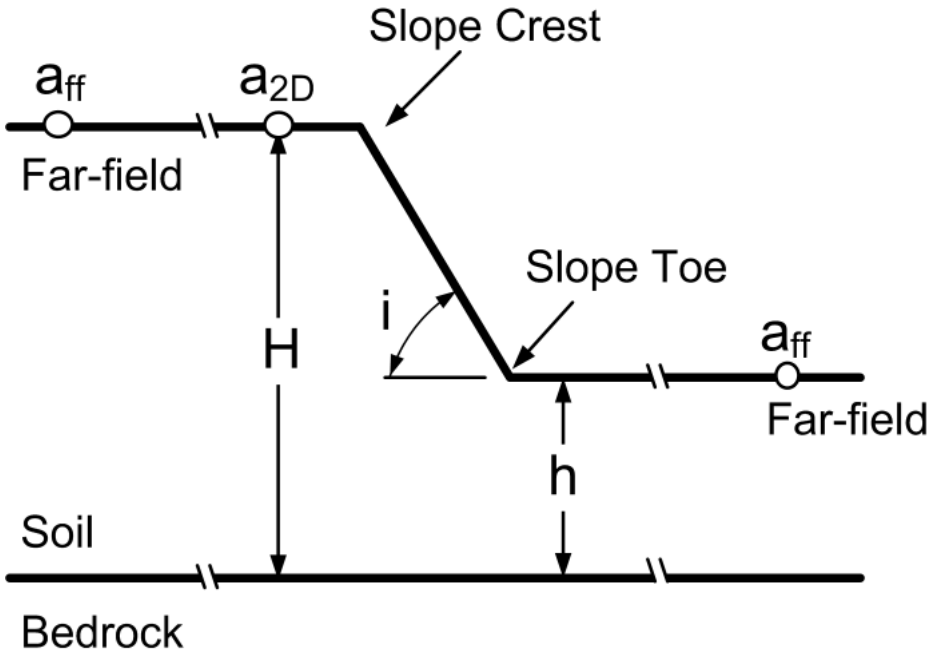

Figure 3.2: Nomenclature for studies on topography effects: near-crest acceleration, a_{2D}, is affected by both 1-D site response and topography effect; and far-field acceleration, a_{ff}, is affected only by 1-D site response.

viscoelastic material; based on Snowdon [52], the shear modulus (G) and damping (ζ) of neoprene rubber at the ambient temperature of the experimental facility are $G = 0.25MPa$ and $\zeta = 6\%$ correspondingly, while the latter is almost frequency independent for loading frequencies up to 100Hz. Figure 3.4 compares the experimental data by Snowdon [52] with the calibrated Rayleigh damping used in our simulations. The flexible vertical rods (shown in figure 3.1), which provide complementary frictional resistance between the soil and the container sides, were neglected; instead, we assumed perfect (non-slip) soil-container contact. However, the loss of contact between soil and container sides during shaking was simulated by assigning zero extensional strength to the soil. We also rigidly linked the horizontal degrees of freedom of the ring elements, so that the left and right container sides deform horizontally in sink; the implicit assumption here is that the axial deformation of the rings during shaking is negligible. The equivalent material properties of the rings and rubber are listed in Table 3.1.

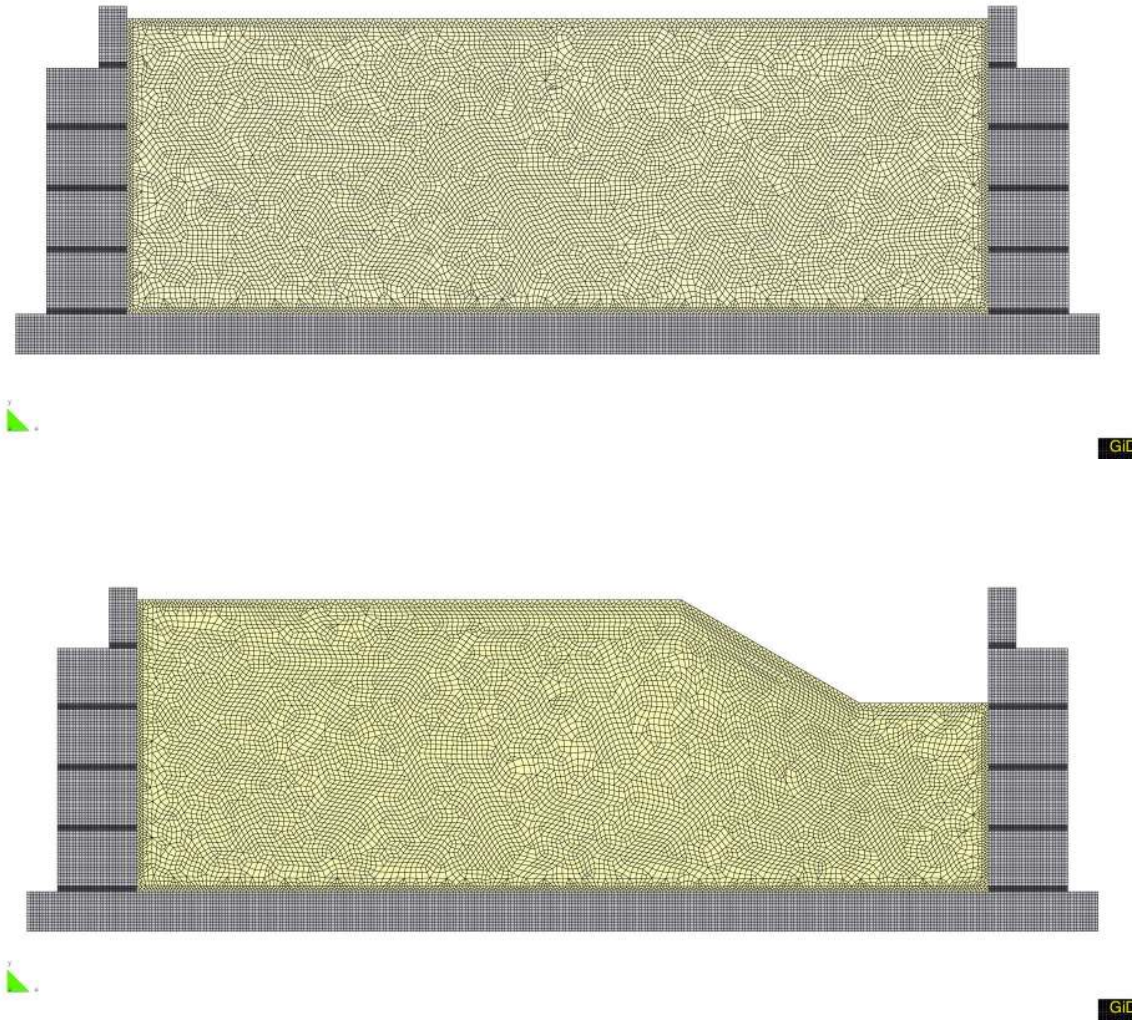

Figure 3.3: 2-dimensional finite element mesh of a centrifuge experiment model: a flat ground configuration (top) and a single slope with angle of 30° (bottom)

Table 3.1: Material parameters selected for numerical model of the flexible container FSB-2

	E [MPa]	ν	ρ $[Mg/m^3]$	α	β
Ring 1	70000	0.35	1.92	0	0
Ring 2	70000	0.35	2.19	0	0
Ring 3	70000	0.35	2.19	0	0
Ring 4	70000	0.35	4.14	0	0
Ring 5	70000	0.35	5.24	0	0
Rubber 1	2	0.499	2.0	9	0.0001
Rubber 2 $\sim$ 5	1.5	0.499	2.0	9	0.0001

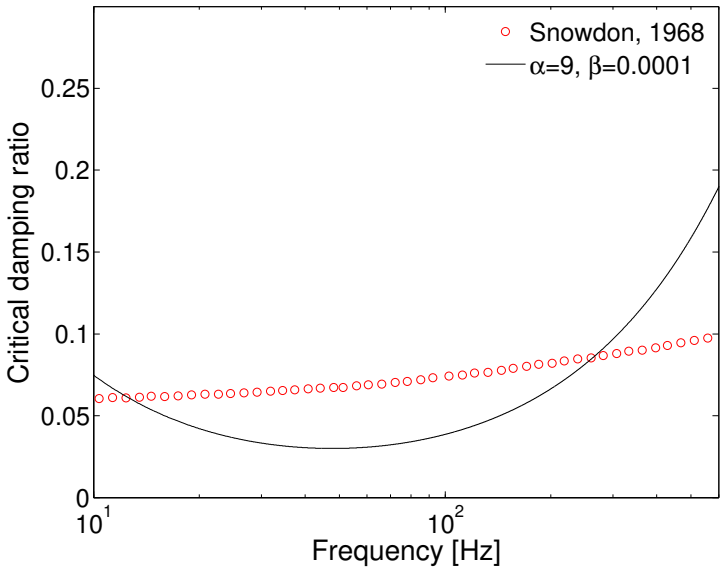

Figure 3.4: Critical damping ratio of neoprene foam rubber and Rayleigh damping approximation used in the simulations; the neoprene foam rubber has a shear modulus of $G = 0.25MPa$ and a damping ratio of $\zeta = 6\%$ that is almost frequency independent up to 100 MHz in room temperature.

We simulated the dry Nevada sand using the pressure dependent multi-yield (PDMY) plasticity model by Prevost [41, 42], and employed a purely kinematic hardening rule with round-cornered Mohr-Coulomb yield surfaces, an associated flow rule for the deviatoric strains, and a non-associated flow rule for the volumetric plastic strains. The sand's pressure-dependent shear modulus was idealized by the power law of Equation (1), where G_{max} is the elastic shear modulus at the reference hydrostatic pressure p_{ref}.

$$G = G_{max} \left(\frac{p}{p_{ref}} \right)^n \tag{1}$$

Figure 3.5 shows the shear wave velocity (V_s) profile of dry Nevada sand with relative density $D_r = 100\%$ measured by Stevens et al. [54] in a previous centrifuge experimental study that used the same container; in absence of similar data from Dafni [18], we used the Stevens et al. [54] measurements for the initial calibration of Equation (1), which we iteratively re-calibrated using ground motion data recorded

by Dafni [18] during the flat ground model shaking tests.

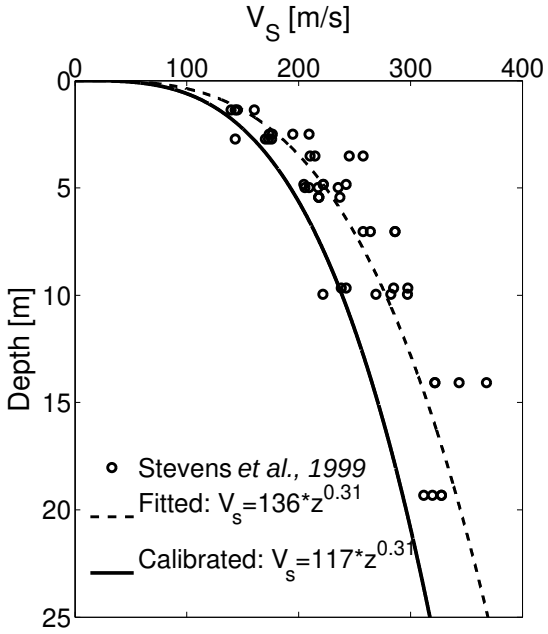

Figure 3.5: Shear wave velocity profile of dry Nevada sand with relative density of 100% as published by Stevens et al. [54]. The black dashed line shows fitted power law used in the design phase of the centrifuge experiments; the black solid line shows the final velocity profile after calibration using the result from flat ground model.

Finally, we simulated the monotonic shear stress-strain response of the soil using the generalized hyperbolic model by Hayashi et al. [28] shown in Equations (2) and (3):

$$f(x,n) = \frac{\left(\frac{2}{n}x+1\right)^n - 1}{\left(\frac{2}{n}x+1\right)^n + 1}; n > 0 \tag{2}$$

$$y = e^{-\alpha x} \cdot f(x, n_L) + (1 - e^{-\alpha x}) \cdot f(x, n_U) \tag{3}$$

where x is the shear strain (γ) normalized with respect to the reference strain $\gamma_r = \tau_f / G_{max}$, τ_f and G_{max} are the soil shear strength and maximum shear modulus respectively, y is the shear stress τ normalized with respect to the shear strength, $y = \tau/\tau_f$, and α, n_L and n_U are three model parameters.

Hayashi's model combines two standard hyperbolic models [30] as shown in Equation (3), but reduces to the standard hyperbolic form when $n_L = n_U = 1$. Such a versatile formulation was necessary to allow simultaneous matching of the soil's shear modulus (G_{max}) (at low strains), and ultimate shear strength (τ_f) (at high strains).

Parenthetically, the minimum strain amplitude at which dynamic soil properties are measured has decreased by two orders of magnitude in the last 30 years: from $\gamma = 0.25 \times 10^{-4}$ in the 1970's to $\gamma = 10^{-6}$ or less today. Consequently, when models developed in the 70s, such as the hyperbolic model [27] among others, are used to fit recently measured data, they either underestimate G_{max} or overestimate τ_f. Recent studies [19, 50, 57] have in fact shown that the shear modulus measured at $\gamma = 10^{-6}$ can be as high as twice the corresponding value measured at $\gamma = 10^{-4}$ depending on the soil composition and hydrostatic pressure. Formulations such as the Hayashi et al. [28] and the recently proposed [59], have improved monotonic shear model fitting: parameter α controls the transition of y from $f(x, n_L)$ to $f(x, n_U)$ with increasing x, while n_L and n_U control the rate of modulus reduction in small and large strains respectively. The model thus allows not only independent matching of the small and large strain modulus reduction and damping curves, but also a good fit in the intermediate (transition) strain range.

For the model calibration, we initially fitted G_{max} and τ_f; we used the V_s data by Stevens et al. [54] to compute G_{max}, and assumed a friction angle of $\phi = 42°$ for the dry Nevada sand with $D_r = 100\%$ to estimate τ_f. Successively, we computed the monotonic loading curve and it's derivative (G/G_{max}), selected a modulus reduction curve from Darendeli [19] that closely matched the latter, and fitted the intermediate strain range (i.e. α). Figure 3.6 shows the fitted curve and the corresponding backbone curve at the reference pressure $p_{ref} = 100kPa$. We assigned higher weight to G_{max} and ϕ, and lower weight to the intermediate strain range values in our calibration, which explains why our model deviates from the Darendeli [19] curve at the

same reference pressure. The soil parameters at the end of the calibration phase that were used in the simulations described below are summarized in Table 3.2.

Table 3.2: Material parameters calibrated for dry Nevada sand at relative density $D_R = 100\%$

$\rho\ [Mg/m^3]$	ν	$G_0\ [MPa]$	$p_{ref}\ [kPa]$	n	$\phi\ [^\circ]$	$\Psi\ [^\circ]$	X_{pp}	α	n_L	n_U
1.7	0.25	108	100	0.62	42	35	0.05	0.4	0.5	1.0

3.2.2 Ground motions

The ground motions selected from Dafni [18] for our numerical simulations are listed in Table 3.3; they comprise three recorded (broadband) ground motions (BPTS315, JOS090 and TCU078E), each scaled at two different amplitudes, a frequency sweep (FREQ55NEW) and a sequence of Ricker wavelets (RICK55). The time histories and corresponding Fourier amplitude spectra, as recorded at the baseplate of the container are plotted in Figure 3.7; the acceleration response spectra of all motions are plotted in Figure 3.8, where the gray lines represent the spectral acceleration of each ground motion, and the black line depicts their median spectral acceleration.

Table 3.3: Ground motions selected for numerical simulations

Label	Description	Prototype amplitude (g)	Amplitude scale
BPTS315	Superstition Hills Parachute T S 315	0.25	0.5 and 1
JOS090	Landers-Joshua Tree 090	0.25	0.3 and 1
TCU078E	Chi Chi TCU078-E	0.1	0.7 and 1
FREQ55NEW	Frequency Sweep 1–6–1Hz	0.1	1
RICK55	Ricker wavelets 0.5–1–2–3–4–6Hz	0.1	1

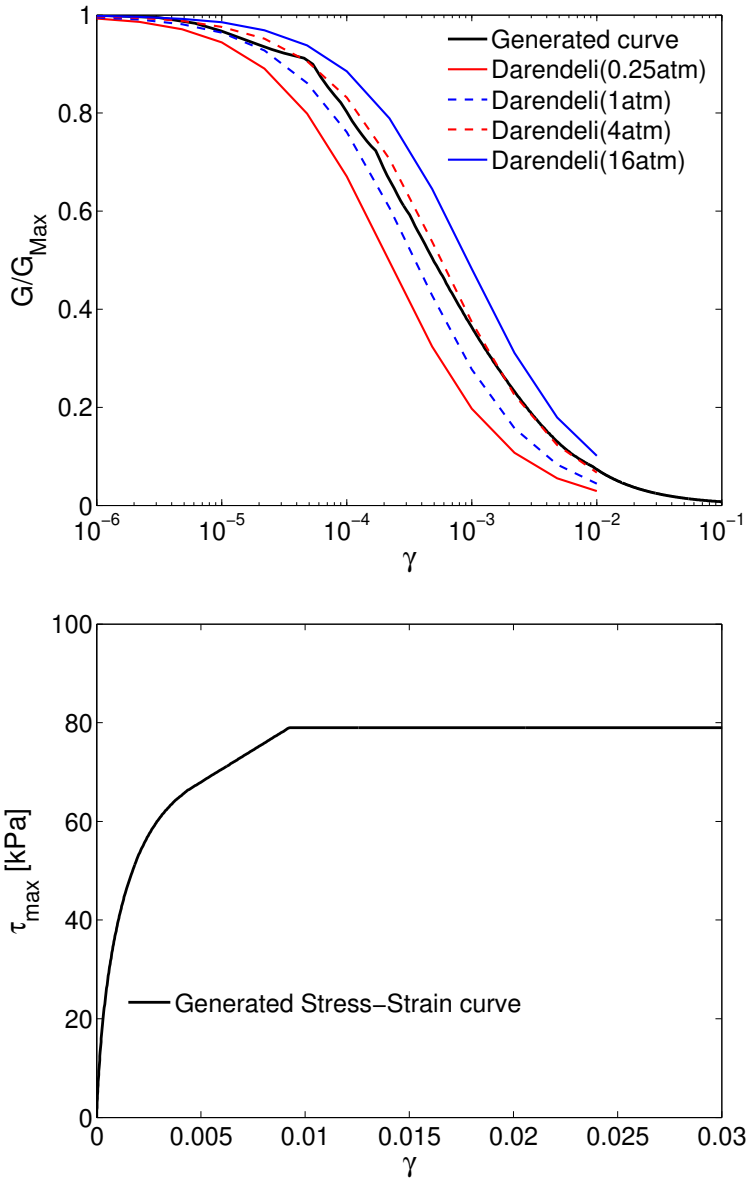

Figure 3.6: Calibrated modulus reduction curve at $p_{ref} = 100kPa$ compared to the data by Darendeli [19] (top), and the corresponding stress-strain curve (bottom) with friction angle of 42°.

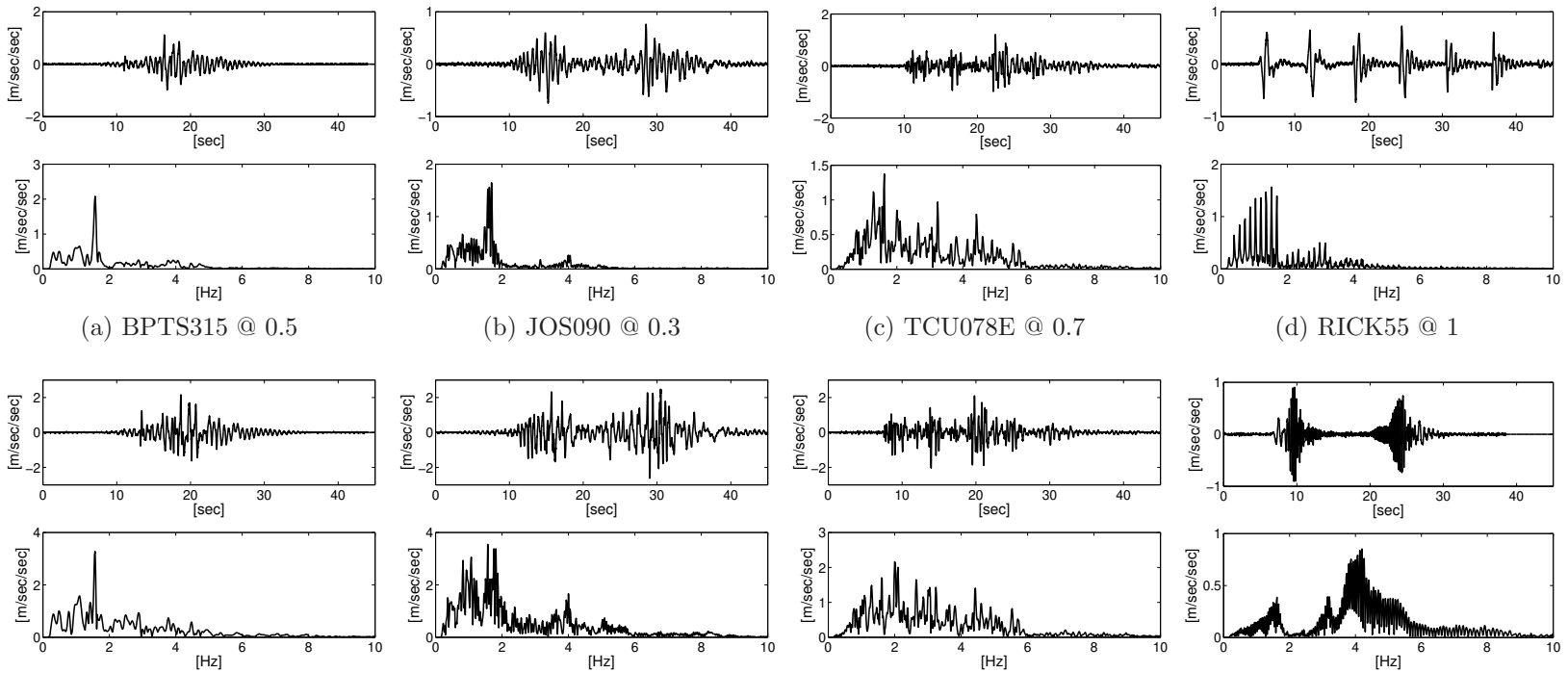

(a) BPTS315 @ 0.5 (b) JOS090 @ 0.3 (c) TCU078E @ 0.7 (d) RICK55 @ 1

(e) BPTS315 @ 1 (f) JOS090 @ 1 (g) TCU078E @ 1 (h) FREQ55NEW @ 1

Figure 3.7: Baseplate acceleration time histories and fourier amplitude spectra, used for numerical simulations.

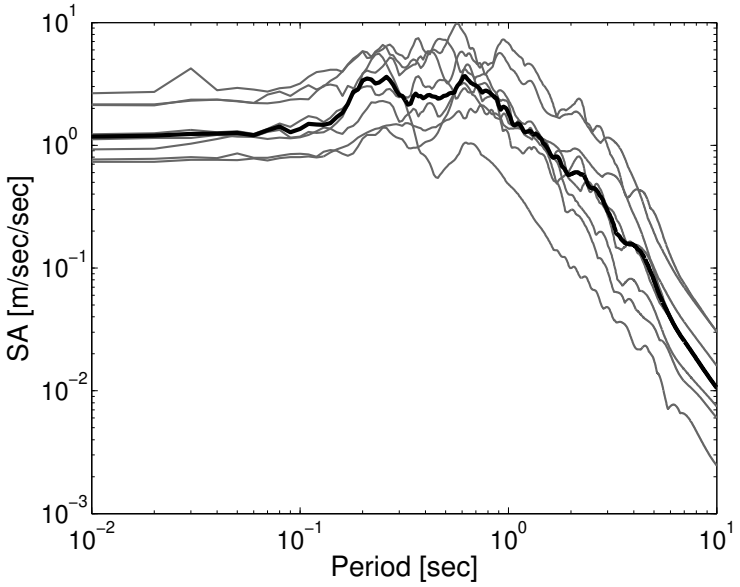

Figure 3.8: Acceleration response spectra computed from baseplate acceleration time histories; median spectral acceleration is plotted with black solid line.

3.2.3 Validation of simulated ground motions

Results from the simulated experiments were next compared to recorded motions, which are here presented in prototype units unless otherwise stated. We first compared recordings from the surface sensors A-28 and A-30 located in the off-plane direction along the centerline (see Figures 3.9 and 3.10); it was important to examine whether the ground surface response was contaminated by boundary effects normal to the direction of shaking, because such a finding could invalidate our assumption of plane strain conditions.

Fortunately, almost no variability was observed as shown in Figure 3.11, which compares recorded to simulated acceleration time histories for four representative input ground motions: 1) weak and narrowband, 2) weak and broadband, 3) strong and narrowband and 4) strong and broadband. The corresponding Fourier amplitude spectra are shown in Figure 3.12. Similarly, Figures 3.13 and 3.14 compare the acceleration time histories and Fourier amplitude spectra respectively, as recorded by the same sensors for the 30° single slope.

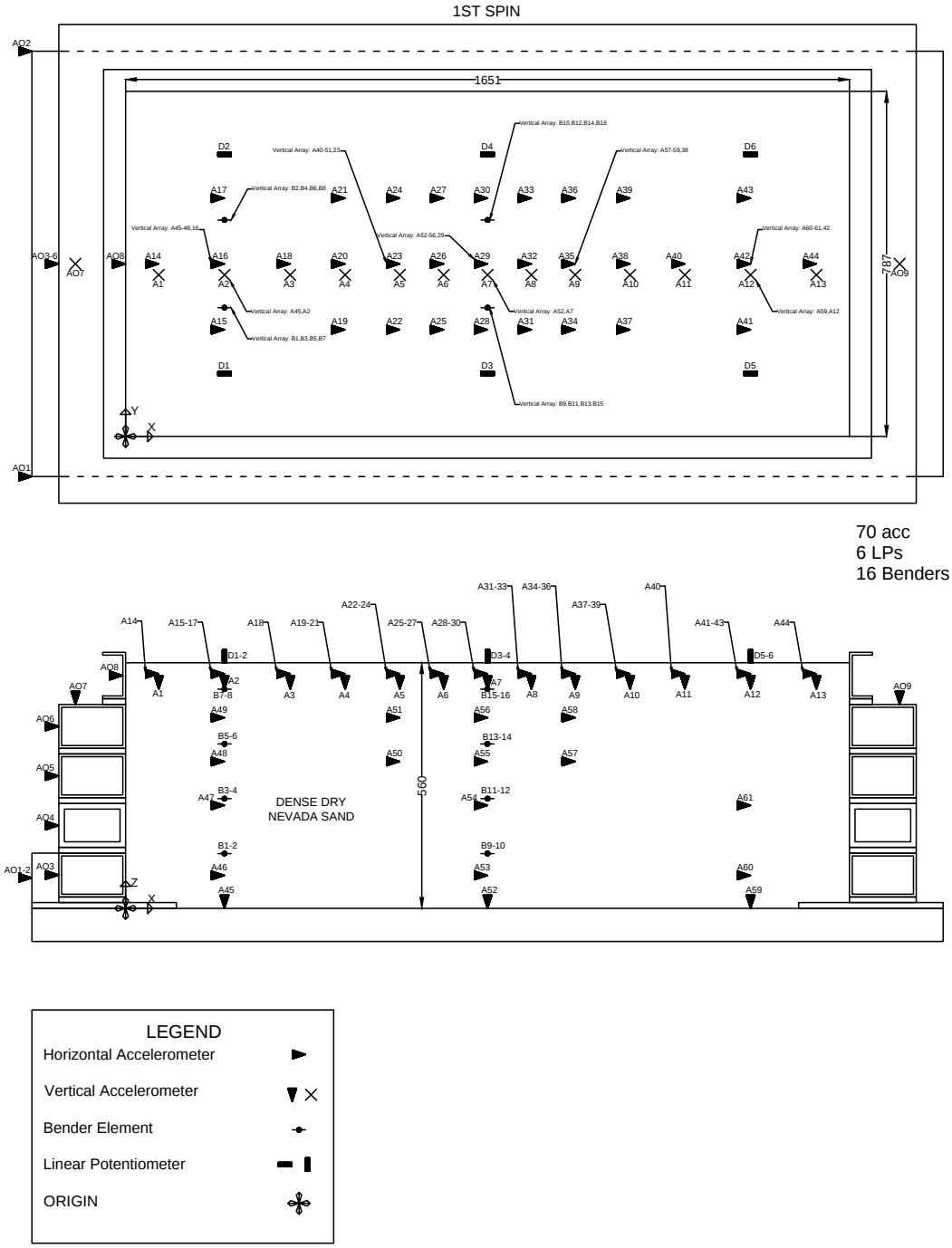

Figure 3.9: Sensor deployment plan for centrifuge experiments: Flat surface

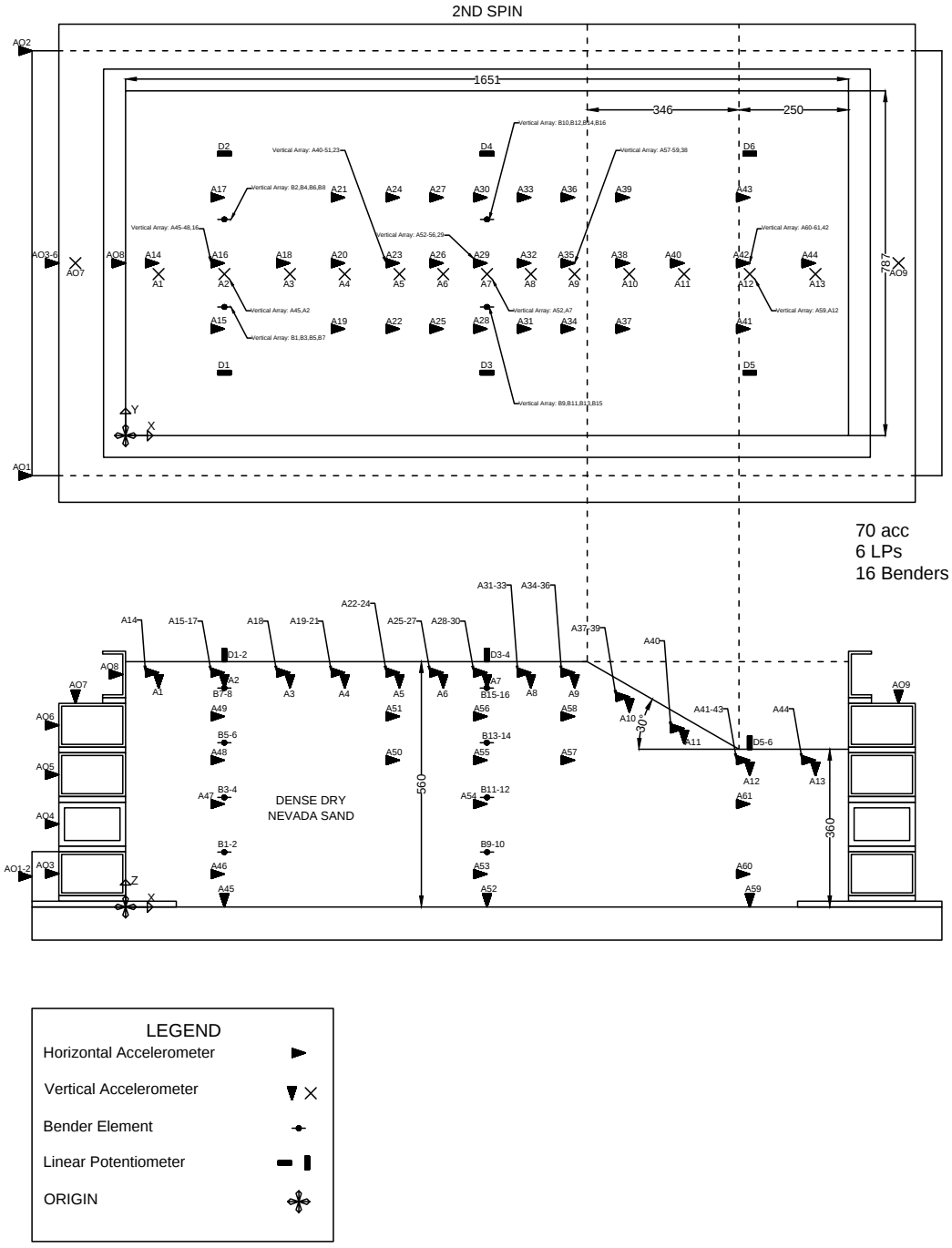

Figure 3.10: Sensor deployment plan for centrifuge experiments: 30° slope

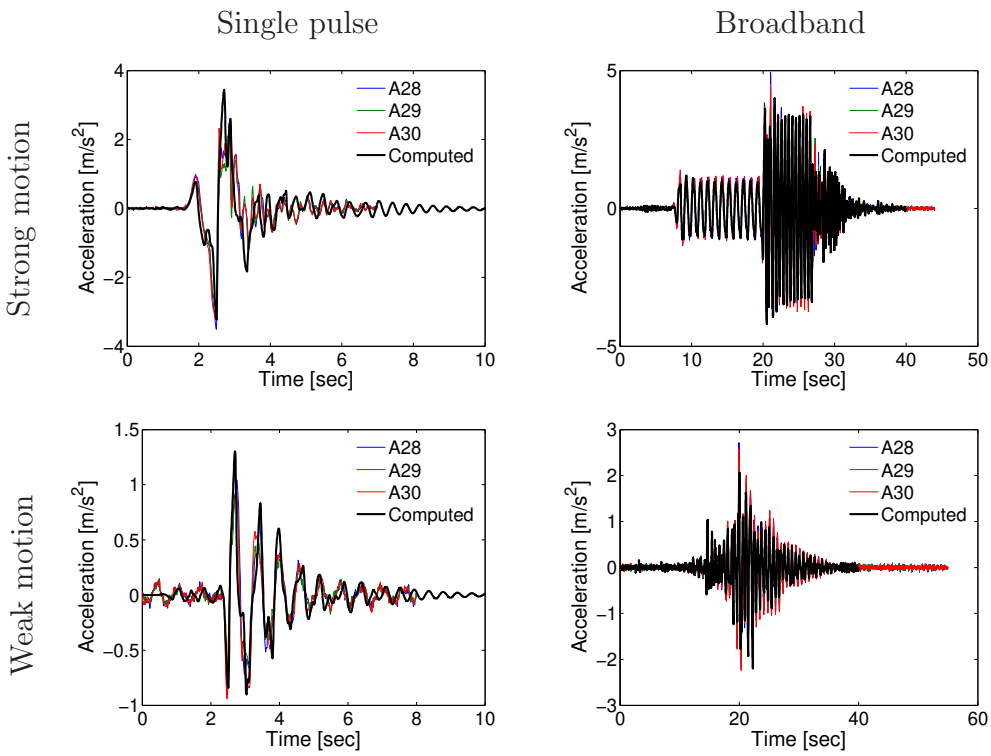

Figure 3.11: Validation of numerical model: Computed acceleration time histories from the flat surface model at the center of the surface compared with the centrifuge experiment results measured from sensors A28, A29 and A30.

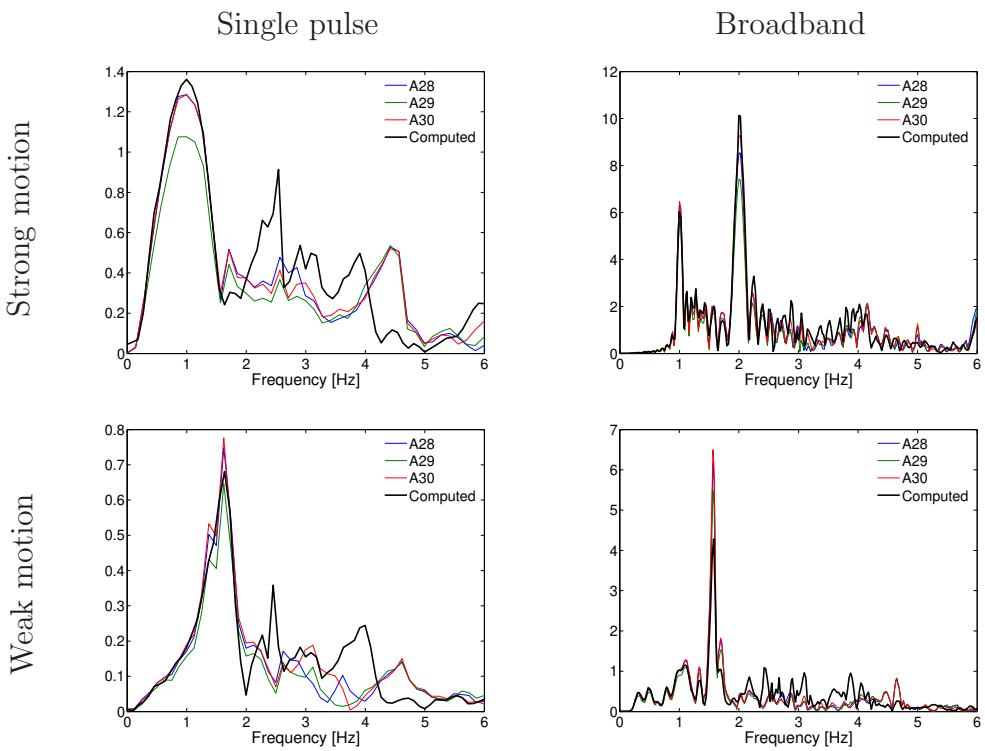

Figure 3.12: Validation of numerical model: Fourier spectra of computed acceleration time histories from the flat surface model at the center of the surface compared with the centrifuge experiment results measured from sensors A28, A29 and A30.

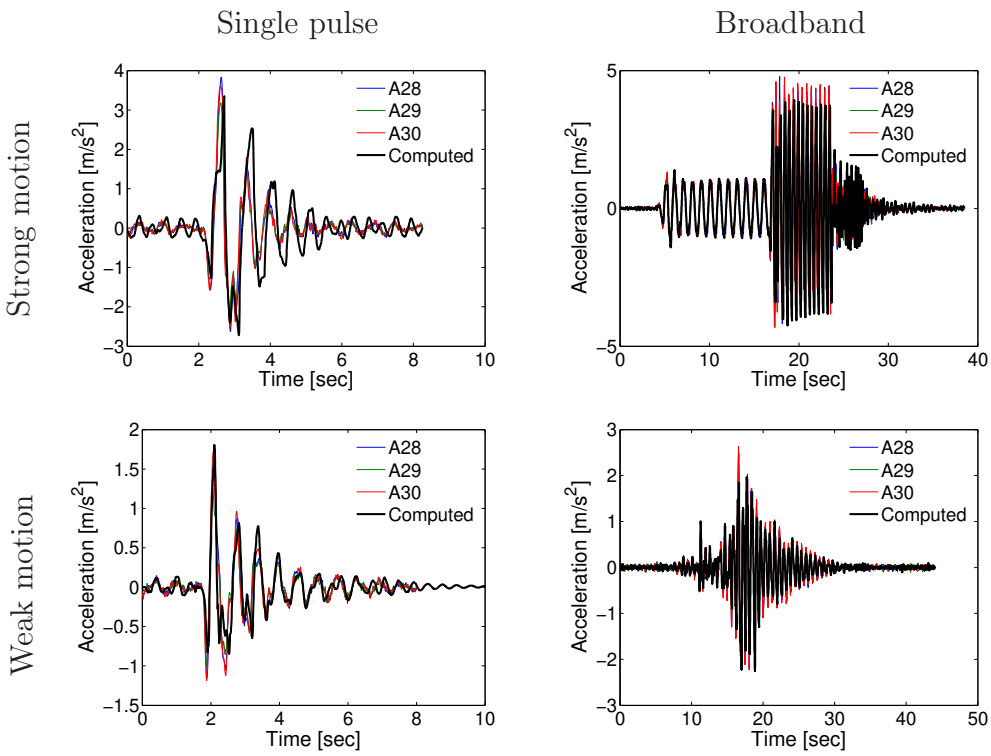

Figure 3.13: Validation of numerical model: Computed acceleration time histories from the 30° single slope model at the center of the surface compared with the centrifuge experiment results measured from sensors A28, A29 and A30.

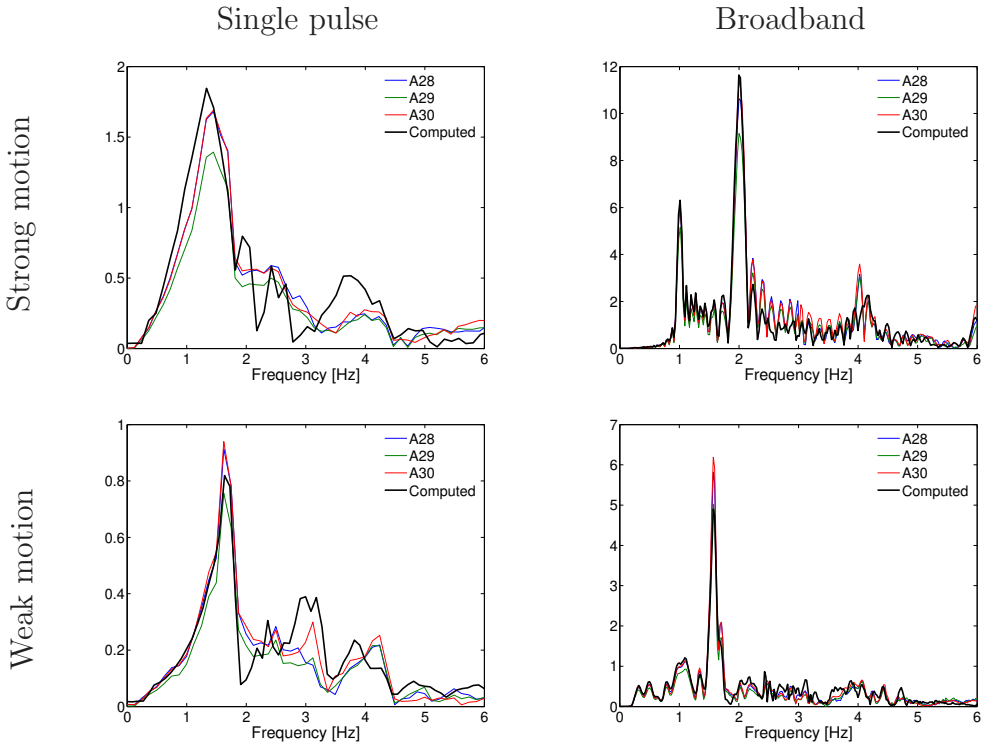

Figure 3.14: Validation of numerical model: Fourier spectra of computed acceleration time histories from the 30° single slope model at the center of the surface compared with the centrifuge experiment results measured from sensors A28, A29 and A30.

We then compared simulated to recorded motions along the vertical array of sensors at the centerline of the container (see sensors A29, A56, A55, A54 and A53 in Figure 3.14 from top to bottom). Results for the 30° slope are shown in Figure 3.15. Overall, we observed excellent agreement between simulated and recorded ground motions.

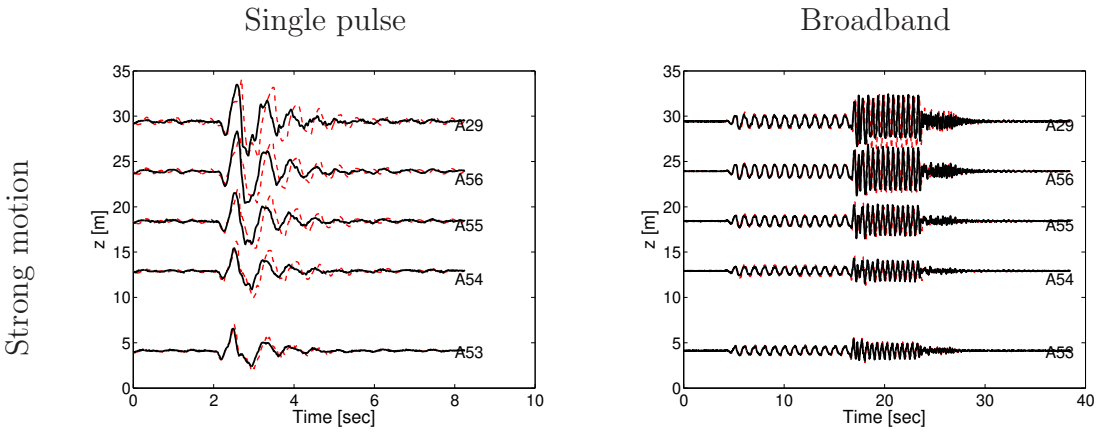

Figure 3.15: Validation of numerical model: Arrays of horizontal acceleration time histories computed along the depth of the numerical model (solid line) from the 30° single slope model compared to the corresponding experiment results measured at sensors A29, A56, A55, A54 and A53 (dashed line).

3.2.4 Topographic amplification factors: Empirical vs. Computed

Traditionally, topography effects have been measured and reported as the modification (frequently amplification) of ground motion in excess of 1D site response [3]. To test whether centrifuge experimental results were representative of free-field topographic amplification, we chose to compare them to numerical simulations in a form that puts them into context with previously published solutions. Thus, we compared the empirical to computed *topographic amplification factor*, defined as the Fourier amplitude ratio of ground motion at (or near) the crest to the motion in the far-field (see Equation (4)). Note that we used the flat ground model response as far-field, because we assumed that the flat sections of the sloped model (see stations A16,

A18 or A20 for example in Figure 3.14) were contaminated by spurious boundary reflections.

$$SR(\omega) = \frac{A^h_{2D}(\omega)}{A^h_{ff}(\omega)} \tag{4}$$

where $A(\omega)$ is the Fourier amplitude of acceleration time history $a(t)$, $\omega = 2\pi f$ is the circular frequency, and the superscript h refers to the horizontal component of ground motion.

As mentioned above, the premise of Equation (4) is that the stations recording $a_{2D}(t)$ and $a_{ff}(t)$ have the same soil profile and the same input motion. This condition was not satisfied in the centrifuge experiments; while the command displacements of the flat ground and sloped tests were the same, the recorded baseplate motions were not, a direct consequence of the differences in mass (and thus inertia feedback) of the two configurations. Using the theory of reciprocity, we corrected the experimental topographic amplification factor for the baseplate motion difference as shown in Equation (5); because the premise of Equation (5) is that the response of both the flat ground and sloped models is linear elastic (at least approximately), the applicability of Equation (5) is thus limited to weak ground motions.

$$\hat{SR}(\omega) = \frac{A^h_{2D}(\omega)}{A^h_{ff}(\omega)} \times \frac{A^h_{BP,flat}(\omega)}{A^h_{BP,sloped}(\omega)} = \frac{A^h_{2D}(\omega)}{\hat{A}^h_{ff}(\omega)} \tag{5}$$

where $\hat{A}^h_{ff}(\omega)$ is the corrected far-field reference ground motion, computed by convolving the recorded baseplate motion of the sloped model with the experimental 1D transfer function (surface over baseplate) of the flat ground model; BP stands for baseplate, $flat$ for the flat ground model, and *sloped* for the sloped model. The raw empirical amplification factors are compared to the corrected ones in Figure 3.16.

In the simulated experiments on the other hand, we used the exact same base plate motion for sloped and flat ground, so this correction was not necessary. Figure 3.17 compares the corrected experimental to the computed median topographic

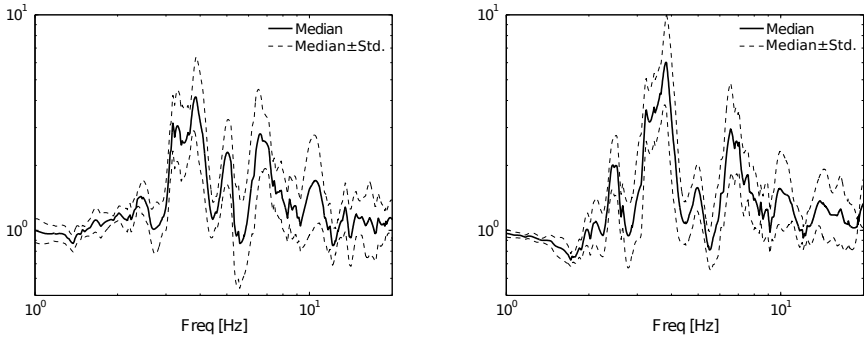

Figure 3.16: Crest–to–Freefield spectral ratios: uncorrected (left) and corrected for the input motion difference (right)

amplification factor at the crest (station A35). Topographic amplification manifested at approximately the same frequencies in both cases, $3.5Hz$ and $6.5Hz$, although the agreement was less favorable for the corresponding absolute peak amplitudes. The source of the mismatch could be the assumption of linear response in the experimental data (although we limited our comparisons to weak motions, soils exhibit nonlinear response even at very low strains), the contribution of three-dimensional effects not accounted for in our numerical simulations, or both.

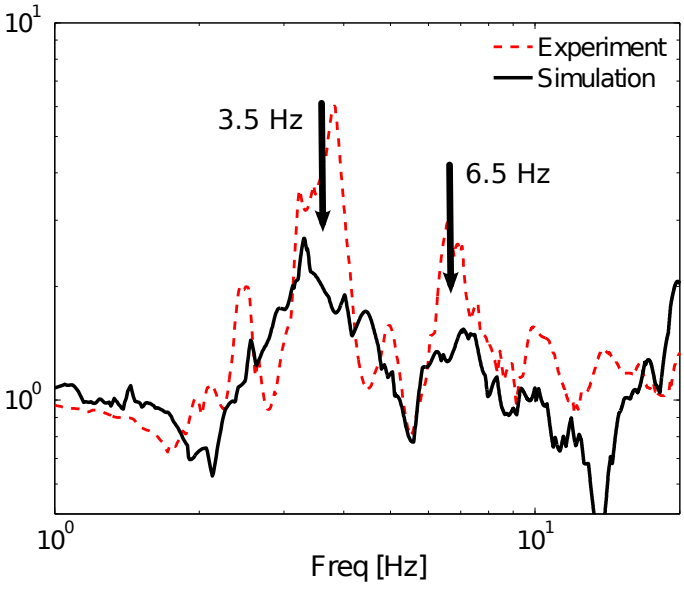

Figure 3.17: Validation of numerical model: Comparison of crest to freefield spectral ratio

3.2.5 Topographic amplification via in-flight ambient vibrations

Retrospectively, we investigated whether weak nonlinear soil response contributed to the divergence between corrected empirical and computed topographic amplification factors. For this purpose, we used the in-flight ambient vibrations recorded by Dafni [18] during spinning and prior to shaking, which –because of their very low amplitude– we hypothesized were associated with model response as closely to elastic as possible. High quality pre-shaking ambient vibration recordings were only available for the 30° slope. For the flat ground reference model, we used instead pre- and post-shaking vibrations, with the caveat that the latter were likely contaminated with model free vibrations at the end of shaking, and the former were not of duration long enough to allow a low variance time-series dataset to be extracted.

In all cases, we only used the in-plane horizontal component. All signals were windowed and tapered using a tapered cosine (Tuckey) window with tapering parameter $\alpha = 0.4$, and duration of 8 seconds. Figure 3.18 shows the tapered and stacked windows of recorded vibrations for the 30° slope and flat ground models respectively, and their corresponding Fourier amplitude spectra. The figure also shows the time-series and Fourier amplitude spectra of ambient vibrations at the baseplate of the two models. Both surface and baseplate signals were found to be of high quality and of broadband nature, indicators that the ambient, pre- and post-shaking vibrations could potentially yield reliable amplification factors. The resulting raw (Equation 4) and corrected (Equation 5) ambient vibration amplification factors are compared in Figure 3.19, and the corrected amplification factors are compared with linear elastic simulation in figure 3.20. We found satisfactory agreement between the measured (and corrected) and simulated spectral ratios at frequencies higher than $4Hz$. The misfit in lower frequencies can be attributed to the lack of high quality ambient vibration measurement for flat ground model. The difference between raw and corrected spectral ratios appears far more pronounced for ambient vibrations than for

the recorded ground motions, because measured ambient vibrations are very sensitive to changes in ambient parameters such as temperature and centrifuge spin rate.

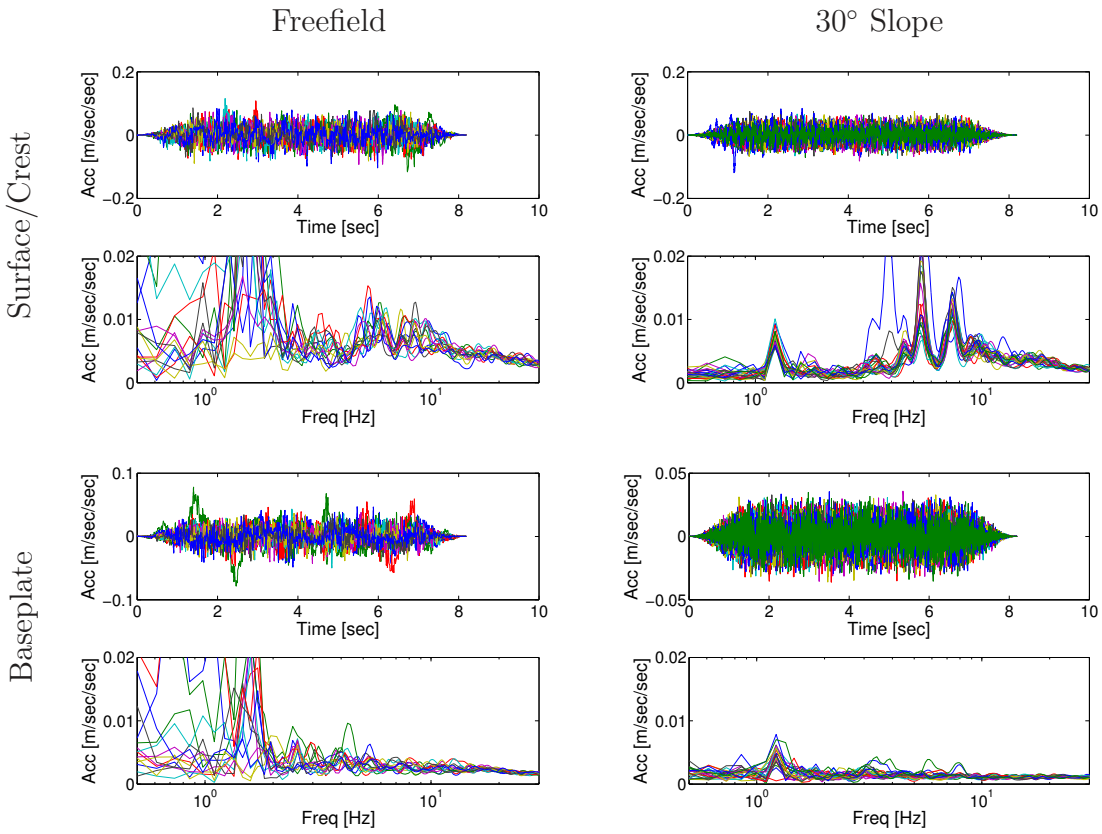

Figure 3.18: Measured ambient accelerations and pre- and post-shaking acceleration signals; windowed and tapered using a tapered cosine (Tuckey) window with tapering parameter $\alpha = 0.4$ and duration of 8 seconds.

Figure 3.21 shows the corrected median amplification factors obtained from ambient vibrations compared with the corresponding factors obtained during shaking (shown in Figure 3.17). Spectral ratios obtained from the ambient vibrations were qualitatively similar to the empirical topographic amplification factors obtained from the shaker ground motion input, with the two distinct peaks shifted to the left, an indication that the sloped model exhibited inelastic response during the experiments, even at very low strains. Our results indicate that ambient vibrations during the free spinning phase of centrifuge experiments may be used as estimates of elastic topographic amplification.

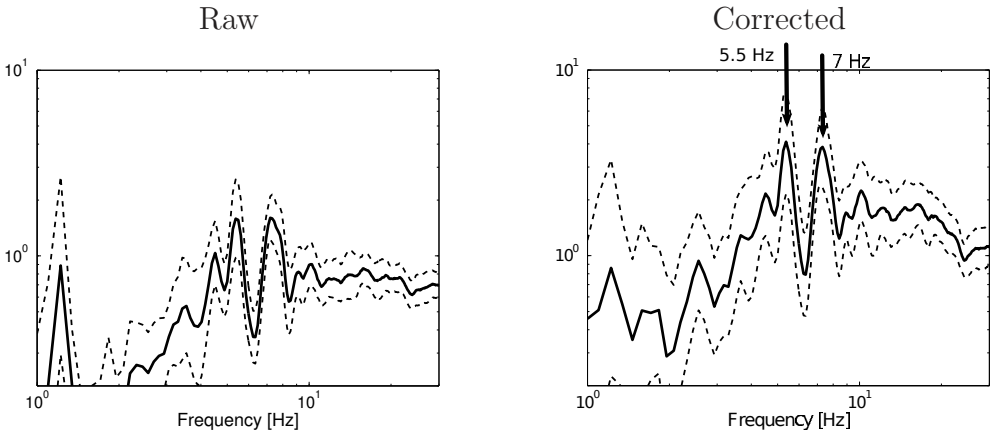

Figure 3.19: Crest over free-field spectral ratios; raw (left) and corrected (right). The difference between raw and corrected spectral ratios are far more pronounced, because measured ambient vibrations are very sensitive to changes in ambient conditions such ad temperature and centrifuge spin rate.

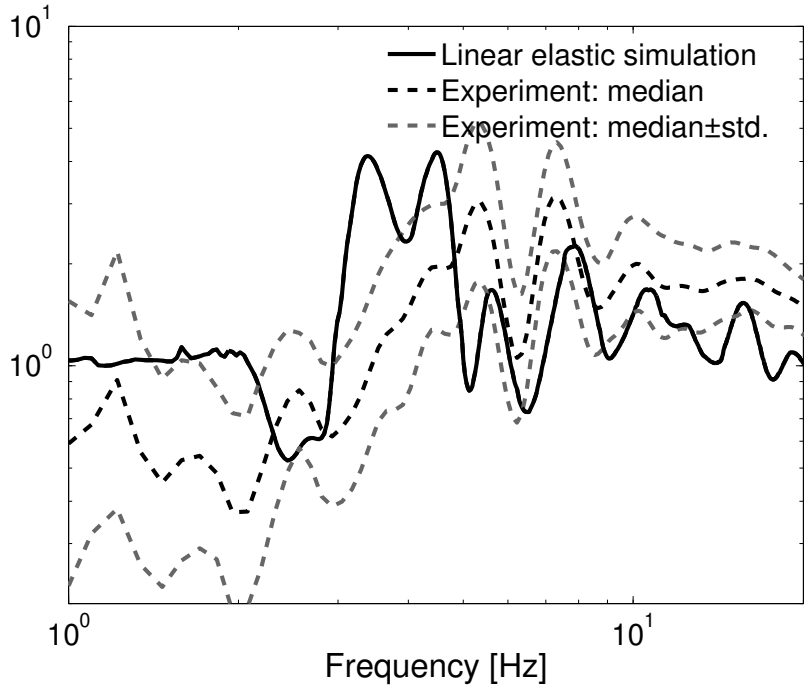

Figure 3.20: Comparison of low-strain crest over free-field spectral ratios: linear elastic numerical simulation vs measured ambient vibration.

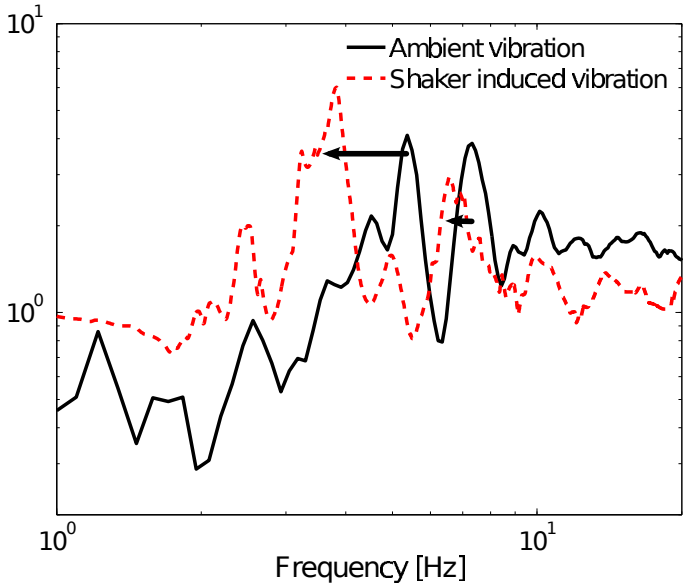

Figure 3.21: Comparison of experimental crest over free-field spectral ratios: ambient vibration vs shaker induced vibration.

3.3 Boundary effects of the centrifuge container

Considering that numerical simulations of all sloped models (of which the 30° is shown here) were found to be in excellent agreement with the experimental data, we proceeded with the assumption that the computed amplification ratio (solid line in Figure 3.17) was a realistic prediction of the empirical ratio that would have been measured, had the base plate motions of flat and sloped ground experiments been identical. We thus proceeded to examine the extent to which wave reflections from the container boundaries (laminar box and base plate) contaminated the experimental results.

3.3.1 Effects due to the lateral boundaries

We first examined the effects of the laminar box lateral boundaries. Flexible containers minimize boundary reflections by imposing symmetric horizontal and anti-symmetric vertical motion constraints at the model boundaries through the rigid rings [49, 58]. For a 1D profile subjected to 1D motion, the horizontal symmetry is

equivalent to a profile that extends laterally to infinity: since the left and right sides of the model are constrained to move in sync, two models could be *stitched* in series without changing the problem, then three and so on. Consider now a 1D profile with a scatterer (e.g. a hill, a boulder, a tunnel) subjected to uniform base motion. While the input motion and soil profile are 1D, the wavefield in the vicinity of the scatterer comprises shear, compressional and surface waves traveling in multiple directions. In turn, if the container boundaries are placed *too close* to the scatterer, this complex wavefield and the laterally constrained boundary response would differ, and this difference would cause spurious reflections. To avoid this artifact, the container sides should thus be placed *adequately far* from the scatterer, to allow the complex wavefield to dissipate, and the model response to converge to 1D, that is to say a motion compatible with the laminar box boundary conditions. *Too close* and *adequately far* in this case are not defined in absolute terms: since attenuation is proportional to the number of wavelengths travelled, higher frequency waves attenuate faster than lower frequencies in the same medium, and thus the former require shorter absolute distances to attenuate than the latter.

The configuration tested in the centrifuge comprised a horizontally stratified soil (1D) with the surface geometry acting as a scatterer, and was subjected to –approximately– uniform horizontal base motion (for the container and base plate rocking recorded motion, see Dafni [18]). Based on the discussion above, the container sides would not yield spurious reflections if the scattered wavefield (i.e. the non-1D scattered or diffracted waves) were allowed adequate distance to attenuate. The experimental design, however, entailed several conflicting constraints in this regard:

- The highest frequency (shortest wavelength) was bound by the actuator capacity ($f_{max} = 5.5Hz$);

- Because topography effects manifest for slope dimensions comparable to the dominant excitation wavelength [2, 5–7, 25], the actuator highest frequency also controlled the minimum dimensions of the model;

- On the same time, the experiment was designed with dense sand ($G_0 = 108MPa$) to prevent slope stability failure at small strains, and allow nonlinear effects to be tested; thus, at f_{max}, the shortest incident wavelength was $\lambda_{min} = 45m$, which in turn dictated an equally large slope to be tested; but then

- The fixed container dimensions were not adequate to accommodate the minimum distance ($3\lambda = 135m$) that the toe and crest of the slope should be having from the boundaries to avoid spurious reflections [3]

Given these constraints, Dafni [18] inevitably compromised the slope-to-boundary distance. We examined the effects that the consequent boundary reflections had on the recorded topographic amplification patterns by means of the finite element model shown in Figure 3.23. The material and slope geometry were identical to the centrifuge configuration, but the container box was replaced by paraxial absorbing elements that minimize energy reflections back into the numerical domain [16]. In other words, the numerical model in Figure 3.23 is a slope on the surface of a Nevada sand layer overlying an *almost* rigid bedrock (here, the aluminum base plate).

Boundary effects were revealed clearly when we examined the spatial distribution of peak (absolute maximum) acceleration on a model cross-section. Figure 3.22 compares the peak acceleration contours produced by the free-field numerical and centrifuge experimental models, for three different broadband ground motions of increasing intensity. In the free-field simulations, the maximum amplification -albeit small- appeared in the vicinity of the crest, and the response gradually approached 1D conditions both behind the crest and away from the toe. The amount of amplification also appeared to increase with increasing motion intensity; specifically in the

stronger of the three motions, the topographic amplification distribution strongly resembles the displacement field of a slope stability failure. By contrast, the maximum amplification appears on the top left corner of the centrifuge experimental model in all three cases showed in Figure 3.22. Considering that the interface between soil and container –the interface of a granular medium and a metal surface– has practically no cohesion, the top corner of the model responds during load reversal as a vertical (90°) slope, much more prone to localized amplification and slope stability failure than the 30° slope.

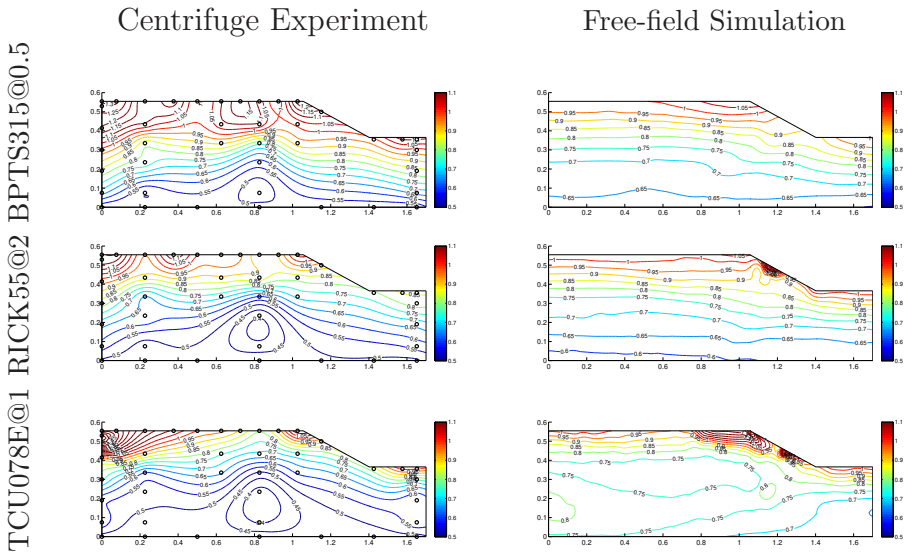

Figure 3.22: Snapshots of maximum acceleration contours: container boundary vs free-field boundary: The first row represents the result from BPTS315 recording scaled by 0.5, the second row is from RICK55, a train of narrow-band pulses, scaled by 2 and the third row is from TCU078E recording unscaled

We then investigated the effect of lateral boundary on the crest-to-free field spectral ratio. Figure 3.24, compares the spectral ratio from the model shown in figure 3.23 with the spectral ratio from the full container model. Even though the comparison of maximum acceleration contours shown in figure 3.22 revealed significant boundary effect near the boundary, we found insignificant difference from the comparison of crest-to-free field spectral ratios. This suggests that, although the boundary configuration during centrifuge experiments was less than ideal, waves reflected from the

lateral boundaries had enough attenuation before they reach the crest, and the modification of wavefield due to the lateral boundary reflection was small enough at the central part of the model, near the slope crest.

Figure 3.23: Finite element mesh with free-field boundary condition. The material and slope geometry are identical, but the model (soils and the aluminum base plate) is further extended to minimize the lateral boundary effect. Lateral boundaries are treated with paraxial absorbing elements.

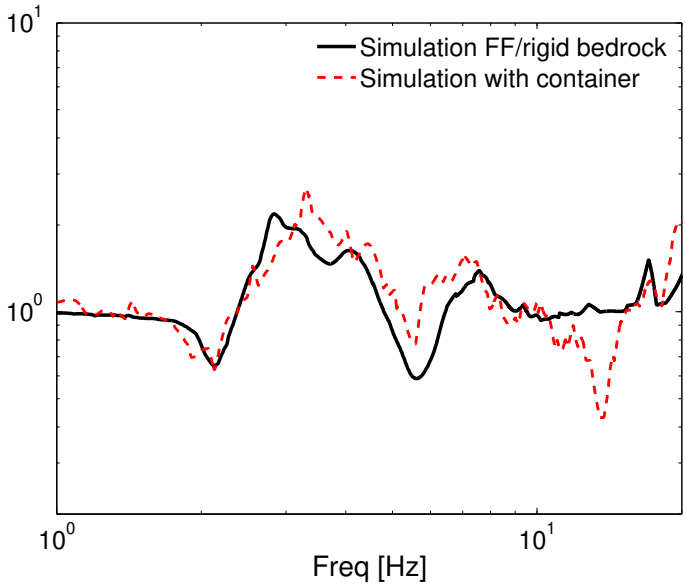

Figure 3.24: Comparison of spectral ratios at the crest relative to the free field. The difference between two curves represent the effect of lateral boundary on the crest-to-free field spectral ratio.

3.3.2 Boundary effects of the base plate

We next examined the contribution of the base plate to the observed topographic amplification. For this purpose, we constructed a numerical model of a slope on the

surface of a Nevada sand layer overlying a halfspace, shown in Figure 3.23 as well: here, both side boundaries and base plate were replaced with paraxial absorbing elements [16], and the incident motion was introduced in terms on incident stress. For more details on free-field boundary conditions for 2D site response problems, see Assimaki et al. [5, 6].

Figure 3.25 compares the horizontal acceleration time histories of the free-field halfspace model to the centrifuge recordings along a surface array of sensors. The base plate and lateral boundary effects appear to be negligible. However, a closer look reveals that the underlying reason lies on the experimental design constraints described above. Altough the actuator of the centrifuge shaking table has excitation frequencies up to $300Hz$ ($5.5Hz$ at $55g$), recorded baseplate accelerations often have dominant frequencies less than $4Hz$. Using an average shear wave velocity ($V_s = 230m/s$) of the sand, the dominant wavelengths were often in the order of ($\lambda = 100 \sim 200m$), approximately one order of magnitude longer than the slope dimensions (H=11m; W=19m). Since topography effects manifest for wavelengths comparable to the feature dimensions [2, 5, 6, 11, 25], topographic amplification appears not to have been the dominant amplification feature in this experiment. In fact, all stations depicted in Figure 3.25 have practically identical traces –a 1D site response experimental outcome. What thus initially appeared to be indicative of negligible boundary effects, was in fact the 1D response of the fundamental soil column mode, for which (as mentioned above) the flexible container boundary constraints are ideal boundary conditions.

Comparison of the frequency ratios of surface–to–baseplate motion shown in Figure 3.26, measured during the sloped and flat ground model tests reveal a similar observation in low frequencies: the crest to baseplate ratio from the former experiment, and the flat ground to baseplate ratio from the latter are almost identical in the frequency range 1-3Hz. In other words, in the frequency range of shaking ($1 \sim 2Hz$),

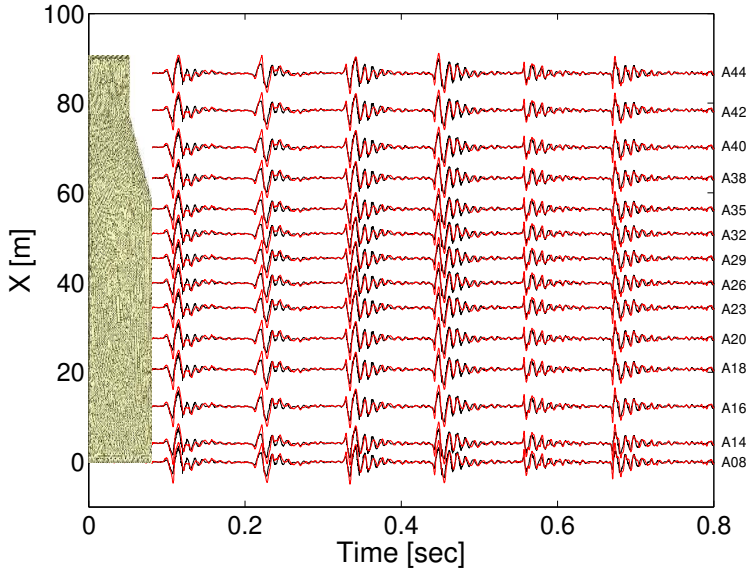

Figure 3.25: Synthetic seismograms comparing the responses from two different model configurations: container boundary vs free-field boundary.

the two models have identical, 1D site response. At frequencies higher than 3Hz, however, we observed a clear evidence of topography effects, causing the differences in amplitude at $3.5Hz$ and $6.5Hz$, which manifest as topography amplification peaks in the ratio A^h_{Crest}/A^h_{ff} shown in Figure 3.16.

We next compared the experimental topographic amplification factor (obtained from shaker induced motions and corrected using equation (5)) to the numerical amplification factor of the free-field halfspace model, defined by equation 6:

$$SR_{Crest} = \frac{A^h_{2D}(\omega)}{A^h_{ff}(\omega)} \tag{6}$$

where $A^h_{2D}(\omega)$ and $A^h_{ff}(\omega)$ here describe the Fourier amplitude spectra of the response behind the crest and in the far-field respectively, computed on the surface of the same model as shown in Figure 3.23; by contrast to equation (5), no correction was necessary in this case.

Figure 3.27 compares the two factors, and reveals fundamental differences between the numerical free-field halfspace model and the centrifuge experimental results: the

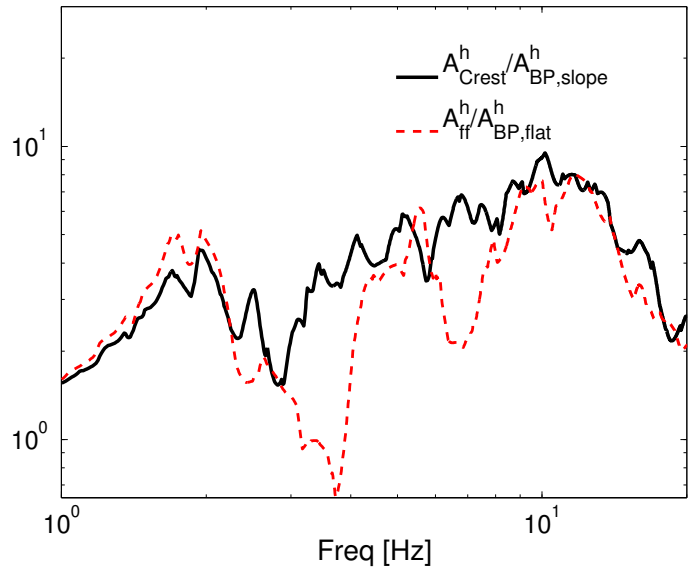

Figure 3.26: Comparison of surface to baseplate spectral ratio for flat and slope model. The peak at $2Hz$ represents the fundamental mode of 1-D site response, which is almost unaffected by the topography effect.

former shows practically no topographic amplification in the entire frequency range 1-20Hz. Comparison between the free-field numerical models with and without baseplate (also in Figure 3.27), both free of boundary reflections from the centrifuge box, shows that the topographic amplification (at 3∼4Hz and 7∼8Hz) of the 30^o slope on the surface of the tested soil manifested almost entirely as a consequence of energy reflections by the baseplate. In other words, the base plate in this 2D model trapped and amplified propagating waves –including the inclined reflected, converted and scattered from the surface slope– similarly to a 1D soil layer overlying bedrock. However, the traditional approach of normalizing the 2D response at the crest by the corresponding 1D surface motion does not remove the additional 2D amplification caused by the stiff layer; the topographic amplification with rigid layer is thus higher than the one resulting from the same geometry on a halfspace.

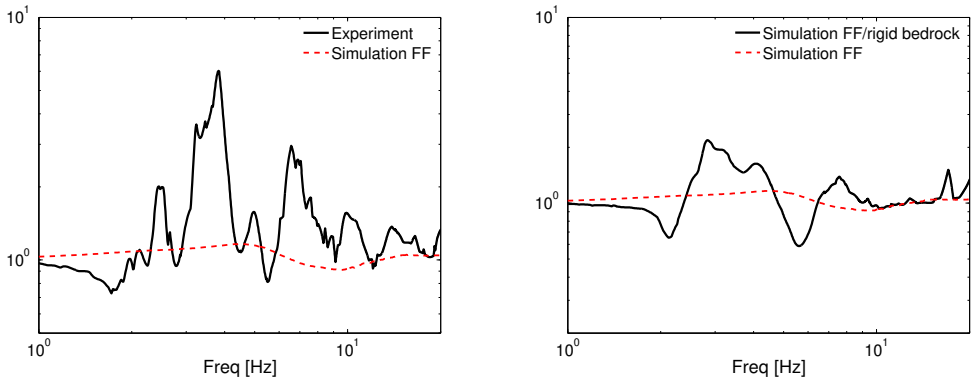

Figure 3.27: Spectral ratios at the crest relative to the free field: container boundary vs free-field boundary. Horizontal accelerations recorded at the crest with halfspace model show negligible topography effects, indicating the topography effect observed during experiments are highly attributed to the presence of rigid baseplate.

3.4 Conclusions

We presented a study where numerical simulations were used to understand and extend a study of centrifuge experiments on topographic amplification. First, we used the experimental data to validate the numerical models. Then, we identified limitations of the centrifuge experiments pertaining to conflicting constraints of frequency input, material stiffness, slope size, and container dimensions. Unavoidable trade-offs in the experimental design by Dafni [18] led to compromises in the distance of the scatterer (the slope) from the boundaries: instead of the recommended distance of 2∼3 wavelengths (100∼150m in this case), the crest-boundary distance was 55m, and the toe-boundary distance 14m, which in turn yielded spurious reflections. However, we found that the boundary effect had little significance on the crest-to-free field spectral ratio. We also showed that the experimental design constraints also led to propagating wavelengths several times larger than the slope, and that these pulses were not fine enough to clearly *see* –and be modified by– the topographic feature: thus, the dominant mode in the observed surface motion was the 1D site response of the sand layer. Nonetheless, topography effects did manifest. Our study showed,

most importantly, that the baseplate (or a stiff underlying layer in a free-field configuration) was instrumental in trapping and amplifying the non-1D scattered waves, and that in absence of those reflections, topographic amplification would have been negligible. We finally demonstrated that the baseplate role was much more significant than the lateral boundary reflections, which mostly contributed to artificially increasing the peak amplitudes at 3∼4Hz and 7∼8Hz.

The experiments by Dafni [18] and our study suggest that topography effects are significantly affected by the underlying soil stratigraphy. Ground motion amplification on the crest in excess of 1D response was much more pronounced when we added a stiff layer several feet below, indicating that soil amplification is coupled to topography effects. Paolucci et al. [40] and Grazier [26] have also made similar observations during site specific case studies. This finding is contrary to procedures of European design codes [20] and seismological models –where topography effects are by and large superimposed to 1D soil amplification factors. On the other hand, among the scarce recordings of exceptionally high ground motions, several have been linked to topographic amplification [55]; and since engineering design procedures rely increasingly on earthquake scenario simulations, *2D/3D site effects* such as the ones presented in this paper are likely to play a particularly important role in ground motion predictions for infrequently large earthquakes, and thus in the design of critical infrastructure. In this context, our study indicates that coupling of soil response and topography effects is an important, poorly understood phenomenon that merits additional research.

Finally, our results show that complementing centrifuge experimental data with numerical simulations can significantly extend the parametric research space of geotechnical earthquake engineering studies. Even in the case of experimental results contaminated with boundary effects, numerical methods enabled us to disentangle them, and to demonstrate that flexible container centrifuge tests can be successfully used

to deepen our understanding of non-1D site response problems.

3.5 Acknowledgements

This material is based upon work supported by the National Science Foundation under Grant No. CMMI-0936543 with title "NEESR-CR: Topographic Effects in Strong Ground Motion - From Physical and Numerical Modeling to Design". Any opinions, findings, and conclusions or recommendations expressed in this material are those of the author(s) and do not necessarily reflect the views of the National Science Foundation.

CHAPTER 4

Parametric investigation of topography effects coupled to nonlinear site response for pressure-dependent media

4.1 Introduction

Topography effects, modification of intensity and frequency contents of seismic motions by strong topographic relief, are known to play a significant role in elevating seismic risks. Observations from historical earthquakes have shown that a pronounced topographic relief may significantly aggravate the intensity of strong ground motions, often causing localized yet extensive damage to structures located at the top of hills, ridges and cliffs. Examples of such observations were made in the 1976 Friuli earthquake in Italy [14], 2010 Haiti earthquake[4, 29], and 1985 Chile earthquake [15], among various others [3]. The case of pacoima dam record (PGA=1.25g) [10] during the 1971 San Fernando earthquake and the Tarzana record (PGA=1.8g) [12] during the Northridge earthquake are two particular examples of such phenomenon.

An extensive extensive amount of work has been done in the past 40 years, to understand the mechanism of the topography effect. This effort can be devided into three categories: 1) analytical solutions [46–48]; 2) numerical models via finite difference, finite element, boundary element, and discrete wavenumber method [2, 5,

6, 10, 11, 39]; and 3) physical model studies utilizing geotechnical centrifuge facilities [18, 34, 38].

However, that most of the previous work has been limited to overly simplified models, often utilizing linear-elastic homogeneous half space with simplified geometries, even though in reality topography effects are rather complex phenomena often affected by the velocity structures and response characteristics of substrata. A limited number of examples, which involves more complex models such as soil layering, three dimensional and/or complicated surface geometries can be found in [2, 9, 13, 25, 40, 45]; but very few [5, 6] have studied the effect of nonlinear soil response on topographic amplifications.

The general consensus drawn from those work, as stated by Geli et al. [25] and Bard [8] is that: 1) the theoretical predictions agree with observations in a qualitative manner, 2) the approximate frequency of this amplification corresponds to the wavelengths comparable to the characteristic dimension of topographic features, and 3) theoretical predictions often underestimates the observed amplifications.

Altough it is widely recognized that topographic amplification can elevate seismic risk, there is currently no consensus on how to reliably quantify its effects. Often, observed amplifications are much higher than the predictions from analytical solutions and numerical simulations. This discrepancy has been attributed, among other reasons, to the lack of realistic soil conditions in predictive models on topographic amplification.

Recently, a series of centrifuge experiments tested the seismic response of single slopes of various inclinations at NEES@UCDavis facility, to investigate the role of nonlinear soil response on topographic amplifications. As part of this collabolative research, we performed a set of detailed parametric numerical simulations, to study the effects of slope size, velocity structure of the soil that constitutes the slope, presence of the bedrock and nonlinear response of soils on topographic amplifications.

We constructed a finite element model, first validated by comparisons with centrifuge experimental data by Dafni [18] then extended to a free-field configuration (free of the container box and the baseplate). We first studied the effects of slope size on topographic amplification and confirm that topography is function of $f \times h/V_s$, the slope height normalized by the wavelength. Next we investigate the effect of a low velocity zone on top of a slope, considering various depths of the soft zone and the impedance contrast at the interface. We then studied the role of high velocity zone (bedrock) beneath the slope, which is often neglected in the numerical predictions partly because of the inherent difficulties in identifying the depth and mechanical properties of bedrocks in-situ. Finally we presented our result on the effect of the nonlinear soil response on topographic amplifications.

4.2 Numerical model and soil constitutive parameters

We performed the time domain non–linear finite element analysis using DYNAFLOW^{TM} [42]. Figure 4.1 shows the mesh of the numerical model, in which the slope has an angle of 30° and the height of 11 m. We used absorbing boundaries to simulate the semi infinite halfspace with a finite domain. Detailed descriptions on treating the boundary condition are described in the work by Assimaki [3].

Figure 4.1: Finite element mesh of the model.

The physical model was constucted with dense nevada sands that has a relative density, $D_R = 100\%$; the dynamic response characteristics of dense nevada sands are documented in Stevens et al. [54]. We modeled the pressure dependency of the elastic

moduli of Nevada sand with a power law equation shown in (7).

$$G = G_0 \left(\frac{p}{p_{ref}} \right)^n \tag{7}$$

Figure 4.2 shows the shear wave profile of Nevada sands with $D_R = 100\%$, previously measured by Stevens et al. [54] using low strain signals generated by an air hammer attached to the centrifuge container base plate. Black dashed line shows the fitted velocity profile using the power law equation, which we used for initially constructing the numerical model. We then re–calibrated the velocity profile using the results from the centrifuge experiments of flat ground model by Dafni [18], which is shown in black solid line in the figure.

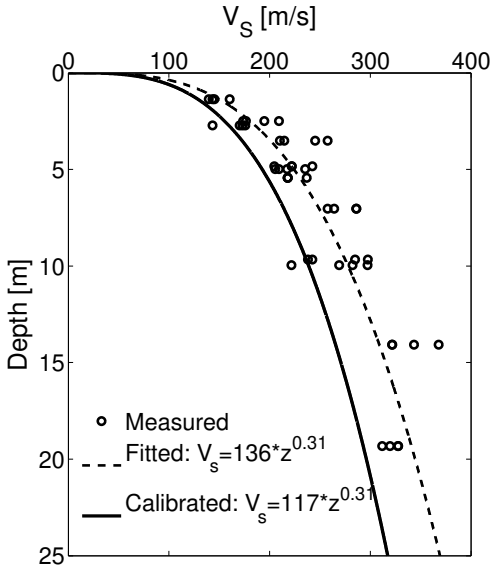

Figure 4.2: Shear wave velocity profiles: Initial estimation based on the measurements by Stevens et al. [54] and the final calibration

To predict the nonlinear response characteristics of Nevada sands, we employed the pressure dependent multi yield (PDMY) plasticity model by Prevost [41, 42], with a purely kinematic hardening rule and round-cornered Mohr-Coulomb yield surfaces. The model assumes the associated flow rule for the deviatoric strains and a non-associated flow rule for the volumetric plastic strains.

The monotonic shear stress-strain response of the soil is simulated using the generalized hyperbolic model by Hayashi et al. [28] shown in Equations (8) and (9):

$$f(x,n) = \frac{\left(\frac{2}{n}x+1\right)^n - 1}{\left(\frac{2}{n}x+1\right)^n + 1}; n > 0 \tag{8}$$

$$y = e^{-\alpha x} \cdot f(x, n_L) + (1 - e^{-\alpha x}) \cdot f(x, n_U) \tag{9}$$

where x is the shear strain (γ) normalized with respect to the reference strain $\gamma_r = \tau_f/G_{max}$, τ_f and G_{max} are the soil shear strength and maximum shear modulus respectively, y is the shear stress τ normalized with respect to the shear strength, $y = \tau/\tau_f$, and α, n_L and n_U are three model parameters. Hayashi's model combines two standard hyperbolic models [27] as shown in Equation (9), but reduces to the standard hyperbolic form when $n_L = n_U = 1$. Such a versatile formulation was necessary to allow simultaneous matching of the soil's shear modulus (G_{max}) (at low strains), and ultimate shear strength (τ_f) (at high strains).

Figure 4.3 shows the fitted curve and the corresponding backbone curve at the reference pressure $p_{ref} = 100kPa$; a modulus reduction curve model developed by Darendeli [19] is also plotted for a comparison purpose. We assigned higher weight to G_{max} and ϕ, and lower weight to the intermediate strain range values in our calibration, which explains why our model deviates from the Darendeli [19] curve at the same reference pressure. The soil parameters at the end of the calibration phase that were used in the simulations described below are summarized in Table 4.1.

Table 4.1: Material parameters calibrated for dry Nevada sand at relative density $D_R = 100\%$

$\rho\ [Mg/m^3]$	ν	$G_0\ [MPa]$	$p_{ref}\ [kPa]$	n	$\phi\ [^\circ]$	$\Psi\ [^\circ]$	X_{pp}	α	n_L	n_U
1.7	0.25	108	100	0.62	42	35	0.05	0.4	0.5	1.0

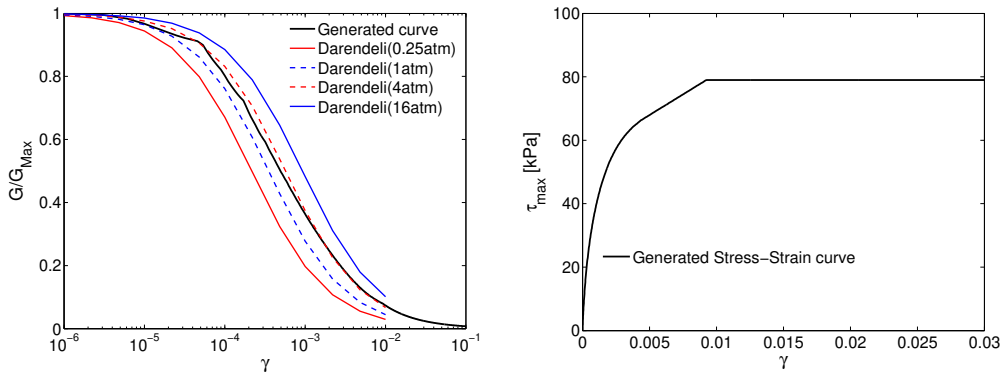

Figure 4.3: Modulus reduction curve and the corresponding $\tau - \gamma$ curve at the reference pressure $p' = 100\,kPa$.

4.3 Input ground motions

In this study, we considered vertically incident, in-plane shear waves. We used a train of ricker wavelets as an input motion, applied at the base of the model as prescribed shear stresses, converted from a velocity time history. The input velocity time history consists of three ricker wavelets, with central frequencies of $f_0 = 1.8\,Hz$, $7\,Hz$ and $20\,Hz$, to ensure it covers a wide band of frequencies. We used a low intensity motion first, with peak incident velocity of $0.003\,m/s$, and studied the study the effect of the slope height, thickness of the low velocity zone, impedance contrast at the interface, and the presence of bedrock. We then analyzed our model with ground motions of increased intensities, to investigate the effect of nonlinear soil response. Figure 4.4 shows the incident velocity time history we applied at the base of the model, and its fourier amplitude spectra.

4.4 Slope height as frequency-dependent scaling parameter

We analyzed models of three different slope heights: $h = 5.5\,m$, $11\,m$ and $22\,m$, to evaluate the effect of slope height on topographic amplification. The original model had a height of $h = 11\,m$, two other models are scaled versions of the original model, where every dimension of the model is scaled in proportion to the slope height. We

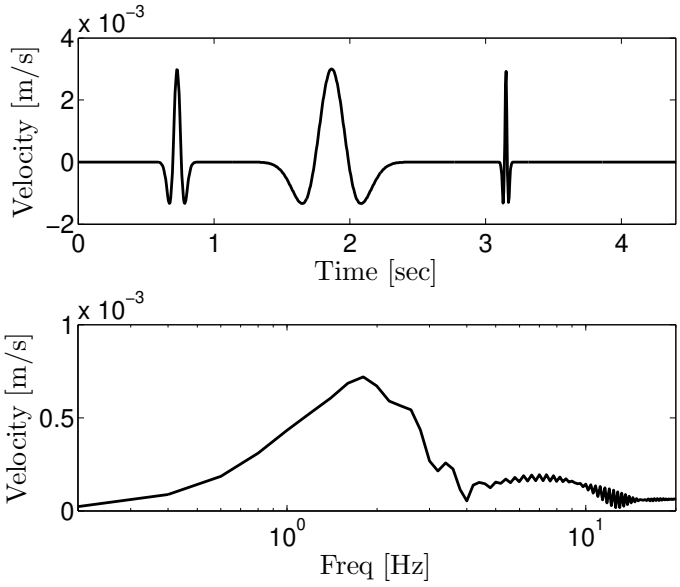

Figure 4.4: A time history (top) and and its fouries amplitude spectra of input velocity; it consists of three ricker wavelets with $f_0 = 1.8\,Hz$, $7\,Hz$ and $20Hz$ to ensure the coverage on a wide range of frequencies, and scaled to a low peak value of $0.003\,m/s$.

kept the same pressure dependent velocity profile for all three model configurations, as shown in figure 4.2, which results in the average shear wave velocities of $Vs = 190m/s$, $234\,m/s$ and $289\,m/s$, respectively for the slope height of $h = 5.5\,m$, $11\,m$ and $22\,m$.

Figure 4.5 shows the spectral ratios of horizontal accelerations obtained at the slope crest, normalized by the corresponding free-field acceleration. The figure on the left shows that slopes with different heights amplify the accelerations at different frequencies; generally, slopes with larger height is associated with amplifications in lower frequencies, and vice versa. Also, the result shows about 20% of maximum amplification compared to the free-field accelerations, regardless of slope heights. On the right, we plotted the same spectral ratios, but now in terms of normalized slope height, $f \times h/V_s$. The figure shows that the topographic spectral ratio scales nicely in terms of the normalized slope height; this confirms previous studies [2, 25] stating that the characteristic slope dimension normalized by the wavelength is an important parameter that governs the topographic amplification.

We then plotted, in figure 4.6, the spectral ratio of vertical accelerations, obtained at the crest and normalized by the horizontal free-field acceleration. We will stress that the input motions are vertically propagating, in-plane shear wave, therefore the free-field accelerations would be free of vertical component. This vertical component, refered to as parasitic vertical accelerations, is a result of mode converted S-waves and the Rayleigh waves due to the slope inclinations. Vertical accelerations at the crest show about 30% of maximum amplitude ratio compared to the free-field accelerations. Again, it appears the slope height has no significant effect on the amplitude of topographic spectral ratios and the first peak appears at the same normalized slope height $f \times h/V_s = 0.2 \sim 0.25$ as the horizontal component.

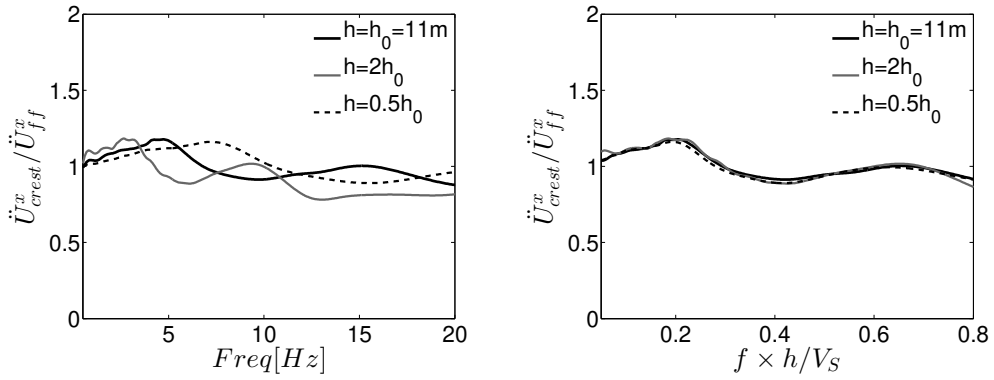

Figure 4.5: Effect of slope height on the spectral ratio of horizontal ground motion at slope crest

4.5 Near-surface impedance contrast: Low velocity layer

We studied the effect of low velocity zone near the surface at the back of the slope. Figure 4.7 shows the schematic diagram of the model for this study. We considered two different cases for the depth of the soft layer $h = 4\,m$ and $8\,m$ and compare the result with the original velocity profile without any large velocity jump; the height of the slope is $11\,m$.

We also studied the effect of impedance contrast at the interface of low velocity

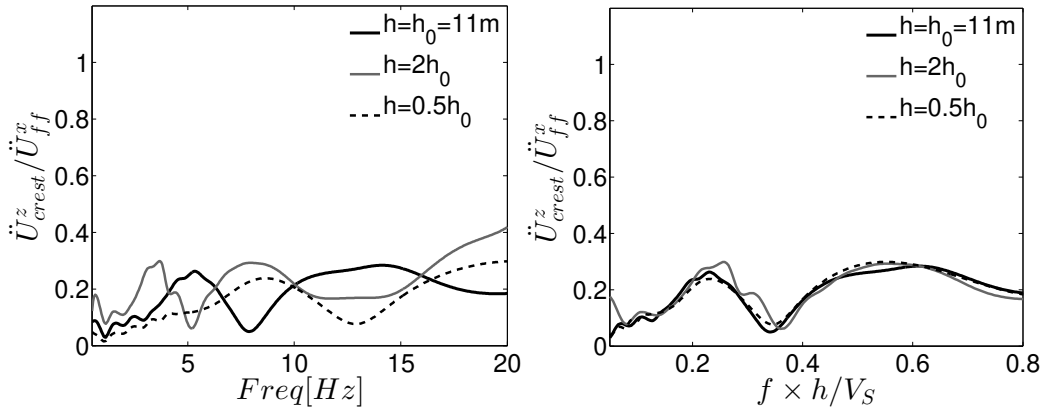

Figure 4.6: Effect of slope height on the spectral ratio of vertical ground motion at slope crest

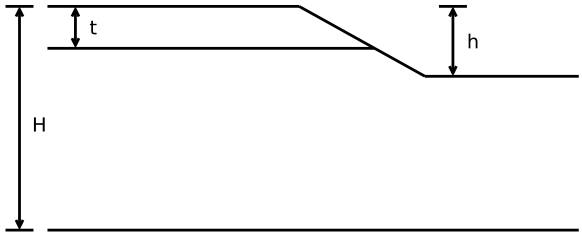

Figure 4.7: Schematic diagram of the model with low velocity zone near the surface at the back of the slope; we studied the effect of depth h of the low velocity zone and the impedance contrast at the interface.

layer. In this study, the impedance contrast at the interface is defined as

$$\alpha = \frac{\rho_l V_{sl}}{\rho_u V_{su}} \tag{10}$$

where ρ_l and V_{sl} are the density and the shear wave velocity of lower layer, and ρ_u and V_{su} are the density and the shear wave velocity of upper layer, respectively. Three different values of impedance contrast, $\alpha = 1.5$, 2 and 3, are considered and compared to the response with the original velocity profile. The summary of velocity structures considered in this study is shown in figure 4.8, where the left and right figures show the velocity structures with the depth of soft layer $h = 4\,m$ and $h = 8\,m$, respectively.

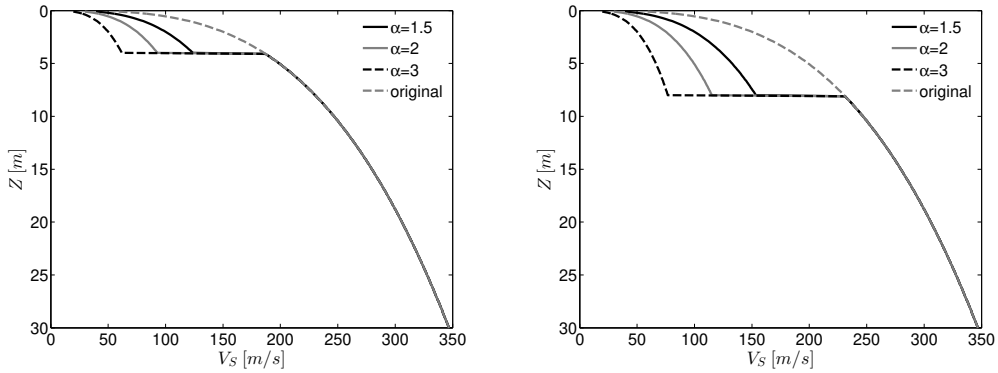

Figure 4.8: Shear wave velocity profiles at the back of the slopes

4.5.1 Effects of layer thickness

We summarized the result of parametric studies on the effect of the thickness of surficial low velocity layers in figure 4.9. We analyzed two different profiles ($h = 4\,m$ and $h = 8\,m$) for impedance contrast valued of $\alpha = 1.5$, 2 and 3. In the figure, we plotted the spectral ratios computed at the crest for the horizontal and vertical components, and compared the result to the spectral ratios we obtained from the original profile.

Our result shows that the presence of soft layer can dramatically shift the frequencies where topography effect dominates. It seems that, overall, deeper soft layers are

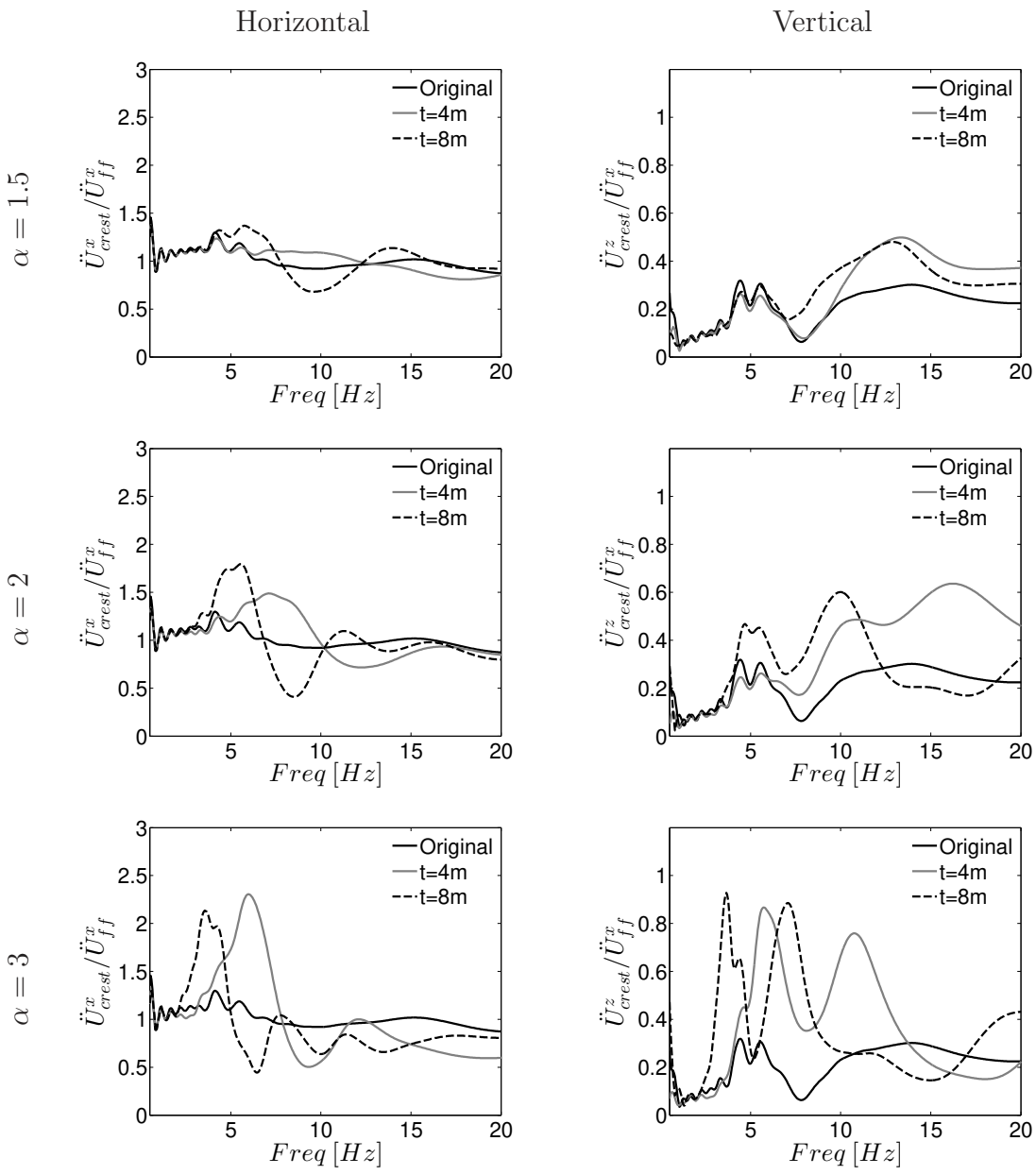

Figure 4.9: Effect of the thickness of soft soil layer on the horizontal (left) and vertical (right) component spectral ratios computed at the crest; the first, second and third column correspond to the impedance ratios at the interface $\alpha = 1.5$, 2 and 3, respectively .

associated with amplifications in lower frequencies, because the presence of a deep soft layer near the surface changes apparent shear wave velocities, while the two different depth profiles show little differences in maximum amplification factors. Also, we found that the vertical component spectral ratios have two distinct peaks, and that the peaks at higher frequencies are much more sensitive to the changes in the depth of surficial low velocity layers.

4.5.2 Effects of impedance contrast

Figure 4.10 shows the variation of crest-to-freefield spectral ratio with increasing impedance contrast at the interface of the low velocity layer. Unlike the effect of the depth of the soft layer, where we only observed a significant effect in terms of frequencies, the changes in impedance contrast seems to drastically alter both the amplitude and frequency contents of the spectral ratios. The result of our parametric study suggests the maximum amplification factor increases monotonically with increasing impedance contrast, both in horizontal and vertical components; while the overall shape of the spectral ratio becomes more and more complex, showing multiple peaks and troughs at different frequencies. This finding has a significant practical implications, because many natural and man-made slopes such as cut-slopes, coastal bluffs and tectonic uplifts share velocity structures similar to our model configuration.

We also observed very high amplitude of the parasitic vertical accelerations, reaching 60% and 90% of the free-field horizontal components for impedance contrasts $\alpha = 2$ and 3, respectively. We believe that this high amplitude parasitic accelerations require a special attention; although traditionally vertical accelerations has been mostly neglected in structural design procedures, vertical accelerations induced by a topographic feature is strongly rotational, resulting in the increased moment demand to nearby structures.

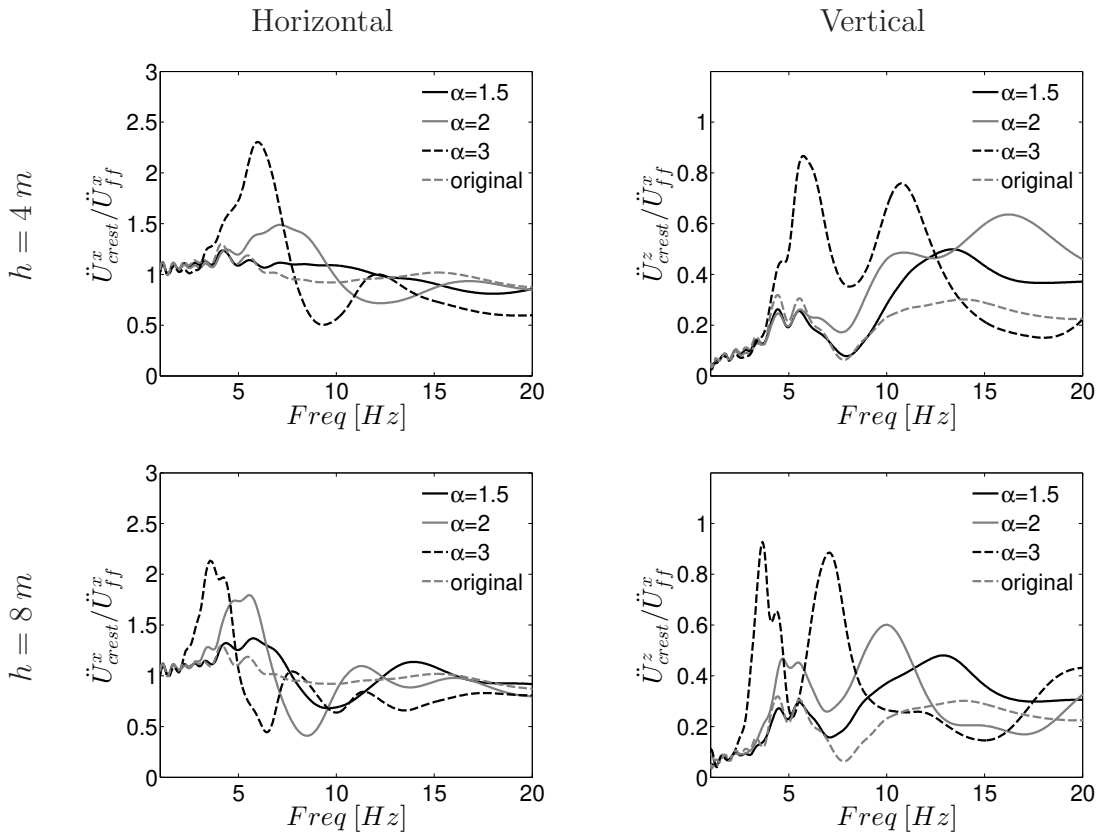

Figure 4.10: Horizontal and vertical spectral ratios at the crest with different, showing the effect of impedance contrast at the interface of soft layer; $t = 4m$ (top) and $t = 8m$ (bottom)

4.6 Impedance contrast at depth: Elastic bedrock

In this section, we present the effect of a deep high velocity zone (i.e. bedrock) on topographic amplifications. This time we added another layer of elements at the base of our numerical model, with impedance contrasts at the soil-bedrock interface $\alpha_B = 1.5$, 2 and 3. The soils above the bedrock layer has our original velocity profile: smooth pressure dependent shear wave velocities monotonically increasing with depth.

The result of our simulations is summarized in figure 4.11. Our result suggests that the presence of bedrock beneath the slope can increase amplitude of crest-to-freefield spectral ratios, both for horizontal and vertical components. With our model configurations, the amplitude of vertical components were more sensitive on the soil-bedrock impedance contrast, compared with the horizontal components. Also, we observed a monotonic increase of maximum topographic amplification factors with increasing soil-bedrock impedance contrasts, while we didn't observe significant changes in the frequency contents at this time. The result showed no significant effect of soil-bedrock impedance contrast at higher frequencies either; it seems the presence of a deep high velocity zone would just increase the amplitude of spectral ratios, near its first peak. Figure 4.12 shows the effect of increased soil-bedrock impedance contrast on the crest-to-free field spectral ratios at $f = 4.4Hz$.

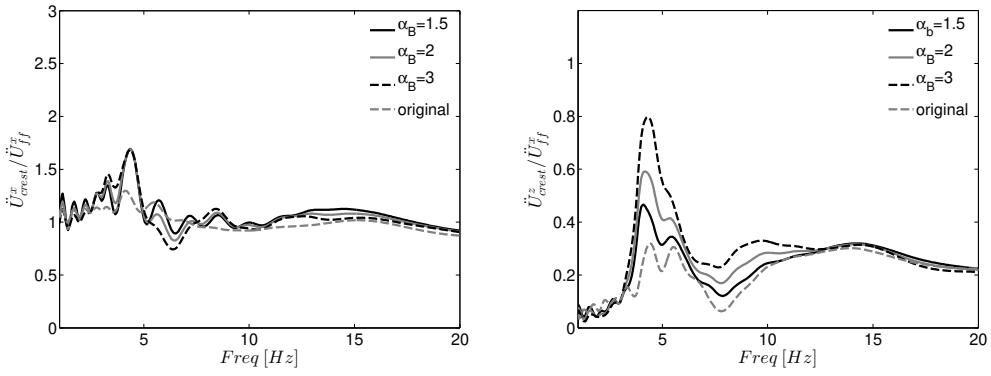

Figure 4.11: Effect of the impedance contrast at the interface with deep high velocity zone on the crest-to-spectral ratios for horizontal (left) and vertical (right) component.

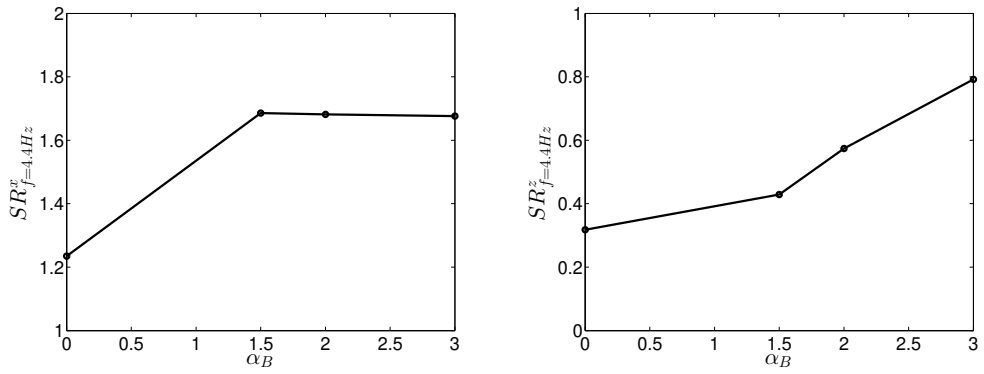

Figure 4.12: Effect of the impedance contrast at the interface with deep high velocity zone on the crest-to-spectral ratios at $f = 4.4Hz$.

4.7 Effect of nonlinear soil response

So far our studies have been done with input ground motions with relatively weak intensity. To study the effect of nonlinear soil response on topography effects, we analyzed our model using input motions with increased intensities. We scaled the amplitude of our input velocity time histories to $u^i_{max} = 0.003$, 0.01, 0.04, 0.08 and $0.1\, m/s$.

Figure 4.13 shows the effect of increasing peak input velocity on the crest-to-freefield spectral ratios, with our original model velocity profile shown in figure 4.2. Our result shows significantly increased amplification factors for peak incident velocities higher than $0.04\, m/s$. This trend is also depicted in figure 4.14, which describes the effect of ground motion intensities on crest-to-free field spectral ratios at $f = 4.4Hz$ and $15Hz$. Also the parasitic vertical components seems to be more sensitive to the soil nonlinearity, especially for the higher frequencies. We observed very large amplitude in high frequency vertical components, exceeding the amplitude of free-field horizontal components with peak incident velocities higher than $0.08\, m/s$.

We would like to point out the peak incident velocity of $\dot{u}^i_{max} = 0.1\, m/s$, which would result in the PGV of $0.2 m/s$ or higher, is very commonly found in the database of recorded grond motions and is usually associated with moderate to strong events

with PGA ranges of $0.1 \sim 0.6\,g$. Although, in our model, this high amplitude vertical accelerations are observed in frequencies higher than $10\,Hz$, this could happen in much lower frequencies as well; should a slope have a same velocity profile and same geometry but with 4 times larger height, this effect would be observed in frequencies at about one fourth of the original frequencies.

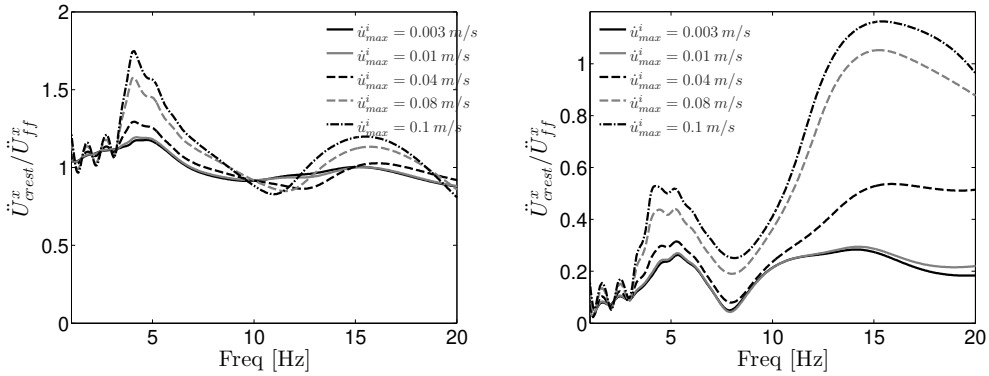

Figure 4.13: Effect of ground motion intensity on crest-to-free field spectral ratios with pressure dependent soil, subjected to ricker wavelets

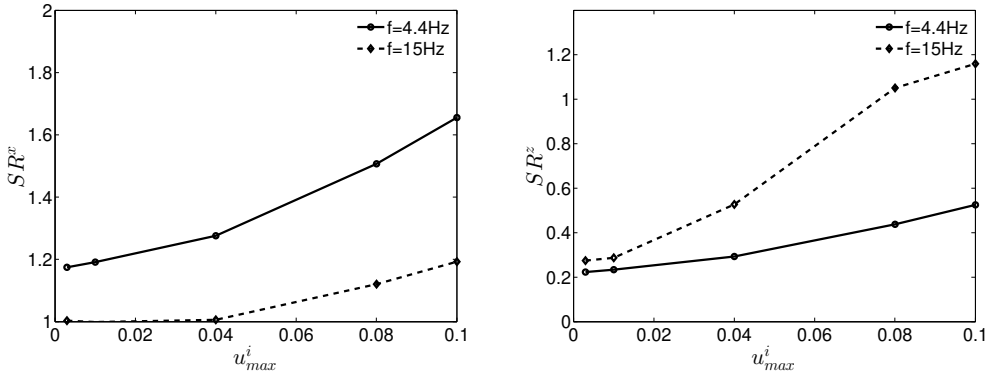

Figure 4.14: Effect of ground motion intensity on crest-to-free field spectral ratios at $f = 4.4Hz$ and $15Hz$ with pressure dependent soil, subjected to ricker wavelets

We then simulated our model, this time with a pressure independent-homogeneous soil profile, with low strain shear wave velocity of $V_s = 230m/s$, the average shear wave velocity of our original profile. Therefore the strength of soil is uniform, regardless of the depth; shallow layers would have significantly more strength compared to the original configuration. The result of this simulations is summarized in figure 4.15.

Although this model has the same average shear wave velocity up to $30\,m$, the result shows a remarkable difference compared with the original configuration. Overall, the crest-to-freefield spectral ratios computed from this model shows lower amplitudes, even for the ground motions with smallest intensity considered. Also it shows little effect of increased ground motion intensity on topographic amplifications.

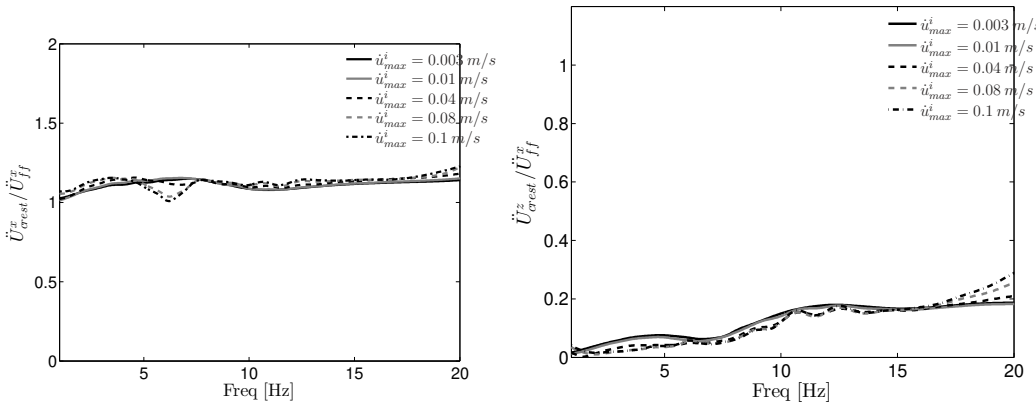

Figure 4.15: Effect of intensity on horizontal component at slope crest with pressure idependent soil, subjected to ricker wavelets

Our result suggests that aggravation of toopgraphic amplification due to the soil nonlinear response is a result of instantaneous decrease in the effective shear wave velocities (increase of impedance contrasts) of soft surficial layers. Our model with pressure dependent velocity gradient would be especially susceptible to this phenomenon, since the shallow surficial layers have very low strength; this also explains why the higher frequencies are more sensitive to the increase of ground motion intensities. The result from the pressure independent velocity profile–which already shows less topographic amplifications due to the reduced velocity gradient–exhibits little dependence on the intensity of ground motions we considered, most likely because the ground motions we considered were not strong enough to cause any significant nonlinear response of shallow soil layers.

4.8 Conclusions

In this study, we presented the result of a detailed parametric investigation on the topographic amplification of strong ground motions, near the crest of a single faced slope. Using a finite element model, validated in comparison with a set of centrifuge simulations [18], we studied the effect of slope height, the effect of low velocity zones near the surface, the effect of deep high velocity zones and the effect of soil nonlinear responses.

Our result suggests that the slope height, normalized by the wavelength, governs the frequency at which topography effect dominates; yet it has little to no effect on the maximum topographic amplification factors.

A low velocity zone, near the surface at the back of single sided slopes, can have a significant impact on topography effect, in terms of both the frequency content and amplification factors. The result suggests that the impedance contrast at the interface of low velocity zone has a direct impact on both the amplification factors and the frequencies where topography effect dominates; in general, higher impedance contrasts result in higher amplification factors, while the depth of low velocity zone only affects the dominant frequencies of topography effects. We also observed very high amplitudes–sometimes nearly as high as the horizontal component–in vertical component spectral ratios, at frequencies higher than the topographic frequency. We believe this high amplitude parasitic vertical accelerations requires a special attention, because the vertical components from the mode-converted and Rayleigh waves caused by slope inclinations are strongly rotational; thus they can increase the moment demand to nearby structures.

It appears that the high velocity zone at depth increases the topographic amplification factors for both horizontal and vertical component; yet it manifests more pronounced effect on the vertical component. Unlike the effect of low velocity zone near the surface, we observed no significant effect on higher frequencies; it seems the

presence of bedrock would just increase the topographic amplification factor near the topographic frequency.

Our parametric study on the effect of ground motion intensities suggests that nonlinear response of soils could aggravate the topographic amplification, most probably by the instantaneous softening of near surface soils. The result suggests that a slope with soft surficial layers would be especially susceptible to this phenomenon, especially in higher frequencies.

CHAPTER 5

Ground motion observations at Hotel Montana during the M7.0 2010 Haiti Earthquake: Topography or Soil Amplification?

5.1 Introduction

Topography effects are associated with the presence of strong topographic relief (hills, ridges, canyons, cliffs, and slopes), complicated subsurface geometries (sedimentary basins, alluvial valleys), and geological lateral discontinuities (e.g., ancient faults, debris zones). These features have been shown to significantly affect the intensity, frequency content and duration of ground shaking during earthquakes. Examples of *topographic amplification* of seismic ground motion are the PGA=1.82g recording by the hilltop Tarzana station during the 1994 Northridge Earthquake [12], the Pacoima Dam (PGA=1.12g) recording during the 1971 San Fernando earthquake, the recent extraordinary ground motion (PGA=2.74g) recorded at K-Net station MYG004 during the 2011 Tohoku Earthquake on the crest of a 5m high, steep man-made slope [36], and numerous others (see [25], [8], [3]).

Observational evidence from past earthquakes indicates that damage concentration occurs where steep slopes or complicated topography is present; buildings located

on the tops of hills, ridges, and canyons, have been shown to suffer more intense damage than those located at the base. There is also strong recorded evidence that surface topography affects the amplitude and frequency content of the ground motions. Reviews of such instrumental studies and their comparison to theoretical results can be found in [8, 23–25]. Among others, a case study on the response of a steep site in the Southern Alps revealed a crest-to-base spectral ratio of 20 [37]. In another case study, records obtained on a small ridge revealed that their spectral ratio to recorded motions at a nearby station on flat ground were only a function of topography and site conditions and were nearly independent of the azimuth, distance, and size of the seismic events [56]. By contrast, topography effects on three-dimensional features were shown to strongly dependent on source-station azimuth in studies conducted by [40] and [35], highlighting the complexity and associated numerous parameters involved in evaluating and predicting topographic amplification of seismic motion.

The problem of scattering and diffraction of seismic waves by topographical irregularities has been studied by many researchers, and examples include [7, 10, 11, 44, 51, 56] who studied topography effects using numerical techniques such as finite differences, finite-elements, boundary-elements, and discrete-wave number methods. A limited number of examples, which involve more complex simulations such as numerical models with soil layering and/or three dimensional effects, can be found in [2, 9, 13, 25, 40, 45, 60]. A comprehensive review of such analyses is given in a study by Assimaki [3]. In a comparative study of observations and predictions of topography effects, Geli et al. [25] showed that topographic amplification ratios typically range from 2 to 10, while events have also been recorded with spectral amplifications on the order of 20 or more. Later, Bard [8] summarized the findings by Geli et al. [25] as follows:

1. There exists a qualitative agreement between theory and observations on ground motion amplification at ridges and mountain tops, and de-amplification at the

base of hills.

2. The observed or computed amplification is first-order related to the "sharpness" of the topography: the steeper the average slope, the higher the peak amplification.

3. Topographic effects are frequency-dependent; the stronger effects correspond to wavelengths comparable to the horizontal dimension of the topographic feature.

Topography effects are not accounted for in design guidelines, attenuation relations and hazard maps in the US, despite the documented evidence on the role of topography in elevating seismic risk. Even further, analytical solutions and numerical methods available for site-specific problems significantly underpredict the observed amplifications, a discrepancy partially attributed by Geli et al [25] to simplified assumptions such as homogeneous halfspace, elastic material behavior and monochromatic or narrowband incident pulses instead of broadband ground motions. Two exceptions are: (i) the European Seismic Code [20], which proposes a correction factor for both cliff and ridge type topographies as a function of the slope height and inclination; and (ii) the 1995 French Seismic Code [1], which proposes a similar aggravation factor to account for 2D amplification on cliff-type topographies as a function of the cliff height and the slope inclination. Case studies, however, such as the Tarzana Hill in Los Angeles (Bouchon & Barker, 1996) demonstrate that extremely high acceleration levels (1.78g) may be associated with topographic features of small height (H = 18m) and low slope angle ($i = 10\,\mathrm{deg}$), suggesting that there exist additional factors that control topographic amplification of seismic motion and should be investigated, if not explicitly accounted for as part of design recommendations.

In this paper, we analyze a case study of topography effects from the catastrophic 2010 M7.0 Haiti Earthquake, where the severe damage observations and aftershock

recorded amplification in the vicinity of Hotel Montana, located along a foothill ridge in northern Pétionville, brought topography effects forward to explain the observations [29]. To test this hypothesis, we conduct site-specific numerical simulations for the convex ground surface geometry and soil profile at Hotel Montana comprising one-dimensional (1D) site response analyses, two-dimensional (2D) analyses of seismic response of the ridge on homogeneous elastic halfspace, and combined analyses of the layered soil profile with irregular surface geometry. We qualitatively demonstrate that the observed amplification is most likely attributed to coupling between soil layering and topographic amplification, heretofore referred to as *'soil-topography coupling effects'*. These effects differ from the superposition of one-dimensional ground response and ray focusing alone, and arise from seismic waves trapped in the near surface soil layers, amplified or de-amplified as a consequence of soil-bedrock impedance and nonlinear response, and further modified due to scattering, refraction, mode conversion and interference caused by the non-horizontal ground surface.

We finally conduct a parametric investigation of the role of surface soil stiffness, soil thickness and soil-bedrock impedance on the intensity of soil-topography coupling amplification, and show that when accounting for a soil-bedrock interface at approximately 100m depth, predictions are in excellent agreement with the observed motions. Our study highlights the complexity of the seismic wavefield in the near surface of layered soils with irregular surface geometry, and illustrates that the predicted levels of seismic ground motion amplification in the vicinity of topographic features can be significantly improved when soil layering and ground surface topography are simultaneously accounted for in numerical simulations. Similar conclusions have been drawn by previous studies such as Paolucci et al. [40] for strong motion observations obtained on an instrumented hill at Matsuzaki, Japan, and Grazier [26] who revisited the case of Tarzana Hill and explained the extremely high acceleration levels as the result of soil amplification coupled to topography effects.

5.2 Macroseismic Observations and Aftershock Recordings

The city of Port-au-Prince suffered widespread damage during the M7.0 Haiti earthquake of 12 January 2010, with an officially announced death toll of 230,000 [22], 97,294 residential structures destroyed, and 188,383 damaged beyond repair; the catastrophic consequences of the event were attributed to the proximity of epicenter and the poor construction quality of the residential structures. Site effects played a key role in the damage distribution [43], manifesting both as sediment-induced amplification and as ray focusing at convex features of the strong topographic relief. In this paper, we focus on the case study of Hotel Montana, that was located along a foothill ridge in northern Pétionville and suffered extensive damage during the mainshock along with a number of adjacent residential structures. Due to the ground surface geometry at the site, the localized damage pattern was initially attributed to topography effects [29].

Hough et al. [29] deployed eight portable K2 seismometers equipped with force-balance accelerometers and, at two stations, velocity transducers in order to explore the damage distribution within Port-au-Prince. Two of these instruments were deployed in late January, 2010 while the remaining six were deployed in early March. The location of the instruments is shown in Figure 5.1, which also highlights the stations of interest in this study: station HHMT that was installed on the foothill ridge adjacent to Hotel Montana on medium stiff site conditions (NEHRP Class C) with V_{s30}=626m/s, and station HCEA that was installed on competent (NEHRP Class B) site conditions with V_{s30}=1014m/s and was thus used as a reference station ([17]).

A number of weak motions associated with a series of M3-4 aftershocks were recorded cleanly across the array with good signal-to-noise ratios. We here present analysis of the largest aftershocks, namely six events with magnitudes between 3.6-4.4 listed in Table 5.1(see Hough et al. [29]).

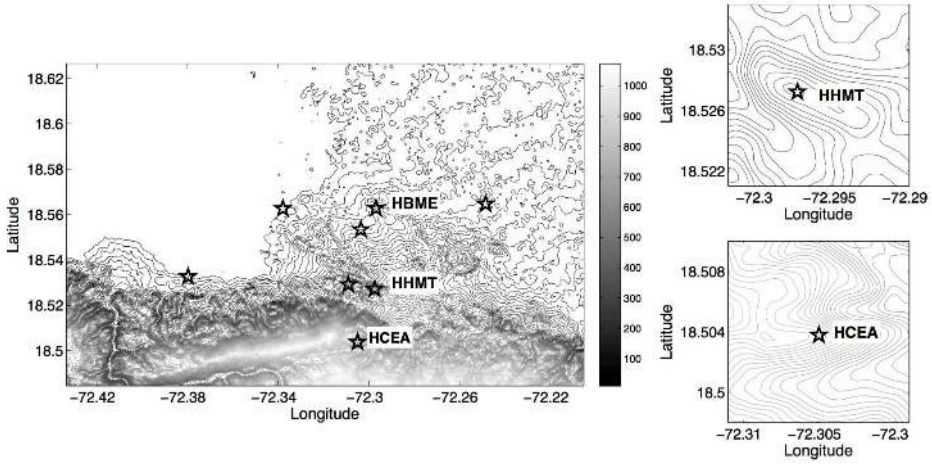

Figure 5.1: Contour map and instrumentation (stations are depicted as stars) at Pétionville district: Station HHMT is located adjacent to Hotel Montana atop a foothill ridge (see contour closeup on the top right) and station HCEA is located on competent rock and was used as reference by Hough et al. [29]

Table 5.1: Aftershock recordings by Hough et al. [29] at HHMT and HCEA, where amplification was observed in the vicinity of 7Hz.

	Month	Day	UTC	Magnitude
Event 1	03	21	02:44:28	3.7
Event 2	03	28	07:16:17	4.2
Event 3	03	28	07:16:17	4.2
Event 4	05	03	05:38:48	4.0
Event 5	05	03	19:21:24	4.4
Event 6	05	07	21:30:04	3.6

Without processing, waveforms recorded at HHMT revealed significant amplification relative to the reference station HCEA in the frequency range [6-8] Hz as shown in Figure 5.2. It should be noted here that the widely scattered broadband amplification observed in the entire [1-8] Hz frequency range indicates the spectral ratio amplitude dependency on the source-receiver azimuth (see Figure 5.3), and in turn elicits three-dimensional amplification effects from the interaction between surface and subsurface topographic features and soil irregular layering. Recent instrumental and analytical studies on the effects of source azimuth and mechanism on topographic amplification on three-dimensional features can be found in Paolucci et al. [40], Lee

et al. [33] and Maufroy et al. [35]. The lack of deeper crustal velocities, however, constrains our numerical models in the top 100m of the profile, within which we adopt the engineering amplification paradigm of vertically propagating SV waves. Paolucci et al. [40] showed that simplified 2D models of complex topographic features with non-homogeneous soil layering can yield valuable insight into the complex nature of site effects. Results presented in the ensuing should therefore be interpreted in the light of a simplified model partially explaining the recorded evidence to the extent that the latter is attributed to near-surface soil amplification and two-dimensional topography effects.

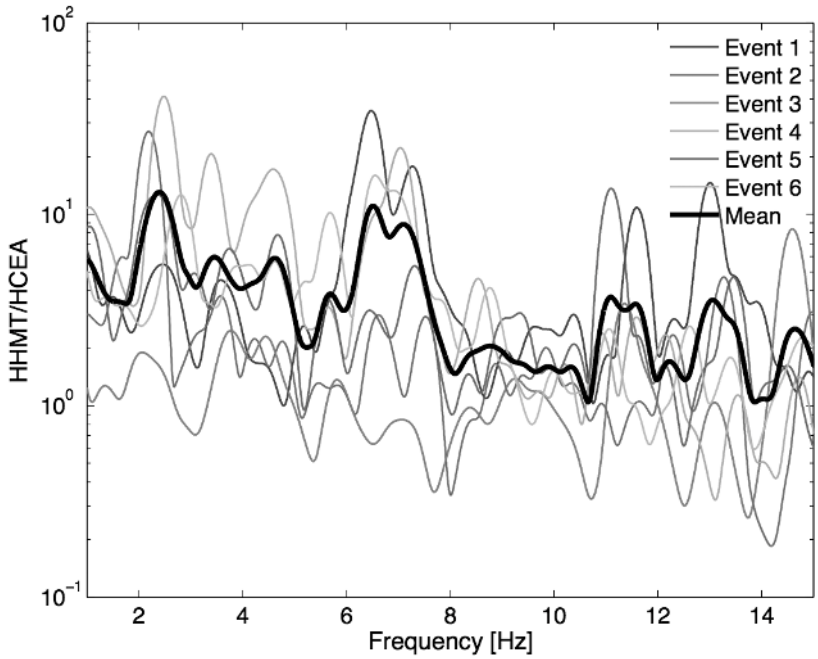

Figure 5.2: Spectral amplification of aftershock recordings at HHMT relative to HCEA in the vicinity of 7Hz, attributed to topography amplification (modified from Hough et al. [29]).

The ground surface topography at HHMT in conjunction with the localized damage pattern and the relatively uniform –albeit poor– structural quality in Pétionville, suggested ray focusing in convex features as the most likely phenomenon explaining the macroseismic observations. Note that the theoretical prediction of ground motion aggravation at HHMT using the infinite wedge model proposed by Sanchez-Sesma [47]

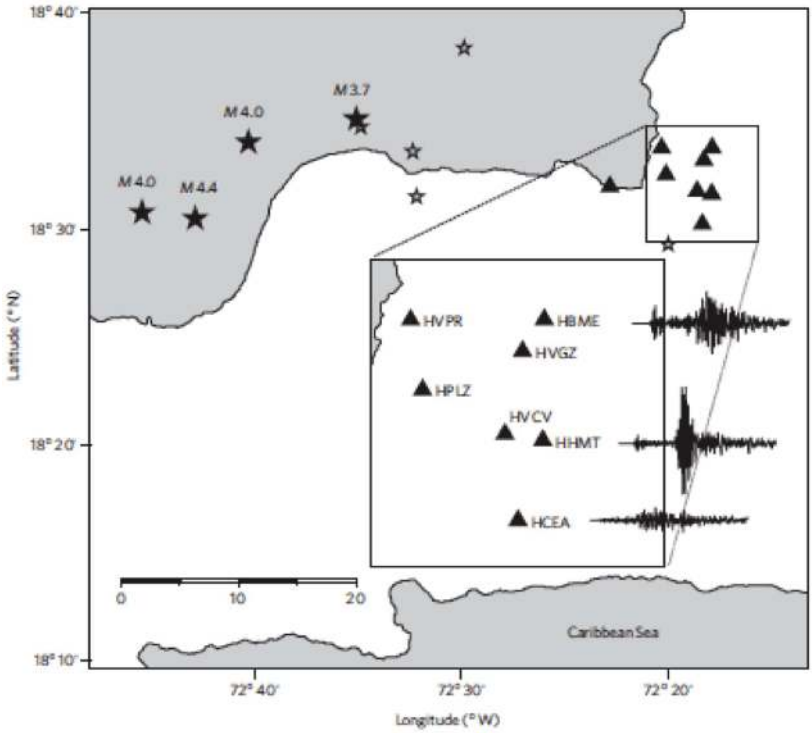

Figure 5.3: Map showing location of stations within Port-au-Prince and sample recorded waveforms. Location of several of the moderate aftershocks (black stars) and smaller events (grey stars) recorded by K2 stations (black triangles); seismograms are the northsouth component of ground motion for the 3.7 aftershock on 21 March 2010 recorded at HCEA, HBME and HHMT (peak-to-peak PGA values 0.42, 0.95 and 1:68%g, respectively) (from Hough et al. [29]).

for a simplified geometry of the foothill ridge (internal angle 135^o) and SH-wave incidence yields a topographic amplification factor of 2.7 in the frequency range [0-7] Hz. The agreement between the theoretical predictions and ground motion recordings further supported the assumption of topography effects as the dominant factor in the observed damage concentration atop the ridge.

To investigate the source of observed amplification and associated structural damage in the vicinity of Hotel Montana, we here conduct site-specific numerical simulations for the geometry and soil profile at station HHMT using Digital Elevation Maps (DEM) and Multi-Channel Analyses of Surface Waves (MASW) data collected at the sites by [17], and compare our predictions with the recorded ground motion amplification. We choose to conduct linear elastic numerical analyses based on the maximum strain induced in the near surface by the available aftershock (weak) ground motions. More specifically, we first present results of one-dimensional (1D) site response analyses at HHMT and HCEA and illustrate the negligible site amplification of the latter (reference site conditions) and the pronounced 7Hz first mode amplification of the former. Successively, we conduct two-dimensional (2D) analyses of the topographic profile at HHMT and HCEA assuming homogeneous halfspace, and show that the observed spectral amplification cannot be explained by topography amplification alone. We finally combine the two models into realistic simulations of the foothill ridge seismic response, and complement the site-specific analyses by a series of parametric studies.

5.3 One-dimensional site response analysis

Following the mainshock, Rathje et al. [43] sponsored an earthquake reconnaissance effort in the broader area of Port-au-Prince, as part of which, Cox et al. [17] evaluated MASW shear wave velocity profiles at 36 sites. The soil profiles at the sites of interest are shown in Figure 5.4, while the corresponding linear elastic frequency domain site

response, evaluated by means of the Haskell-Thompson transfer matrix method, is shown in Figure 5.5. As can be readily seen, the soil column response at station HHMT is characterized by pronounced first mode amplification at 7Hz, in the same frequency range as the observed ground motion amplification; the latter, however, was on the order of 10-20, approximately five times the predicted 1D soil amplification of amplitude 3-4. On the other hand, the stiff site conditions at HCEA yield a relatively flat transfer function up to 10Hz, and render the site an excellent candidate for site amplification reference; the computed 1D soil response of the profile at the reference station is also shown in Figure 5.5.

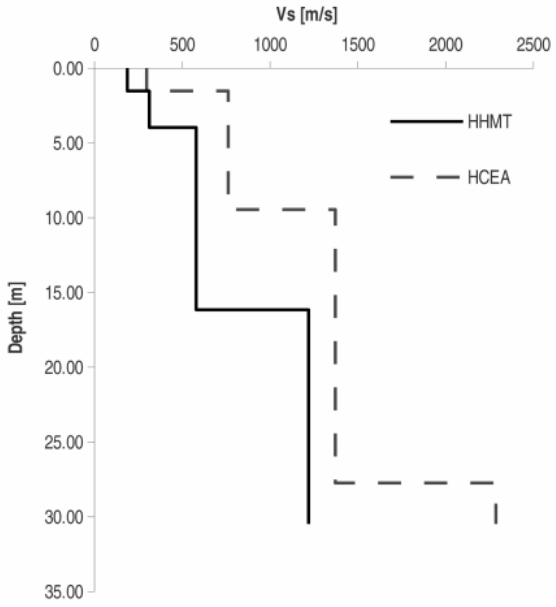

Figure 5.4: Shear wave velocity in the top 30m at stations HHMT and HCEA evaluated by means of multi-channel surface wave analysis (MASW)

5.4 Site-specific simulations of topographic amplification

We next investigate the effects of surface topography on the aggravation of seismic motion relative to flat ground conditions. The numerical models are shown in Figure 5.6 and the simulations are conducted by means of the finite element computer

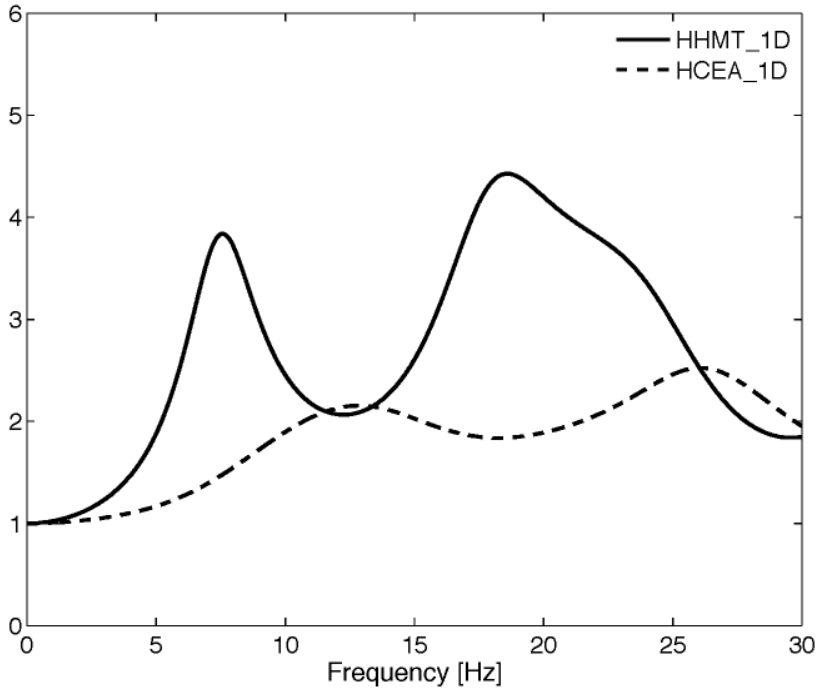

Figure 5.5: Haskell-Thompson linear elastic transfer function at the two sites, revealing the HCEA site relatively flat response in the frequency domain and the pronounced site amplification at HHMT in the vicinity of 7Hz

code DYNAFLOW (Prévost, 1995). The far field boundaries of the computational domain are located at adequate distance to approach 1D conditions and are thus constrained in the vertical direction, the ground motion is simulated as incident seismic pulse at the base of the models in the form of effective forces, and absorbing boundaries are implemented at the bottom of the model to represent the effects of reflected energy radiation towards the simulated halfspace. Details on the simulations of 2D topographic amplification by means of finite elements can be found in Assimaki et al (2005a; b). The dimensions of the topographic features at HHMT and HCEA are extracted from the Digital Elevation Map of the area shown in Figure 5.1 (A. Yong, personal communication, March 2011).

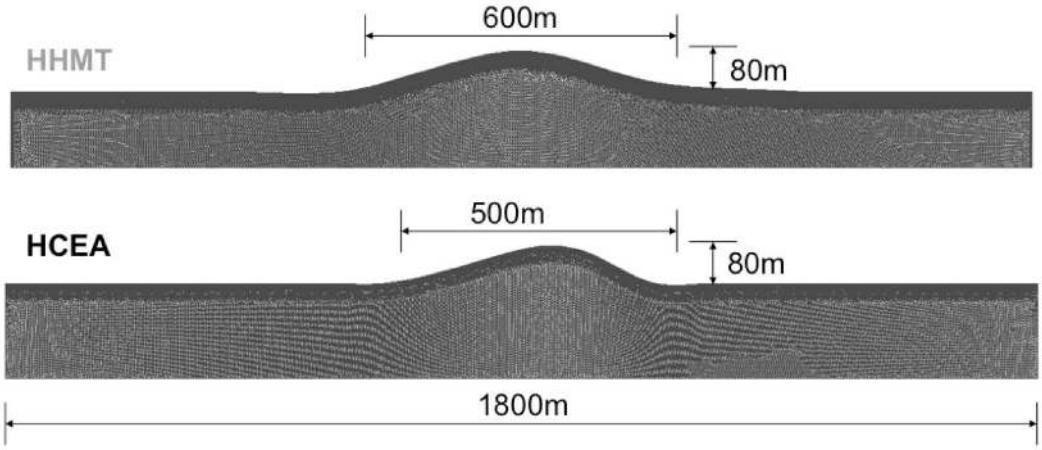

Figure 5.6: 2D Finite element models for the response analysis of topographic features, constructed on the basis of DEM data; station HCEA is installed on a ridge with dimensions comparable to HHMT

5.4.1 Homogeneous (Reference) Configuration

We first study the ground motion amplification arising from the irregular surface geometry alone by simulating the response of the features at the locations of stations HHMT and HCEA by means of linear elastic two-dimensional analyses assuming homogeneous halfspace soil conditions and vertical SV wave incidence. The shear wave velocity of the homogeneous halfspace for both features is here set at V_s=2286m/s, which corresponds to the the bedrock velocity measured by MASW at the reference station HCEA. The features are subjected to an incident train of Ricker wavelets with central frequencies 0.5, 2.5, 5 and 10 Hz. The incident waveform and corresponding Fourier Amplitude Spectra (FAS) are shown in Figure 5.7, and results are shown in Figure 5.8. The Fourier Amplitude Surface (FAS) at station HHMT subjected to a Ricker wavelet train is shown in Figure 5.7, depicting the frequency response of the feature as a function of space along the surface of the finite element model in Figure 5.6. The cross-section AA' corresponds to the FAS of the ground surface response at the vertex of the foothill ridge (i.e. approximately at the midpoint of the 600m-wide feature idealized in Figure 5.6), adjacent to Hotel Montana. Finally, the horizontal and vertical ground motion synthetics in Figure 5.8 clearly demonstrate the pulses

(and corresponding frequency range) of the Ricker wavelet train most affected by the topographic irregularity.

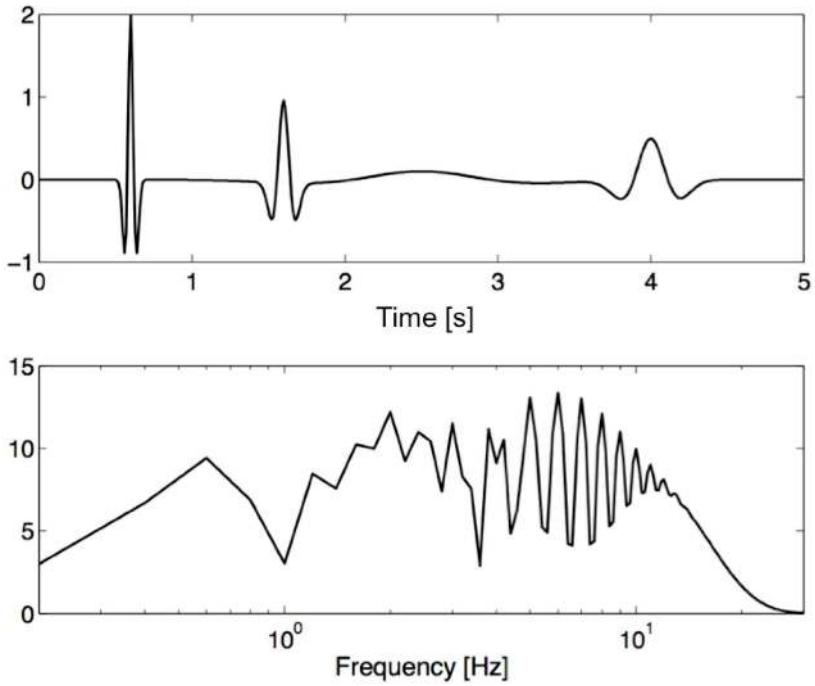

Figure 5.7: Input motions used in the simulations: A train of Ricker wavelets that shows flat distribution of energy over a wide band of frequencies for evaluating the frequency response of the ridge.

It should be noted here that the ground surface topography at stations HHMT and HCEA is very similar, which in turn implies that the frequency response of the homogeneous irregular topographic features is also expected to be similar. Indeed, the FAS's on the vertices of the homogeneous features HHMT and HCEA are compared in Figure 5.8, and one can clearly see that the frequency response of the two features is almost identical for frequencies in the vicinity of 7Hz, where amplification was identified in the recorded ground motions. It should be also noted here that the 1D ground response at the reference station HCEA shown in Figure 5.5 is relatively flat in the frequency range of interest [6-8] Hz. Given that the geometry at stations HCEA and HHMT yields practically equal topographic amplification, and the soil profile at HCEA results in almost no soil amplification, we will assume in the ensuing for

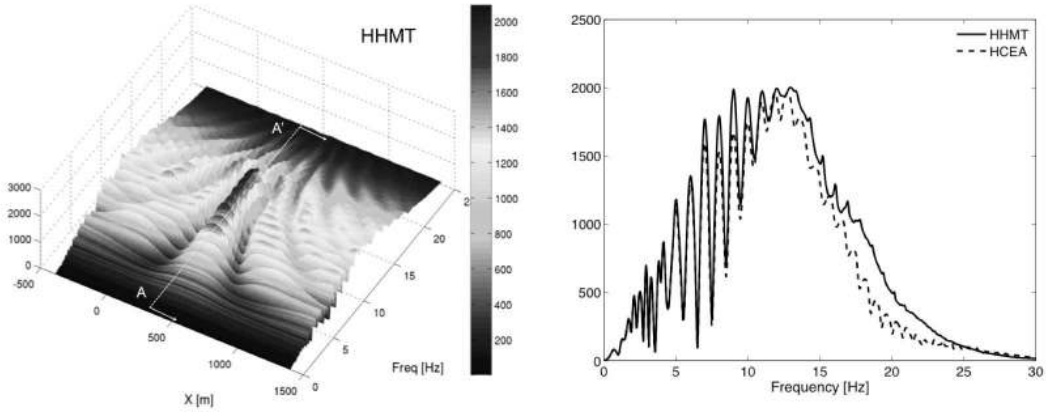

Figure 5.8: Fourier Amplitude Surface (FAS) plot on the ground surface the topographic feature of HHMT assuming homogeneous soil conditions (left), and comparison of the vertex FAS of HHMT and HCEA (right). Note that the homogeneous response of the two features is shown to be almost identical in the frequency range of ground motion recorded amplification.

simplicity that the response of the HCEA reference feature is approximately equal to the response of the homogeneous HHMT feature, and use the latter in the parametric analyses of *'soil-topography coupling effects'*.

5.4.2 Layered Configuration: Soil-Topography Coupling Effects

Successively, we integrate the effects of stratigraphy by adding continuous soil layers on the surface of the halfspace, computing the coupled response of layered feature HHMT with irregular ground surface geometry, and comparing results with the homogeneous feature used to approximate the response of HCEA (denoted heretofore *reference configuration*). Due to lack of multiple SASW measurements at the site of interest that would allow us to develop a spatially varying soil stratigraphy, we adopt the assumption of uniform thickness across the irregular topographic feature. A potentially more realistic approach would involve laterally varying soil thickness with the minimum located on the crest and the maximum in front of the toes. Preliminary analyses using this configuration, however, revealed focusing effects similar to basin edge effects emerging in the vicinity of the toes which substantially complicated the

scattered wavefield. In absence of additional geotechnical data to support a spatially varying soil profile (and the associated more complex wavefield), we chose to abort this model for the more simplified uniform thickness soil presented in the ensuing. This allows us to study the interaction between 2D topography and 1D layering, and build upon this simplified configuration future analyses that could include 3D effects and spatially varying soil formations among others.

A narrowband Ricker pulse with central frequency 7Hz is selected as vertically propagating incident wave, containing energy in the frequency range where amplification was observed in the field recordings. It should be noted here that for the reference configuration (V_s=2286m/s), a pulse with frequency 7Hz corresponds to wavelengths approximately equal to half the width of the topographic feature, and is in turn anticipated to give rise to topographic amplification [8].

Results are presented in Figure 5.9 as ground surface seismogram synthetics on the reference configuration and layered feature (vertex HHMT corresponds to the location of Hotel Montana), and as Peak Ground Acceleration (PGA) (horizontal and vertical) normalized by the corresponding value in the free-field. The term free-field is used to describe the response recorded by a station far enough from the irregular topographic feature where the ground surface motion is '*free*' from the scattered and diffracted wavefield. With the assumption of a horizontally stratified soil, the free-field response is identical to the one-dimensional site response described above. Seismogram synthetics of horizontal and vertical motion for the homogeneous and layered configurations are also compared in Figure 5.10) where the frequency dependent nature of soil and topographic amplification can be readily seen by qualitatively comparing the configuration response to three wavelets of different frequency content.

As expected, seismogram synthetics on the surface of the reference feature depict the constructive interference of direct incident and uphill traveling surface waves

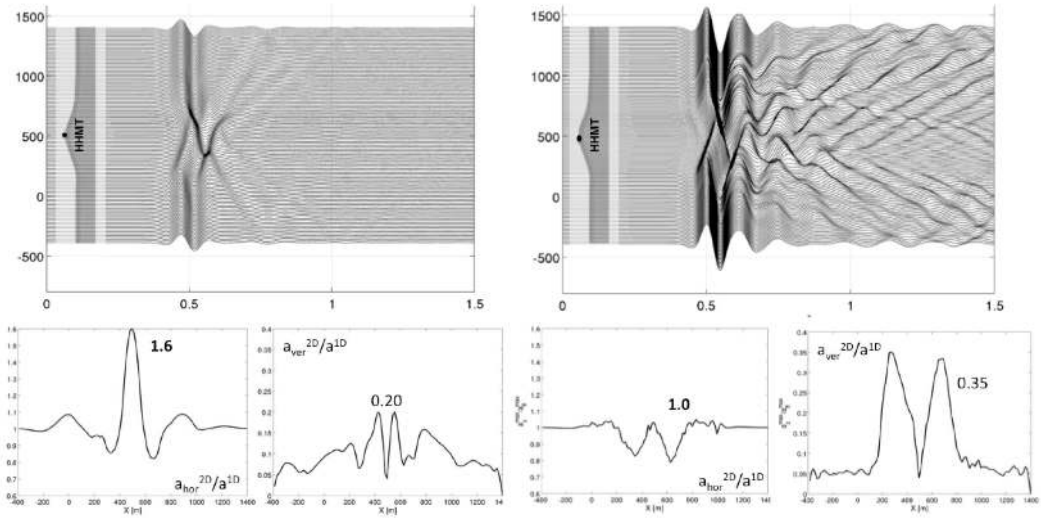

Figure 5.9: (top) Horizontal acceleration seismogram synthetics for the homogeneous ridge (left) and the ridge with measured velocity profile (right), subjected to a Ricker wavelet with $f_0 = 7Hz$ as input velocity pulse at the base of the model; (bottom) Horizontal and vertical (parasitic) peak ground acceleration (PGA) along the surface of the two configurations, normalized by corresponding horizontal PGA in the far-field (1D conditions).

at the vertex, which result in 60% amplification of the incident horizontally polarized SV wave amplitude, and vertical acceleration with amplitude 20% of the Peak Ground Acceleration in the free-field. Counterintuitively, however, the ground surface response of the layered feature (where topography effects are coupled to site amplification) shows almost no amplification at the vertex relative to the free-field. Instead, we observe approximately 20% deamplification along the slopes of the foothill ridge due to destructive interference between shear waves trapped and reverberating in the near-surface, and surface waves traveling uphill. The complexity of the wavefield compared to the homogeneous case can be clearly seen in the seismogram synthetics, where the reverberating shear waves repeatedly produce surface waves upon incidence on the surface discontinuities while gradually attenuating as a result of refraction and energy radiation towards the halfspace. By contrast, the vertical component on the ground surface is here more pronounced than in the reference configuration shown

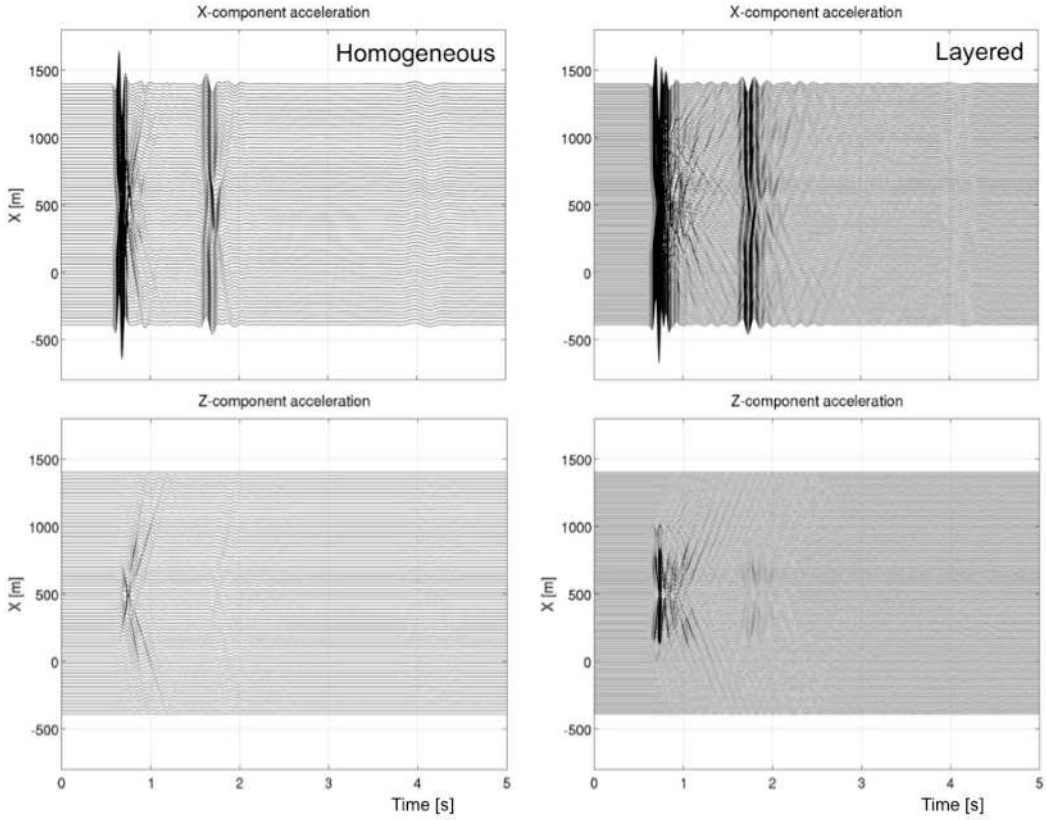

Figure 5.10: Horizontal and vertical acceleration synthetics for the homogeneous and layered configurations subjected to incoming vertically propagating train of Ricker wavelets, illustrating the frequency dependent nature of soil and topography amplification and their interaction at the hilltop

on the left, with peak amplitude 35% of the far-field PGA in the vicinity of the vertex. Note that the incident ground motion comprises purely vertically propagating SV-waves (horizontally polarized particle motion), while the ground surface response comprises both horizontal and vertical motion components; the latter corresponds to the surface wave components converted from scattered and diffracted body-waves upon incidence on the non-flat ground surface, and is for this reason heretofore termed *parasitic* vertical acceleration.

Results described above indicate that coupling between topography effects and soil amplification gives rise to complex phenomena that cannot be captured via superposition. More specifically, incident seismic waves in the near surface of irregular topographic features are trapped in the softer soil layers, and further amplified as a result of the impedance contrast, while simultaneously scattered and refracted due to the irregular surface geometry. To illustrate this concept, Figure 5.11 compares the 1D site response at HHMT shown in Figure 5.5 to the spectral acceleration ratio of the layered configuration vertex (HHMT) to the reference configuration vertex (approximating the response of station HCEA). As can be seen, the response of the stratified feature normalized by the response of the homogeneous feature is not equal to the 1D soil amplification transfer function. Instead, coupling effects give rise to a *topography-modified site response*, which differs from the free-field 1D response by a frequency dependent factor $\alpha(\omega)$ as follows:

$$\frac{U^{2D}_{layered}}{U^{2D}_{homogeneous}} \approx \frac{U^{HHMT}_{Rec}}{U^{HCEA}_{Rec}} = U^{1D}_{layered} \cdot \alpha(\omega) \tag{11}$$

The topography amplification on each feature (layered and homogeneous) is also depicted by Figure 5.11 (left) as the spectral ratio of predicted acceleration on the vertex (2D) to the acceleration in the free-field (1D). For the homogeneous case, the amplification due to topography is very mild and extends over a wide range of

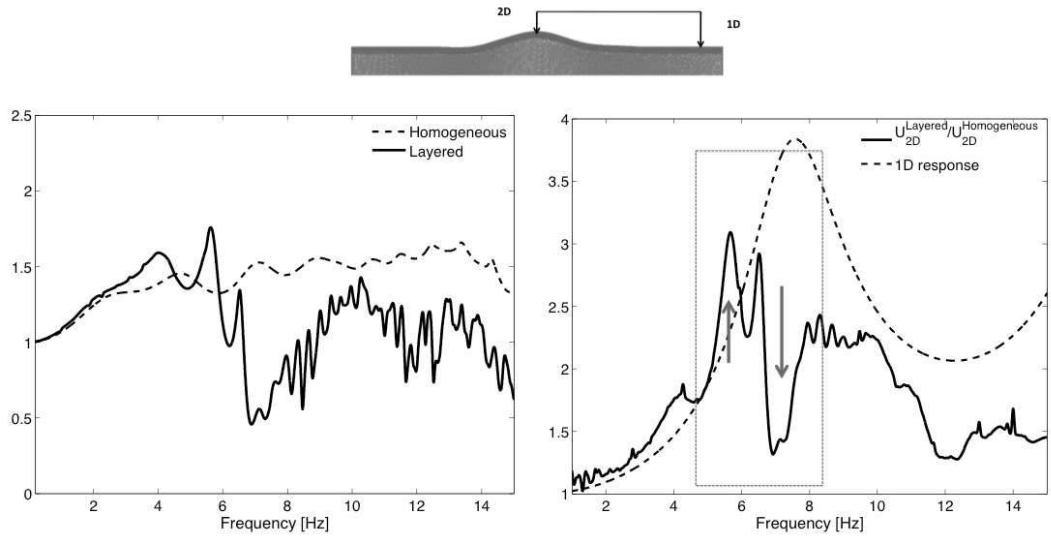

Figure 5.11: (left) Comparison of the frequency response functions of the ridge: Dashed line shows the response of homogeneous ridge and the continuous line shows the response of the ridge with measured velocity structure; (right) Frequency response of the ridge with measured velocity structure normalized by the response of homogeneous ridge (approximately equal to HCEA): Frequency response of 1D soil column at HHMT is plotted in dashed line for comparison.

frequencies, while for the layered case, amplification is observed only in the frequency-range 3-5Hz, followed by deamplification in the vicinity of 7Hz. Similarly, comparing the 1D free-field response to the topography-modified site response at HHMT (right), we observe that the coupling effects reduce the site amplification potential of the near surface stratigraphy at the profile's first mode in the vicinity of 7Hz, namely in the range where amplification was observed in the recorded ground motions at Hotel Montana.

Successively, Figure 5.12 compares the predicted topography-modified site response at HHMT to the mean frequency ratio of the recorded ground motions shown in Figure 5.2, revealing qualitative agreement in the frequency range [5-8] Hz. For comparison, Figure 5.2 also depicts the ratio of predicted layered HHMT response to the predicted HCEA response accounting for the 1D layered structure at both features (here approximated by the response of layered HHMT to homogeneous HHMT), and the 1D soil amplification transfer function at HHMT. Results illustrate that soil

response is likely to have had the strongest contribution to the amplification recorded at Hotel Montana. Results also show that while topography-induced amplification alone could explain the structural damage severity at the station, coupled topography-soil effects do capture the frequency range of amplification. Quantitatively, however, numerical simulations and field observations show a clear discrepancy, differing in magnitude by a factor of three. In the following section, we identify the parameters most likely controlling the magnitude of ground motion amplification, and speculate the orig

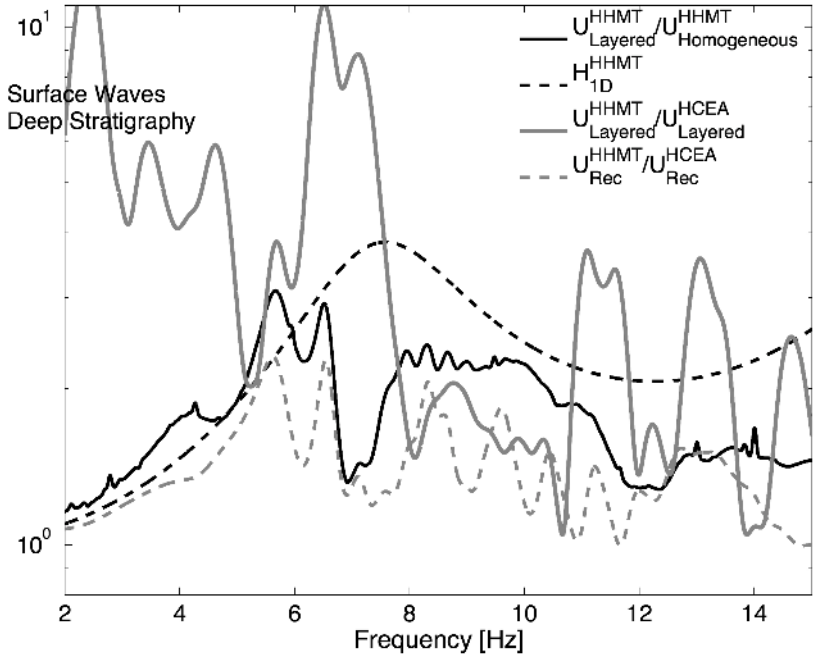

Figure 5.12: Spectral ratio of the recorded response at HHMT over HCEA, compared against the computed ratio of HHMT to HCEA, the ratio of layered HHMT to homogeneous HHMT, and the 1D response of the soil column at HHMT. Numerical simulations of the seismic response of layered topographic features capture the frequency range of recorded amplification, at a significantly -however- lower amplitude.

5.4.3 Parametric Study of Coupled Topography-Soil Amplification at HHMT

In the preceding sections, we numerically simulated the ground motion amplification published by Hough et al. [29], who normalized the ground surface recordings on a foothill ridge (station HHMT) with the recordings on a similarly shaped, 2D feature

(station HCEA) with reference site conditions in accordance to the criteria by Steidl et al. [53]. We next showed that the observed amplification is most likely attributed to the altering of soil response by the irregular ground surface geometry. We termed the complex interaction between soil and topography amplification a *soil-topography coupling effects*, and qualitatively described it as the trapping of seismic waves in the surficial soil layers, and the subsequent altering of their direction, amplitude, frequency and duration due to scattering and refraction upon incidence on the irregular ground surface geometry. While, however, our numerical results qualitatively agree with the observed amplification in terms of frequency, they clearly deviate in terms of amplitude by a factor of almost three.

We here investigate this discrepancy by conducting a series of analyses to identify the parameters affecting the magnitude, frequency content and spatial distribution of ground motion amplification in the vicinity of Hotel Montana. More specifically, we investigate the role of the thickness of the surficial layers (t), the impedance contrast between the soil layers (α), and the impedance contrast between the soil and underlying elastic bedrock halfspace (α_b). For the latter, we assume a hypothetical soil-halfspace interface at h=100m, a common geotechnical engineering assumption where the halfspace is referred to as *engineering bedrock*.

For the purpose of the parametric investigation, the geometry and stratigraphy of the HHMT ridge are simplified as shown in Figure 5.13. Figure 5.14 compares the FAS of the original and simplified homogeneous HHMT ridge, and Figure 5.15 compares the 2D-to-1D spectral ratio at the vertex of the original and simplified HHMT layered ridge, as well as the ground surface horizontal and vertical PGA of the two, normalized by the corresponding site response in the free-field. Results are found to be in excellent agreement both in the frequency and the spatial domains, which allows us to replace the original layered 2D feature with the simplified configuration in our parametric study with no significant loss of accuracy. Note that the soil profile

of the original feature corresponds to the MASW inversion shown in Figure 5.4, while the latter is idealized by a three-layer formation overlying elastic halfspace. Objective of this part of the study is to identify the parameters that contribute to the observed amplification in the 6-8Hz frequency range, and the parameters that give rise to the observed low frequency peaks in the frequency range 3-4Hz.

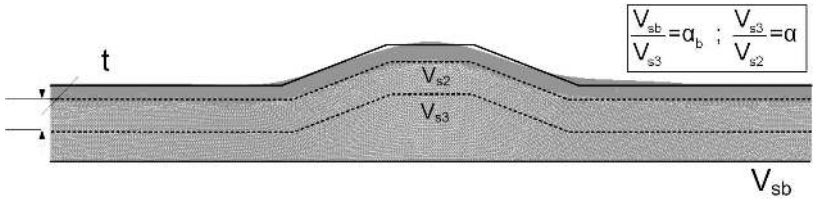

Figure 5.13: Idealized three-layer, dam shaped configuration over homogeneous elastic halfspace used in the parametric investigation of the factors that contribute to the discrepancy in amplification amplitude between observations and simulations.

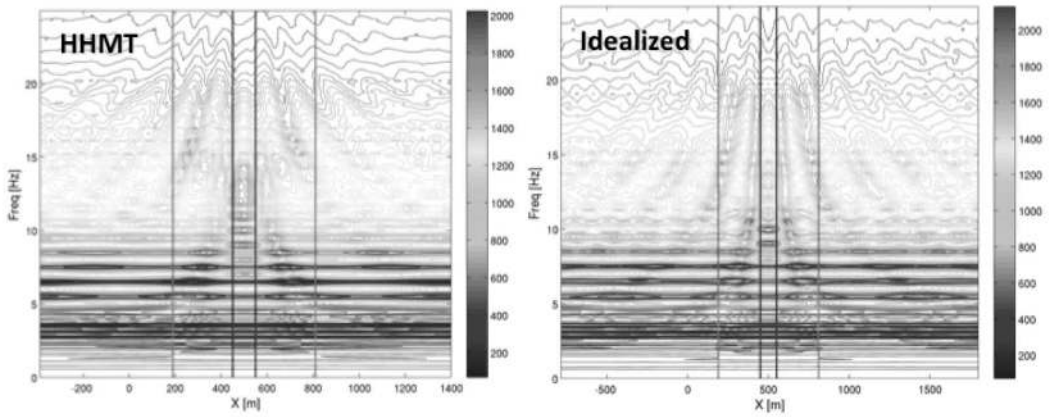

Figure 5.14: Comparison of the Fourier amplitude surface (FAS) on the surface of the original and idealized HHMT ridge subjected to a vertically propagating train of Ricker wavelets. The idealized configuration response compares very well with the original feature response, and is thereafter used instead for the parametric analysis.

To minimize the number of parameters, we note the following:

1. The weighted average shear wave velocity of the top three layers at HHMT (Figure 5.4) is 443m/s, and the quarter wavelength of a monocromatic pulse with frequency 7Hz (where amplification was observed by Hough et al. [29]) is $\lambda/4 = 15m$, approximately equal to the cumulative thickness of these layers

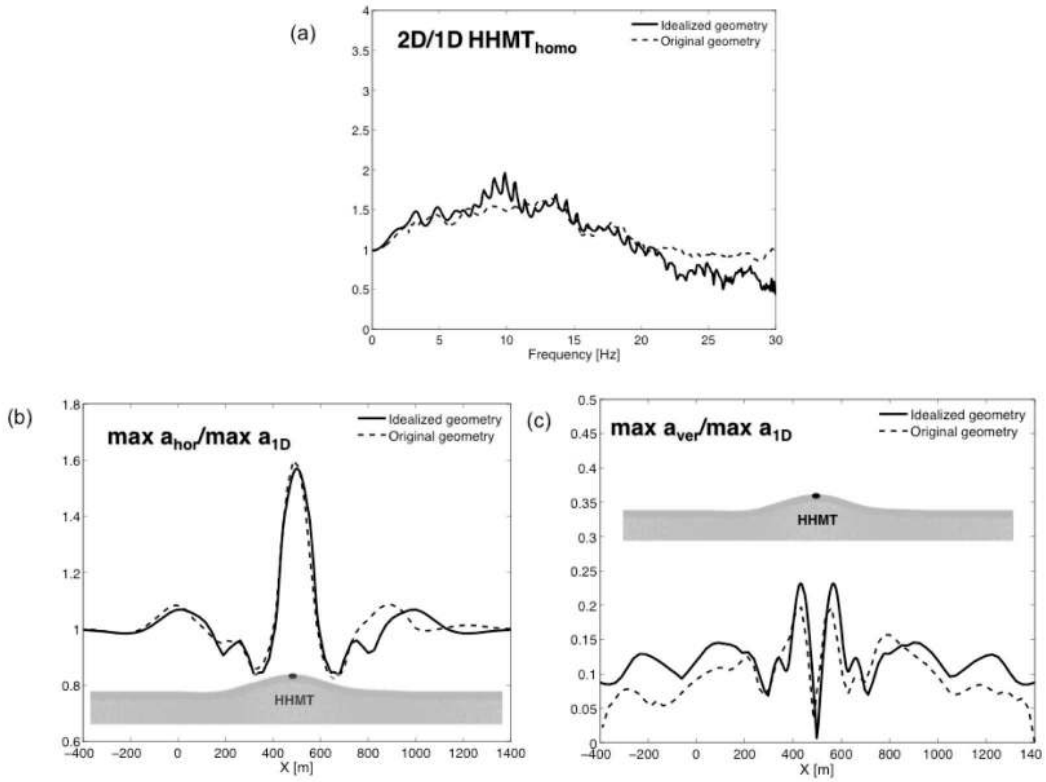

Figure 5.15: (a) Comparison of the frequency response at the midpoint of the original and idealized HHMT ridge normalized by the far-field (1D) response of the layered profile, showing the excellent agreement of the frequency response of the two features. Their response in terms of horizontal (b) and vertical (c) PGA along the surface, normalized by the horizonral far-field response (1D) is also compared and found to be of good agreement.

(17m). We therefore conclude that the resonant frequency of the site in the vicinity of 7Hz corresponds to the response of the top 3 layers whose shear wave velocity was measured via MASW by [17], and in turn fix the thickness and average velocity of the top 3 layers in our simplified configuration as $t_1 = 20m$ and $V_{s1} = 500m/s$ respectively;

2. The amplification local maximum in the range of 3-4Hz corresponds to a quarter wavelength of approximately 50m for the weighted average of all 4 layers reported by [17]. Since the maximum depth of the site investigation was 30m, we select the thickness of the second idealized layer as a parameter of the study in the range $t_2 = 10 - 50m$. We also select the impedance contrast between the second and third soil layers as a parameter that will control the amount of energy trapped above the interface, and successively amplified via reverberations in the vicinity of 3-4Hz. We denote this parameter $\alpha = (\rho_3 \cdot V_{s3}) \div (\rho_2 \cdot V_{s2})$, where $\alpha = 1.5$, 2.0 and 3.0.

We also hypothesize that the divergence of the spectral ratio amplitude at 7Hz between numerical predictions and observations is attributed to the presence of a strong impedance contrast at depth such that it does not alter the 7Hz mode of soil column response while enabling the trapping and amplification of incident seismic waves. Given that the site investigation allowed soil properties to be measured only down to a 30m depth, we set a hypothetical elastic halfspace interface at 100m depth (common assumption of the so-called *engineering bedrock*) and investigate the role of the soil-rock impedance contrast by means of the parameter $\alpha_b = (\rho_b \cdot V_{sb}) \div (\rho_3 \cdot V_{s3})$, where α_b= 1.5, 2 and 3.

Results of the parametric investigation are shown in Figure 5.16. More specifically, we first illustrate the effects of α for a configuration with $t_1 = t_2 = 20m$, $V_{s1} = 500m/s$, $V_{s2} = 1219m/s$ and $\alpha_b = 2$, and show that the presence of a strong

impedance contrast within the soil layers below the measured depth indeed increases the amplification magnitude at 7Hz compared to the original numerical model and contributes to the lower frequency amplification at the first mode of the soil column above the third layer (40m depth) and the higher frequency amplification at higher modes of the profile (¡10Hz). Next, we illustrate the effects of thickness of soil layer 2, t_2, for a configuration with $t_1 = 20m$, $V_{s1} = 500m/s$, $V_{s2} = 1219m/s$, and $\alpha = \alpha_b = 2$. This parameter affects both the amplification magnitude in the 6-8Hz frequency range and the higher response modes in the frequency range ¿10Hz. Finally, we plot the effects of α_b for a configuration with $t_1 = t_2 = 20m$, $V_{s1} = 500m/s$, $V_{s2} = 1219m/s$ and $V_{s3} = 2286m/s$ (or else $\alpha = 2$), and show that the presence of a soil-bedrock impedance contrast at 100m depth further increases the amplification magnitude at 7Hz compared to the elastic halfspace of the original numerical model.

Results of the simplified configuration with $t_1 = t_2 = 20m$, $V_{s1} = 500m/s$, $V_{s2} = 1219m/s$ and $\alpha_b = \alpha = 2$ are shown in Figure 5.17, where the observed median amplification at HHMT relative to HCEA is compared to the numerical results with the original layered configuration and the simplified configuration with added impedance contrast at depth. As can be seen, results of the parametric model are in excellent agreement with the observations both in amplitude and in frequency in the range 3-10Hz. Our parametric study suggests that the amplitude discrepancy between predictions and observations may well be attributed in part to incomplete information of the local soil conditions at HHMT (30m deep profile available), and our hypothesis of deeper soil interfaces with strong impedance contrast results in ground motion amplification that quantitatively agrees with the recorded spectral ratios at Hotel Montana.

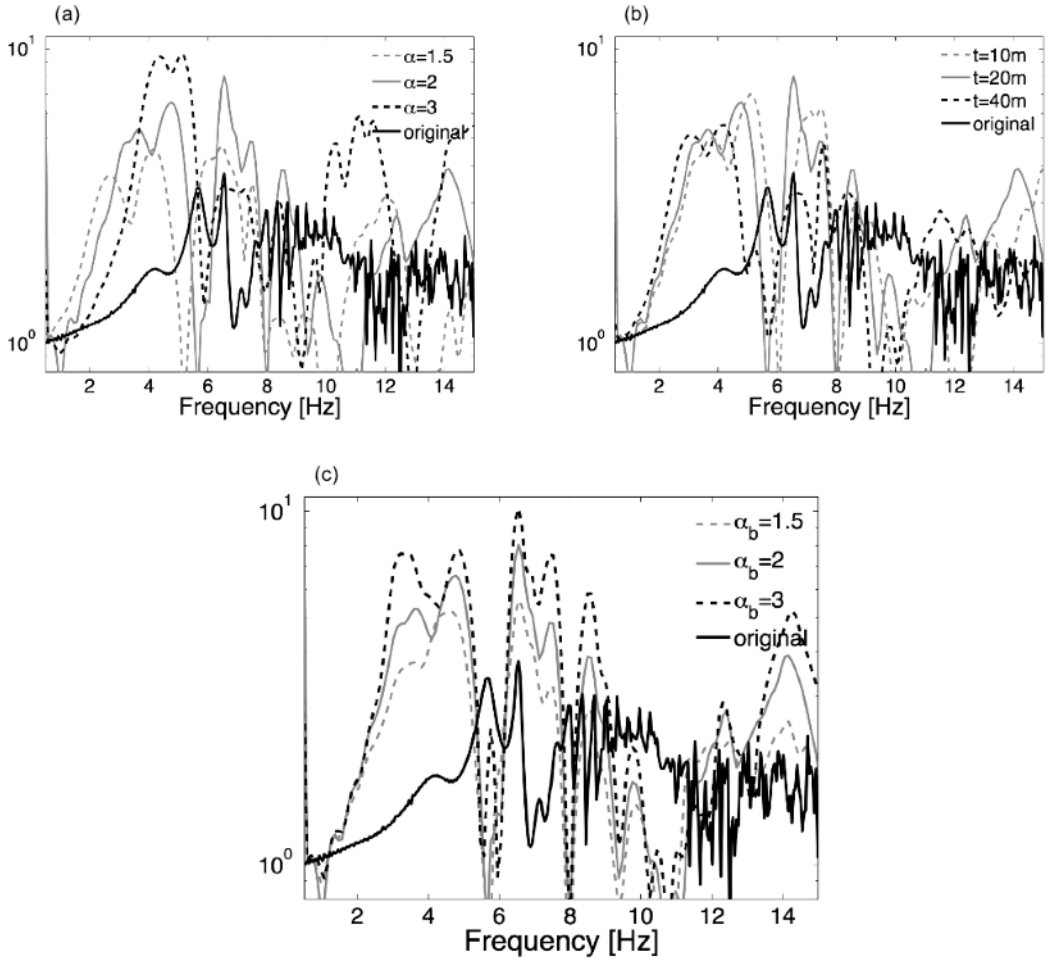

Figure 5.16: Results of the parametric simulation on the factors affecting the amplification amplitude in the vicinity of 7Hz: (a) Effects of the impedance contrast between layers 2 and 3 (α); (b) Effects of thickness of soil layer 2, t_2; and (c) Effects of the impedance contrast between soil and underlying bedrock (α_b) showing that the presence of a soil-bedrock impedance contrast at 100m depth further increases the amplification magnitude at 7Hz compared to the elastic halfspace of the original numerical model.

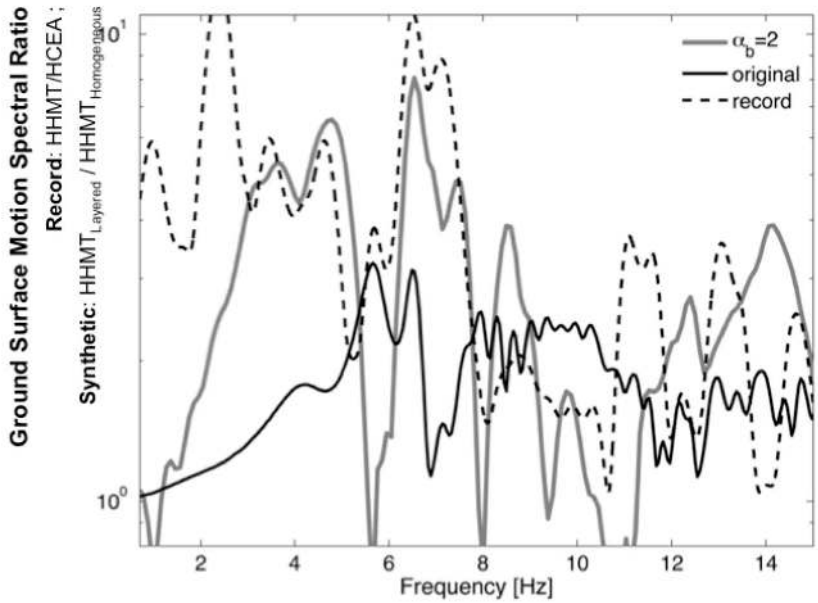

Figure 5.17: Results of the simplified configuration with $t_1 = t_2 = 20m$, $V_{s1} = 500m/s$, $V_{s2} = 1219m/s$ and $\alpha_b = \alpha = 2$ (grey line) compared to the observed median amplification at HHMT relative to HCEA (black dashed line), and the numerical results obtained using the original layered configuration (black continuous line). Predicted amplification of the simplified model with added impedance contrast at 100m depth are in excellent agreement with the observations both in amplitude and in frequency in the range 3-10Hz.

5.5 Conclusions

Following up on the work by Hough et al. [29], we conducted site-specific analyses of coupled topography-soil amplification effects at the hilltop ridge of Hotel Montana. Our simulations revealed that the observed ground motion amplification at station HHMT relative to the reference station HCEA on competent rock is potentially the result of topography-modified site response rather than topographic amplification alone. Observations and site-specific simulations were found to be in good qualitative agreement, yet quantitatively, the predicted amplification in the frequency range [6-8] Hz was found to underestimate the field recordings by a factor of three. We next investigated the parameters controlling the amplitude and frequency content of the coupled topography-soil observed amplification, and identified the thickness of sediments, the soil layer stiffness and impedance contrast as the dominant parameters. The soil to elastic halfspace impedance was shown to affect the amplitude of surface ground motion in the resonant frequency of the surface sediments, and for a contrast equal to $\alpha = 2$, the predicted ground motion amplification quantitatively compares with the observations in frequency and amplitude as shown in Figure 5.17. Also, the soil sediment thickness and soil impedance contrast below 30m was shown to contribute to the fairly systematic secondary amplification at lower frequencies, namely 3-4Hz.

We therefore conclude that the ground motion observations at Hotel Montana and the damage concentration at the hilltop was governed by soil amplification effects, manifesting in the frequency range of 1D soil response [7Hz] and modified due to scattering and refraction of the seismic waves by the irregular ground surface. Soil characterization was available only at the top 30m of the HHMT site, and most likely, the presence of a deeper soil layers of higher stiffness further aggravated the amplification of seismic waves in the near surface. Future site investigation studies using in-situ or surface wave exploration techniques with resolution below 30m would

be nonetheless needed to verify our hypothesis.

Our study shows that coupling between topography and soil amplification effects gives rise to complex wave propagation patterns in excess of the superposition of the two phenomena, and a more detailed parametric investigation of the phenomenon for generic topographic features and soil profiles is currently in progress. Among other factors, we are investigating coupled soil-topography effects during strong ground motion, where nonlinear effects are most likely to occur, and the coupling effects are anticipated to be yet more pronounced: altering of the direction of incident waves by non-flat ground conditions lead to non-uniform stiffness reduction due to nonlinear effects, which in turn further aggravates the scattering and diffraction of body waves due to the presence of reduced stiffness soil patches within the medium, in addition to the surface geometry irregularities. Overarching goal of our ongoing parametric studies, complemented by well documented case studies like the one presented here, is the compilation of our results into simplified space and frequency-dependent factors that describe seismic motion amplification in excess of soil response in the vicinity of irregular ground surface features, and can be integrated in seismic code provisions, attenuation relations, microzonation studies and seismic hazard maps to account for topographic amplification in hazard assessment, mitigation and engineering design practices.

5.6 Data and Resources

Aftershock recordings used to estimate the empirical amplification factors in this study were obtained via personal communication with S. Hough (Oct 2010) and A. Yong (Sep 2010). Recordings are currently available through the Incorporated Research Institutions for Seismology Data Management Center (IRIS DMC) `http://www.iris.edu/dms/dmc` (last accessed August 2012). Velocity profiles are described in Cox et al (2011). Simulation results and input files are available on request from

the authors.

5.7 Acknowledgments

This material is based upon work supported by the National Science Foundation under Grant No. CMMI-0936543 with title "NEESR-CR: Topographic Effects in Strong Ground Motion - From Physical and Numerical Modeling to Design" and Grant No. CMMI-1030728 with title "Topographic Amplification of Seismic Motion: Observations and Simulations in 3D". Any opinions, findings, and conclusions or recommendations expressed in this material are those of the author(s) and do not necessarily reflect the views of the National Science Foundation. The authors would also like to thank Dr. Susan Hough and Alan Yong from the USGS Pasadena Office, Dr. Brady Cox from the University of Arkansas, and Dr Jamison H. Steidl from the Institute of Crustal Studies at the UC Santa Barbara, for their help in providing the Digital Elevation, strong motion aftershock recordings and SASW soil profile data, and their insightful comments on our research findings presented here. The constructive reviews by F. Sanchez-Sesma, M. Chapman and an anonymous reviewer are hereby also acknowledged.

CHAPTER 6

Conclusions

This thesis investigated the interaction between topography and soil amplification, focusing on strong ground motions that frequently trigger nonlinear soil response. Using a finite element model validated by a series of centrifuge experiments, we first investigated whether free-field topography effects can be realistically simulated by means of centrifuge experiments. In this context, we studied how the reflected waves caused by the laminar box interfere with mode conversion and wave scattering that governs topographic amplification, and showed that the aluminum baseplate played an instrumental role in the manifestation of topographic amplification in the centrifuge. We then presented a series of parametric analyses that focused on the role of site response in modifying topographic amplification, using a properly modified reflection-free model, representative of free-field conditions. Finally we demonstrated the coupling effects of site response and topography effects through a case study from the 2010 Haiti Earthquake, on top of a small foothill ridge near Hotel Montana.

We found that the flexible centrifuge container caused spurious reflections during the experiment, due to the limitations on the container size and the shaker excitation frequencies. However, topography effect did manifest, and we observed a qualitative agreement between centrifuge experiments and our free-field numerical simulations. According to our simulations, the aluminum base plate was responsible for the high

amplification observed during the experiment; this in turn suggested the importance of deep bedrocks in topography effects.

Our results demonstrate that numerical simulations can be used to extend the parametric search space of centrifuge experimental studies, which inevitably entail modeling and budget limitations. In this case, numerical simulations enabled us to disentangle boundary effects from topographic amplification in a series of centrifuge experiments, and to demonstrate that flexible container centrifuge tests –corrected for boundary reflections– can be successfully used for studies of non-1D site response problems.

We found that the slope height, normalized by the wavelength, governs the topographic frequency; yet it has no effect on amplification factors. This finding contradicts the Eurocode 8 seismic design provisions, which suggests negligible topography effects for slopes with the height less than $30\,m$.

Our parametric study suggests that topography effects are significantly affected by –or better, coupled to– the underlying soil stratigraphy. Topographic amplification, the ground motion amplification in excess of 1D response, at the crest of the slope was severely accentuated when a strong impedance contrast was added at depth (either in the form of a bedrock of in the form of a soft surficial layer).

The result also suggests that the impedance contrast at the interface of low velocity zone controls both the amplitude and frequencies of topographic amplifications, while its depth only affects the topographic frequencies. The study showed that the presence of deep high velocity zone significantly aggravates the topographic amplifications, which confirms our observation from the experimental data.

Nonlinear soil responses further aggravated the effects of topography on seismic ground motion. We attributed the sensitivity of topography effects to nonlinear response to the associated soil softening near the surface, which intensified the impedance contrast to the deeper –less affected by site response– layers. Naturally,

the frequency components whose response was most severely altered by nonlinear response were those closest to the resonant frequencies of the soil column.

The scattering, diffraction and mode conversion of seismic waves near the topographic feature gave rise to large amplitude vertical accelerations; these accelerations have been coined 'parasitic' since they are absent from the incident motion, and they are purely the product of interaction between vertically propagating SV waves and the non-flat ground surface. In some cases, their amplitude was comparable, or even higher, than the horizontal free-field accelerations. Prompted by their amplitude and spatial variability, we believe that these components can potentially induce rotation to moment frame structures located near topographic features, and we intend to study this problem in detail in the future.

The case study of 2010 Haiti earthquake confirmed our findings and demonstrated that the coupled soil-topography amplification was responsible for observed damage concentration near Hotel Montana.

Results we presented in this thesis imply that topography effects vary significantly with soil stratigraphy. We recommend that the two phenomena, topographic amplifications and 1-D site responses, should be accounted for as a coupled process in seismic code provisions and ground motion prediction models.

References

[1] AFPS. Guidelines for seismic microzonation studies. AFPS/DRM, French Association for Earthquake Engineering, October 1995.

[2] S. A. Ashford, N. Sitar, J. Lysmer, and N. Deng. Topographic effects on the seismic response of steep slopes. *Bulletin of the seismological Society of America*, 87(3):701–709, 1997.

[3] D. Assimaki. *Topography effects in the 1999 Athens earthquake: Engineering issues in seismology*. PhD Dissertation, Department of Civil and Environmental Engineering, Massachusetts Institute of Technology, February 2004.

[4] D. Assimaki and S. Jeong. Groundmotion observations at hotel montana during the m 7.0 2010 haiti earthquake: Topography or soil amplification? *Bulletin of Seismological Society of America*, 103(5):2577–2590, 2013.

[5] D. Assimaki, G. Gazetas, and E. Kausel. Effects of local soil conditions on the topographic aggravation of seismic motion: Parametric investigation and recorded field evidence from the 1999 athens earthquake. *Bulletin of the seismological Society of America*, 95(3):1059–1089, 2005.

[6] D. Assimaki, E. Kausel, and G. Gazetas. Soil-dependent topographic effects: A

case study from the 1999 Athens earthquake. *Earthquake Spectra*, 21(4):929–966, 2005.

[7] P.-Y. Bard. Diffracted waves and displacement field over two-dimensional elevated topographies. *Geophysical Journal of the Royal Astronomical Society*, 72: 731–760, 1982.

[8] P.-Y. Bard. Local effects on strong ground motion: physical basis and estimation methods in view of microzoning studies. In *Proceedings of the Advanced Study Course on Seismotectonic and Microzonation Techniques in Earthquake Engineering*, volume 4, pages 127–218, Kefallinia, Greece, 1999.

[9] P.-Y. Bard and B. E. Tucker. Underground and ridge site effects: A comparison of observation and theory. *Bulletin of the seismological Society of America*, 75 (4):905–922, 1985.

[10] D. M. Boore. A note on the effect of simple topography on seismic SH waves. *Bulletin of the seismological Society of America*, 62(1):275–284, 1972.

[11] M. Bouchon. Effect of topography on surface motion. *Bulletin of the seismological Society of America*, 63(3):615–632, 1973.

[12] M. Bouchon and J. Barker. Seismic response of a hill: The example of tarzana, california. *Bulletin of the Seismological Society of America*, 86(1A):66–72, 1996.

[13] M. Bouchon, C. A. Schultz, and M. N. Toksöz. Effect of three-dimensional topography on seismic motion. *Journal of Geophysical Research*, 101(B3):5835–5846, 1996.

[14] A. Brambati, E. Faccioli, E. Carulli, F. Culchi, R. Onofri, S. Stefanini, and F. Ulcigrai. Studio di microzonizz azione sismica dell'area di Tarcento (Friuli). Edito

da Regione Autonoma Friuli Venezia Giulia, Universit degli Studi di Trieste, 1980. (in Italian).

[15] M. Celebi. Topographical and geological amplifications determined from strong-motion and aftershock records of the 3 March 1985 Chile earthquake. *Bulletin of Seismological Society of America*, 77(4):1147–1167, 1987.

[16] R. W. Clayton and B. Engquist. Absorbing boundary conditions for acoustic and elastic wave equations. *Bulletin of the Seismological Society of America*, 67: 1529–1540, 1977.

[17] B. R. Cox, J. Bachhuber, E. Rathje, C. M. Wood, R. Dulberg, A. Kottke, R. A. Green, and S. M. Olson. Shear wave velocity- and geology-based microzonation of Port-auPrince, Haiti. *Earthquake Spectra*, 27(S1):S67–S92, 2011.

[18] J. Dafni. *Topographic Modifications of Ground Motion and the Initiation of Coseismic Landslides*. PhD thesis, University of Washington, 2013.

[19] M. B. Darendeli. *Development of a new family of normalized modulus reduction and material damping curves*. PhD thesis, University of Texas at Austin, 2001.

[20] EC8. Design provisions for earthquake resistance of structures, part 1-1: General rules-seismic actions and general requirements for structures. prEN 1998-5, European Committee for Standardization, Brussels, 2000.

[21] A. Elgamal, Z. Yang, T. Lai, B. L. Kutter, and D. W. Wilson. Dynamic response of saturated dense sand in laminated centrifuge container. *Journal of Geotechnical and Geoenvironmental Engineering*, 131(5):598–609, 2005.

[22] M. O. Everhard, S. Baldridge, J. Marshall, W. Mooney, and G. J. Rix. The mw 7.0 haiti earthquake of january 12, 2010: USGS/EERI advance reconnaissance

team report. U.S. Geological Survey Open-File Report 2010-1048, USGS/EERI, 2010.

[23] E. Faccioli. Seismic amplification in the presence of geological and topographic irregularities. In *Proceedings of the 2nd International Conference on Recent Advances in Geotechnical Earthquake Engineering and Soil Dynamics*, volume 2, pages 1779–1797, S. Louis, Missouri, March 1991.

[24] W. Finn. Geotechnical engineering aspects of seismic microzonation. In *Proceedings of 4th International Conference on Seismic Zonation*, volume 1, pages 199–250, Stanford, CA, August 1991. EERI.

[25] L. Geli, P.-Y. Bard, and B. Jullien. The effect of topography on earthquake ground motion: A review and new results. *Bulletin of the Seismological Society of America*, 78(1):42–63, 1988.

[26] V. Grazier. Low-velocity zone and topography as a source of site amplification effect on tarzana hill, california. *Soil Dynamics and Earthquake Engineering*, 29 (2):324–332, 2009.

[27] B. O. Hardin and V. P. Drnevich. Shear modulus and damping in soils: Design equations and curves. *Soil Mechanics and Foundations Division*, 98:667–692, 1972.

[28] H. Hayashi, M. Honda, T. Yamada, and F. Tatsuoka. Modeling of nonlinear stress strain relations of sands for dynamic response analysis. In *Tenth World Conference on Earthquake Engineering*. Balkema, 1994.

[29] S. E. Hough, J. R. Altidor, D. Anglade, D. Given, M. G. Janvier, J. Z. Maharrey, M. Meremonte, B. S.-L. Mildor, C. Prepetit, and A. Yong. Localized damage cauded by topographic amplification during the 2010 m7.0 haiti earthquake. *Nature Geocience*, 3:778–782, 2011.

[30] R. L. Kondner. Hyperbolic stress-strain response: Cohesive soils. *Journal of the Soil Mechanics and Foundations Division, ASCE*, 89:115–143, 1963.

[31] B. L. Kutter, I. Idriss, T. Khonke, J. Lakeland, X. Li, W. Sluis, X. Zeng, R. C. Tauscher, Y. Goto, and I. Kubodera. Design of a large earthquake simulator at uc davis. In *Centrifuge 94*, pages 169–175. International Society of Soil Mechanics and Foundation Engineering, Balkema, August 1994.

[32] H. Law, H.-Y. Ko, and R. Scavuzzo. Simulation of O'Neill Forebay Dam, California, subjected to the 1989 Loma Prieta earthquake. In *Centrifuge 94*, 1994.

[33] S. J. Lee, D. Komatitsch, B. S. Huang, and J. Tromp. Effects of topography on seismic-wave propagation: An example from northern taiwan? *Bulletin of Seismological Society of America*, 99(1):314–325, 2009.

[34] S. Madabhushi, S. Haigh, and B. Subedi. Seismic behavior of steep slopes. In *Proceedings of the International Conference on Physical Modeling in Geotechnics*, pages 489–494, 2002.

[35] E. Maufroy, V. M. Cruz-Atienza, and S. Gaffeta. A robust method for assessing 3-d topographic site effects: A case study at the lsbb underground laboratory, france. *Earthquake Spectra*, 28(3):1097–1115, 2012.

[36] F. Nagashima, H. Kawase, S. Matsushima, F. J. Sanchez-Sesma, T. Hayakawa, T. Satoh, and M. Oshima. Application of the H/V spectral ratios for earthquake ground motions and microtremors at K-NET sites in Tohoku region, Japan to delineate soil nonlinearity during the 2011 off the Pacific Coast of Tohoku earthquake. In *Proceedings of the International Symposium on Engineering Lessons Learned from the 2011 Great East Japan Earthquake*, Tokyo, Japan, March 2012.

[37] S. Nechtschein, P.-Y. Bard, J.-C. Gariel, J.-P. Mneroud, P. Dervin, M. Cushing, B. Gaubert, S. Vidal, and A.-M. Duval. A topographic effect study in the nice

region. In *Proceedings of the Fifth International Conference on Seismic Zonation*, volume 2, pages 1067–1074, Nice, France, October 1995. Ouest Édition.

[38] F. Ozkahriman, A. Nasim, and J. Wartman. Topographic effects in a centrifuge model experiment. In 4^{th} *International Conference on Earthquake Geotechnical Engineering*, Greece, June 2007.

[39] R. Paolucci. Amplification of earthquake ground motion by steep topographic irregularities. *Earthquake Engineering and Structural Dynamics*, 31:1831–1853, 2002.

[40] R. Paolucci, E. Faccioli, and F. Maggio. 3D Response analysis of an instrumented hill at Matsuzaki, Japan, by a spectral method. *Journal of Seismology*, 3:191–209, 1999.

[41] J. Prevost. A simple plasticity theory for frictional cohesionless soils. *Soil Dynamics and Earthquake Engineering*, 4(1):9–17, 1985.

[42] J. Prevost. Dynaflow: A nonlinear transient finite element analysis program. Technical Report, Dept. of Civil Eng. and Op. Research, Princeton University, 1995.

[43] E. Rathje, J. Bachhuber, B. Cox, J. French, R. Green, S. Olsen, G. Rix, D. Wells, and O. Suncar. Geotechnical engineering reconnaissance of the 2010 haiti earthquake, 2010. GEER Association Report GEER-021, Geoengineering Extreme Events Reconnaissance, 2010.

[44] F. Sanchez-Sesma, I. Herrera, and J. Aviles. A boundary method for elastic wave diffraction: Application to scattering of SH waves by surface irregularities. *Bulletin of the seismological Society of America*, 72(2):473–490, 1982.

[45] F. J. Sanchez-Sesma. Diffraction of elastic waves by three-dimensional surface irregularities. *Bulletin of the seismological Society of America*, 73(6):1621–1636, 1983.

[46] F. J. Sanchez-Sesma. Diffraction of elastic SH waves by wedges. *Bulletin of the Seismological Society of America*, 75(5):1435–1446, 1985.

[47] F. J. Sanchez-Sesma. Elementary solutions for response of a wedge-shaped medium to incident SH and SV waves. *Bulletin of the seismological Society of America*, 80(3):737–742, 1990.

[48] W. Z. Savage. An exact solution for effects of topography on free Rayleigh waves. *Bulletin of the Seismological Society of America*, 94(5):1706–1727, 2004.

[49] A. Schofield and X. Zeng. Design and performance of an equivalent-shear-beam (ESB) container for earthquake centrifuge modelling. Department of Engineering Report CUED/D-SOILS/TR245, University of Cambridge, 1992.

[50] H. B. Seed, R. T. Wong, I. M. Idriss, and K. Tokimatsu. Moduli and damping factors for dynamic analyses of cohesionless soils. EERC Report UCB/EERC-84/14, University of California, 1984.

[51] W. D. Smith. The application of finite element analysis to body wave propagation problems. *Geophysical Journal of the Royal Astronomical Society*, 42(2):747–768, 1975.

[52] J. Snowdon. *Vibration and Shock in Damped Mechanical Systems*. Wiley, 1968.

[53] J. H. Steidl, A. G. Tumarkin, and R. J. Archuleta. What is a reference site? *Bulletin of Seismological Society of America*, 86(6):1733–1748, 1996.

[54] D. Stevens, B.-I. KIM, D. Wilson, and B. Kutter. Comprehensive investigation of nonlinear site response - centrifuge data report for DKS02. Center for

Geotechnical Modeling UCD/CGMDR-99/02, University of California at Davis, 1999.

[55] F. O. Strasser and J. J. Bommer. Large-amplitude ground-motion recordings and their interpretations. *Soil Dynamics and Earthquake Engineering*, 29:1305–1329, 2009.

[56] B. Tucker, J. King, D. Hatzfeld, and I. Nersesov. Observations of hard rock site effects. *Bulletin of the seismological Society of America*, 74(1):121–136, 1984.

[57] M. Vucetic and R. Dobry. Effect of soil plasticity on cyclic response. *Journal of Geotechnical Engineering*, 117(1):89–107, 1991.

[58] R. V. Whitman and P. C. Lambe. Effect of boundary conditions upon centrifuge experiments using ground motion simulation. *Geotechnical Testing Journal*, 9 (2):61–71, 1986.

[59] E. Yee, J. P. Stewart, and K. Tokimatsu. Elastic and large-strain nonlinear seismic site response from analysis of vertical array recordings. *Journal of Geotechnical and Geoenvironmental Engineering*, 139:1789–1801, 2013.

[60] Z. Zhenpeng, L. Baipo, and Y. Yifan. Effect of three-dimensional topography on earthquake ground motion. In *Proceedings of the 7^{th} World Conference on Earthquake Engineering*, volume 2, pages 161–168, 1980.